博士論文

Spin-charge interconversion via Rashba spin-orbit coupling at metal/oxide interfaces

(金属/酸化物界面におけるラシュバスピン分裂によるスピン－電荷相互変換)

蔡 瀚陸

Hanshen Tsai

博士論文

Spin-charge interconversion via Rashba spin-orbit coupling at metal/oxide interfaces

(金属/酸化物界面におけるラシュバスピン分裂によるスピン－電荷相互変換)

蔡　瀚陞
Hanshen Tsai

Department of Advanced Materials
UNIVERSITY OF TOKYO

MARCH, 2019

Thesis Summary

Spin-charge interconversion via Rashba spin-orbit coupling at metal/oxide interfaces

(金属/酸化物界面におけるラシュバスピン分裂によるスピン－電荷相互変換)

Spintronics, which is a study based on two fundamental properties of carriers: spins and charges, has attracted great attention in the last two decades. Spintronics has several advantages over conventional electronics; for example, flowing of the spins without moving charges causes less energy loss so spintronics devices have less heat dissipation. For making spintronics devices, the generation, manipulation, and detection of spins are the fundamental functions required. One of the most common ways to reach these requirements is using the interconversion between charge and spin. So far, two mechanisms for the spin-charge interconversion originating from the spin-orbit interaction have been demonstrated: spin Hall effect (SHE) and Rashba-Edelstein effect (REE). Spin Hall effect appears in any conductive materials with spin-orbit coupling (SOC). An applied charge current converts to a transverse spin current in SOC materials; this charge-to-spin current conversion is called direct spin Hall effect (DSHE). The inverse effect, a process that converts a spin current into a transverse charge current, is called inverse spin Hall effect (ISHE). In contrast, REE originates from the Rashba SOC induced by the broken potential symmetry. At certain interface state in x-y plane without inversion potential symmetry, the Hamiltonian of Rashba SOC can be described as $\boldsymbol{H}_{\mathrm{R}} = \alpha_{\mathrm{R}}(\boldsymbol{p} \times \hat{\boldsymbol{z}}) \cdot \boldsymbol{\sigma}$, where $\boldsymbol{\sigma}$ is the vector of Pauli spin matrices, $\boldsymbol{p}$ is the momentum, and α_{R} is so-called Rashba parameter. Because the $\alpha_{\mathrm{R}}(\boldsymbol{p} \times \hat{\boldsymbol{z}})$ term acts as a fictitious Rashba magnetic field, the conduction electron spins are aligned along $\boldsymbol{p} \times \hat{\boldsymbol{z}}$ direction. This phenomenon is known as spin-momentum locking. When an electric field is applied, the Fermi contour with spin-momentum locking shifts and generates non-equilibrium spin accumulation, whose gradient drives a diffusive spin current into an adjacent conductive layer. This charge-to-spin (C-S) conversion is called the direct Edelstein effect (DEE). In reverse, injecting the spin current into the interface generates charge current and this phenomenon is called the inverse Edelstein effect (IEE). Recently, it has been shown that the conversion efficiency through IEE can be even larger than SHE in typical SHE materials such as β-W and Pt [E. Lesne, *et al. Nat. Mat.* **15**, 1261-1266 (2016)]. Therefore, the spin-charge interconversion via Rashba SOC is expected to have greater potential in spintronics application. So far, the S-C conversion at three types of Rashba interfaces have been studied: metallic interface, metal/oxide interface and oxide/oxide interfaces. The origin of Rashba effect at metallic

and oxide/oxide interfaces have been well studied in last few years. However, there are only few experiment reports of metal/oxide Rashba interfaces. Metal/oxide interfaces have two advantages: the lower resistance of metal layer than SHE materials promises a lower energy consumption than using SHE effect, and it is also possible to apply gate voltage at oxide insulator layer to control Rashba effect. For the possible spintronics application, a further understanding of metal/oxide type Rashba interfaces is necessary.

In this thesis, we focus on the spin-charge interconversion via Rashba spin-orbit coupling at metal/oxide interface. The spin-to-charge conversion is measured by spin pumping method and the charge-to-spin conversion is detected by spin-torque ferromagnetic resonance method. Firstly, to clarify guiding principles for designing metal/oxide interfaces, we investigated the materials dependence of conversion efficiency at various metal/oxide interfaces. In addition, because the metal/oxide interface is contacted with metal layer directly, it is expected that the conversion efficiency at the interface state may be influenced by the adjacent metal bulk state. To understand the relation between metal/oxide interface and metal bulk, we increased the electron momentum relaxation time of metal bulk by decreasing temperature and investigated the temperature dependence of S-C conversion at metal/oxide interface.

The major results of the thesis are as follows:

Strong modulation of Rashba spin-splitting due to material dependent electron distribution at metal/Bi_2O_3 interfaces. (Chapter 4)

To understand how to design the metal materials of non-magnetic metal (NM)/oxide interface with large Rashba spin-splitting, NM material dependence of spin-to-charge (S-C) conversion efficiency at NM/Bi_2O_3 interfaces is investigated by spin pumping method. Cu, Ag, Au, and Al are used as NM materials. We observed large modulation and sign change in spin-to-charge (S-C) conversion efficiency λ_{IEE} which corresponds to the variation of Rashba spin-splitting. The experimental results together with first-principles calculations indicate that such large variation is caused by material dependent electron distribution near the interface. We found that the work function difference between metal and oxide materials is an important essence for determining electron distribution and Rashba parameter α_{R}. A smaller work function difference corresponds to a stronger localization of electron distribution near NM nuclei which results in a larger α_{R} and λ_{IEE}. In addition, the sign of work function change the direction of interfacial electric field and therefore change the sign of α_{R}. We also found that the SOC of NM layer has almost no contribution to Rashba effect at metal/oxide interface because the SOC of Bi is much larger and becomes dominant. This study suggests a way to design the metal/oxide interface for large Rashba spin-splitting and efficient spin-to-charge interconversion. [**H. Tsai**, S. Karube, K. Kondou, N. Yamaguchi, F. Ishii and Y. Otani, "Clear variation of spin splitting by changing electron distribution at non-magnetic metal/Bi_2O_3 interfaces", Scientific Reports, vol. 8, no. 1, 2018.]

Efficient spin-charge interconversion at Cu(Ag)/oxide interfaces without heavy elements. (Chapter 5)

In chapter 4, Bi_2O_3 is used as the oxide layer due to the large spin-orbit coupling of Bi. To improve the materials selections for oxide materials at metal/oxide interface, the oxide materials dependence of S-C conversion is investigated. SnO_2, HfO_2, Al_2O_3, SiO_2, ITO (Indium Tin oxide) are used as oxide layer. From spin pumping measurement, only Cu/ITO interface shows notable S-C conversion signal which is 5 times larger than others; this results cannot be explained by only the strength of SOC. We further investigate both S-C conversion and charge-to-spin conversion at Cu(Ag)/ITO interfaces. Both the conversion efficiency and α_{R} of Cu(Ag)/ITO are comparable to Cu/Bi_2O_3 despite of the 5-6 times smaller SOC of In and Sn than Bi. In addition, estimated spin current conductivity at Cu(Ag)/ITO interface is even larger than typical spin Hall materials Pt and β–Ta due to the high conductivity of Cu(Ag) layer. These results indicate that heavy element is not necessary for efficient spin-charge interconversion at metal/oxide interfaces. Such large α_{R} should originate from some special features of the electron distribution at Cu(Ag)/ITO interfaces though the exact shape of electrons distribution is out of our understanding. One hypothesis is that the conductive feature of ITO may enable more electrons locate near In or Sn nuclei than Bi in insulating Bi_2O_3. Further studies are required to understand whether the conductive oxide layer can really enhance the Rashba effect at metal/oxide interfaces. [K. Kondou, **H. Tsai**, H. Isshiki, and Y. Otani "Efficient spin current generation and suppression of magnetic damping due to fast spin ejection from nonmagnetic metal/Indium-tin-oxide interface", APL Materials 6, 101105, 2018.]

Enhancement of S-C conversion due to the increasing momentum relaxation time of metal layer at low temperature (Chapter6)

Spin-to-charge conversion coefficient λ_{IEE} can be described by $\lambda_{\mathrm{IEE}} = \alpha_{\mathrm{R}}\tau_{IEE}/\hbar$, where τ_{IEE} is the spin relaxation time at interface. Therefore, increasing τ_{IEE} is a way to enhance λ_{IEE} without changing α_{R}. Because τ_{IEE} is strongly influenced by the momentum relaxation time of adjacent metal layer, it is possible to modulated λ_{IEE} by changing τ_p^{NM}. In this study, we increases conductivity of metal layer, which is proportional to τ_p^{NM}, by decreasing temperature from 290 K to 10 K at Cu(Ag)/Bi_2O_3 interfaces. 40(17) percentages enhancement of λ_{IEE} at 10 K due to the increased τ_p^{NM} at Cu(Ag)/ Bi_2O_3 interface are observed. From the experiment results, we found that the spin relaxation time τ_{IEE} at metal/oxide interface is proportional to τ_p^{NM} of metal layer. This relation can be explained by the spin-momentum locking at interface and the additional momentum relaxation process induced by the hybridization between 2D interface state and 3D metallic state. This study indicates that λ_{IEE} at metal/oxide interface can be enhanced by increasing conductivity, i.e. making high conductivity metal layer, and also provides a further understanding of the mechanism of the spin-to-charge conversion at metal/oxide interfaces. [**H. Tsai**, K. Kondou, and Y. Otani, "Enhancement of spin-to-charge current conversion at metal/oxide interface by increasing momentum relaxation time", in preparation.]

Contents

CHAPTER 1

CHAPTER 2

CHAPTER 3

CHAPTER 6

Enhancement of spin-to-charge conversion at metal/oxide interface by increasing momentum relaxation time 78

CHAPTER 7

Conclusion 89

Chapter 1

Introduction

In this chapter, we start with a general review of spintronics and the background of this thesis, and then describe the motivation and purpose.

1.1 Spintronics

Spintronics, which is a study based on two fundamental properties of carriers: spins and charges, has attracted great attention in last two decades. Spintronics emerged from the discoveries of giant magnetoresistance (GMR) in multilayers composed of alternating ferromagnetic and non-magnetic conductive layer by Albert Fert [1-1] and Peter Grünberg [1-2] in 1988. GMR effect shows tens of percentages variation of magnetoresistance, i.e. 20% at room temperature and 85% at 4.2 K observed by Albert Fert [1-1]. This value is much larger than the magneto-resistance of metal materials which is about few percentages. GMR technology dramatically increase the sensitivity and decrease the size of magnetic field sensors, which is widely used in hard disk in computers. Since then, studies in spintronics field have shown rich application in improving the conventional electronics devices.

Nowadays, the rapid development of electronics, especially in computing and information storage, have changed the life of human beings. However, when purchasing a higher density of integrate circuit and better performance of electronic devices, the increasing energy consumption becomes a serious problem. In conventional electronics devices, a continuously flowing current is required to maintain and transport the information of charge; therefore, massive power consumption is generated by Joule heating and even more energy is required for cooling the devices. In addition, more charge leakage is occurred when the sizes of the devices are scaled down. In contrast, for spintronics devices, flowing of only spin angular momentum without moving charges, which is so-called spin current or pure spin current, has less heating effect and causes less energy loss.

Thus, spintronics devices are considered as a powerful candidate of next generation devices. The generation, manipulation, and detection of the spin current are the most fundamental functions for developing spintronics devices. A general way to reach these requirements is using the interconversion between charge and spin, which is the main topic of this thesis. So far, two of the most common mechanisms for the spin-charge interconversion originating from the spin-orbit interaction have been demonstrated: spin Hall effect (SHE) and Rashba-Edelstein effect (REE).

Spin Hall Effect

Spin Hall effect (SHE) is a spin-charge interconversion phenomenon appearing in any conductive materials with spin-orbit coupling (SOC). An applied charge current converts to a transverse spin current and generate a spin accumulation at the edge of bulk materials as shown in Fig. 1-1(a); this charge-to-spin current (C-S) conversion is called direct spin Hall effect (DSHE). The inverse effect, a process that converts a spin current into a transverse charge current as shown in Fig. 1-1(b), is called inverse spin Hall effect (ISHE). It is first predicted by Mikhail I. Dyakonov and Vladimir I. Perel in 1971 [1-3] and revised by Hirsch [1-4]. However, there was no any experiment evidence during a long time until 2004; Kato *et al.* succeed to experimentally observe the spin accumulation due to SHE at GaAs/InGaAs [1-5]. In this experiment, a charge current is injected into GaAs/InGaAs heterostructures and generates a spin accumulation at the edge; this spin accumulation is observed by using a spatially resolved magneto-optical Kerr effect setup (MOKE) as shown in Fig. 1-1(c). After the first optical observation of SHE, the electrical detections and the characteristics of SHE of various materials becomes a hot topic. The key parameter of SHE is the conversion efficiency between spin and charge current, which can be defined as spin Hall angle (SHA). So far, several techniques have been developed to determine SHA of materials, such as spin pumping [1-6], spin-torque ferromagnetic resonance (ST-FMR) [1-7], non-lateral spin injection [1-8], and spin Hall magnetoresistance (SMR) [1-9]. Many materials have been investigated by these techniques, and it has been found that heavy metals, such as Pt and β-W [1-10], have larger SHA about few percentages to over 10%. Using SHE materials is considered as a promising way to generate and detect spin current, and it already shows great potential in the application of spintronics devices, such as magnetization switching [1-11] and domain wall motion [1-12]. Though SHE has been intensively studied in last two decades, a search of large SHE materials and the suitable SHE materials for commercial application is still one of the most important topics in spintronics field.

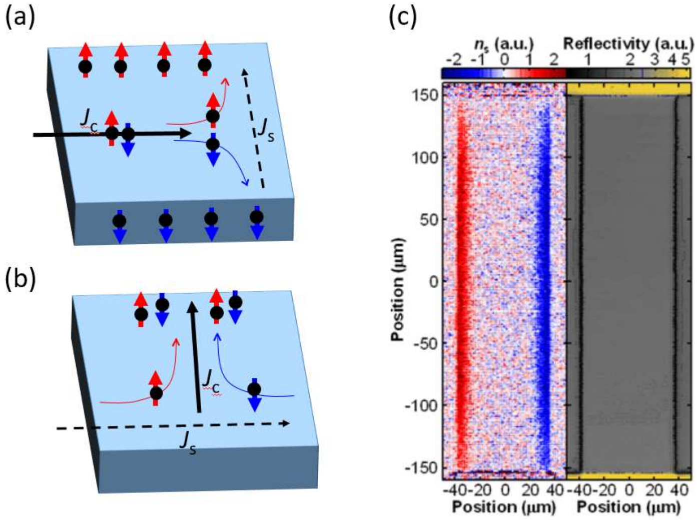

Figure 1-1. (a) A schematic of direct spin Hall effect (DSHE). (b) A schematic of inverse spin Hall effect (ISHE). (c) Spin accumulation observed by MOKE at GaAs/InGaAs sample. The red and blue point show the opposite spin directions [1-5].

Rashba-Edelstein effect

Rashba-Edelstein effect (REE) is a spin-charge interconversion phenomenon originates from the momentum-dependent splitting of spin bands at 2-dimension electron gas with Rashba effect. Rashba effect is theoretically demonstrated by Rashba in 1959 [1-13]. At certain surface or interface of materials, i.e. surface of Au(111), an surface/interfacial electric field is naturally generated by the Fermi energy difference and thus the inversion potential symmetry is broken by the electric field. This kind of surface/interface is called Rashba surface/interface. The Rashba Hamiltonian can be described as $\boldsymbol{H}_\mathrm{R} = \alpha_\mathrm{R}(\boldsymbol{p} \times \hat{\boldsymbol{z}}) \cdot \boldsymbol{\sigma}$, where $\boldsymbol{\sigma}$ is the vector of Pauli spin matrices, $\boldsymbol{p}$ is the momentum, and α_R is so-called Rashba parameter. Because of this spin-dependent Hamiltonian, the energy bands of spin up and down splits at Rashba system. Additionally, because the $\alpha_\mathrm{R}(\boldsymbol{p} \times \hat{\boldsymbol{z}})$ term acts as a fictitious Rashba field, the conduction electron spins are aligned along $\boldsymbol{p} \times \hat{\boldsymbol{z}}$ direction as shown in Fig. 1-2(a). This phenomenon is known as spin-momentum locking. The first observation of Rashba state on metal surface succeeded in 1996 on the Au(111) surface by using angle-resolved photoemission spectroscopy (ARPES) [1-14]. A spin-splitting of free-electron-like energy band is observed as shown in Fig. 1-2(b). In 1990, Edelstein demonstrated that a spin accumulation can be occurred by inducing electric current in 2DEG with Rashba SOC [1-15]. When an electric field E_x is applied, the Fermi contour with spin-momentum locking shifts in x-direction and generates non-equilibrium spin accumulation, whose gradient drives a diffusive spin current into an adjacent conductive layer. This charge-to-spin (C-S) conversion is called the direct Edelstein effect (DEE). In reverse, injecting the spin current into the interface generates charge current; this phenomenon is called the inverse Edelstein effect (IEE). Note that the conversion efficiency of IEE and DEE is both proportional to Rashba parameter.

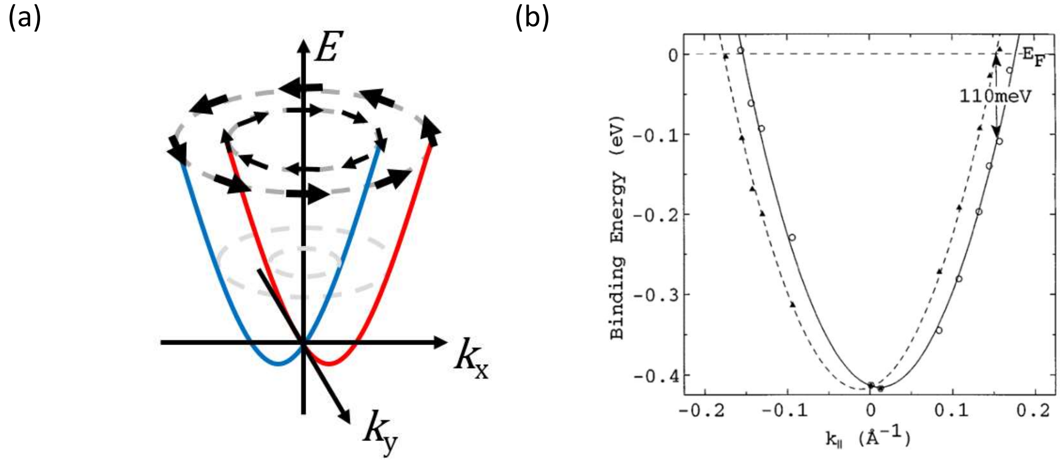

Figure 1-2. (a) Typical spin-momentum locking in Rashba system (b) Rashba spin-splitting at surface of Au(111) observed by angle-resolved photoemission spectroscopy (ARPES) [1-14]

In 2010, a spin-transfer torque generated by DEE is observed at Pt/Co/AlO$_x$ tri-layers structure in the study of magnetization switching [1-16]. A few years later, the first experiment evidence of spin-charge conversion via IEE is observed at Ag/Bi Rashba interface by spin pumping method [1-17]. The S-C conversion efficiency via IEE is defined as $\lambda_{\mathrm{IEE}} \equiv j_{c(2D)}/J_s$, where $j_{c(2D)}$ is the charge current density at 2D interface and J_s is the 3D spin current density. Estimated λ_{IEE} at Ag/Bi interface is 0.3 nm. In this paper, by using the model of strong spin-momentum locking Rashba system, λ_{IEE} is described by $\lambda_{\mathrm{IEE}} = \alpha_{\mathrm{R}}\tau_{IEE}/\hbar$, where τ_{IEE} is the spin relaxation time. In contrast, by using a more general Rashba model which includes the case of weak spin-orbit coupling, Shen, K. theoretically demonstrated a similar relation that $\lambda_{\mathrm{IEE}} = \alpha_{\mathrm{R}}\tau_p/\hbar$, while τ_p is the electron momentum relaxation time at interface. Authors of Ref. [1-17] comment that because τ_p equals to τ_{IEE} in the strong-orbit coupling system, this two relations are actually consistent. Since then, Rashba-Edelstein effect is intensively studied as an alternative effect of spin Hall effect. Recently, it has been shown that the conversion efficiency through IEE can be one order larger than typical SHE materials such as β-W and Pt [1-18]. This result shows the great potential of Rashba interface in spin-charge interconversion. In addition, while the conversion efficiency of SHE is confined by the atomic SOC of bulk materials, the REE at Rashba interface does not only depend on SOC but also the broken inversion symmetry induced by the combination of materials at interface. This feature of REE enables plentiful material selection for spin-charge interconversion. Thus, Rashba interface is expected to have great potential in spin generation and detections and the studies of how to design materials of Rashba interfaces becomes an important issue in spintronics field.

1.2 Background

So far, Rashba effect and Rashba-Edelstein effect have been studied in mainly 3 types of interfaces: metallic interface [1-17], metal/oxide(insulator) interface [1-19], and oxide(insulator)/oxide(insulator) interface [1-18, 20]. In last few years, metallic interface and oxide/oxide interface have been well studied by various methods. In 2007, a largest value of Rashba parameter until now, $\alpha_{\mathrm{R}}\sim 3$ eV·Å, was observed at Ag(111)/Bi metallic interface by ARPES [1-21]. By using other materials instead of Ag or Bi layer, such as Cu/Bi [1-22,23] and Ag/Pb [1-24] interface, several metallic interfaces have been investigated by ARPES and first-principle calculation. From these studies, it has been known that such large Rashba spin-splitting at metallic interfaces comes from the surface alloying structures at the interface and the atomic SOC of heavy element Bi or Pb [1-21~24]. In 2013, J. C. Rojas Sánchez *et al.* succeed to observed the IEE at Ag/Bi by spin pumping method [1-17]. In this experiment, NiFe/Ag/Bi tri-layer samples are prepared for spin pumping method as shown in Fig. 1-3(a). By exciting NiFe layer in ferromagnetic resonance, a spin current is pumped from NiFe layer to the Ag layer and converts to charge current at Ag/Bi interfaces via IEE which can be electrically detected. Fig. 1-3(b) shows the FMR resonance spectrum and the detected current spectrum at NiFe/Ag, NiFe/Bi, and NiFe/Ag/Bi samples. All of them shows clear FMR resonance while only NiFe/Ag/Bi shows much larger charge current signal than others, which indicates that the S-C conversion due to IEE at Ag/Bi Rashba interfaces is most dominant. The S-C conversion efficiency, $\lambda_{\mathrm{IEE}} \equiv j_{c(2D)}/J_s$, is estimated to be 0.3 nm at Ag/Bi interface. For comparison with spin Hall effect, the spin Hall angle of materials can be converted to λ_{IEE} through $\lambda_{\mathrm{IEE}} = \theta_{\mathrm{SHE}} l_{\mathrm{sf}}$, where θ_{SHE} is the spin Hall angle and l_{sf} is the spin diffusion length [1-18]. As the results, λ_{IEE} is 0.2 nm for Pt, 0.3 nm for Ta and 0.43 nm for β-W [1-10]. Thus, the S-C conversion efficiency at Ag/Bi is comparable to typical SHE materials, which should be large enough for possible application.

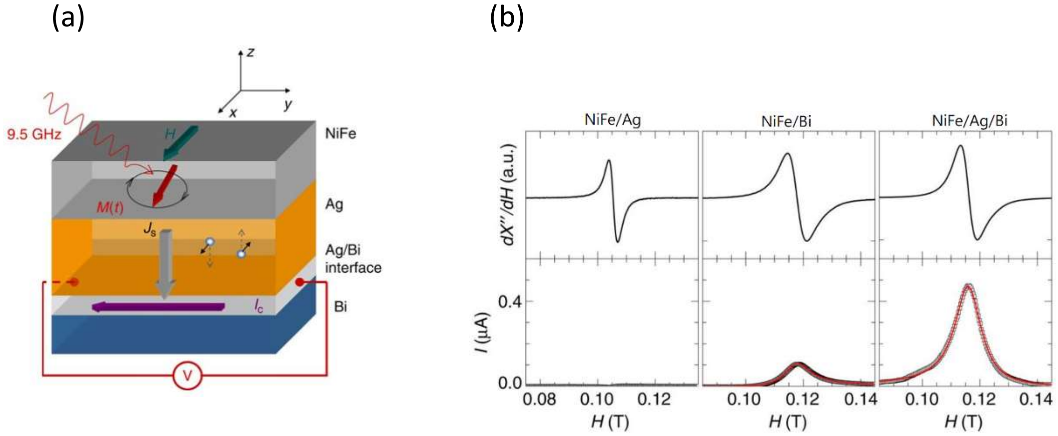

Figure 1-3. (a) Schematic of spin pumping measurement in NiFe/Ag/Bi tri-layer [1-17] (b) detected charge current spectrum in [1-17]. No detected signal at NiFe/Ag sample

In case of oxide/oxide interface, the 2DEG at oxide/oxide interfaces is first observed at the $LaAlO_3$(LAO)/$SrTiO_3$(STO) interfaces in 2004 [1-25]. Few years later, A. D. Caviglia *et. al.* reported that Rashba SOC at LAO/STO interfaces can be tuned by applying gate voltage, and the maximum value of α_{R} estimated by weak localization measurements is ~0.05 eV·Å [1-26]. Following this studies, by applying gate voltage on the STO layer in spin pumping measurement, a tunable and high efficient S-C conversion at LAO/STO is observed in 2016 [1-18]. The sample structure is the same as the experiment of Ag/Bi before but this time with a gate voltage applied at the bottom of STO layer as shown in Fig. 1-4(a). Fig. 1-4(b) shows the current spectrum modulated by different gate voltages. A maximum value of conversion efficiency λ_{IEE} becomes to 6.4 nm, which is one order larger than Ag/Bi interfaces even though α_{R} at LAO/STO is 2 orders smaller than Ag/Bi interfaces. Such large λ_{IEE} can be explained by the relation $\lambda_{\mathrm{IEE}} = \alpha_{\mathrm{R}}\tau_p/\hbar$. Because τ_p is much longer at LAO/STO interfaces (~ps) than Ag/Bi interfaces (~fs), an efficient λ_{IEE} can be obtained even with quite small α_{R}.

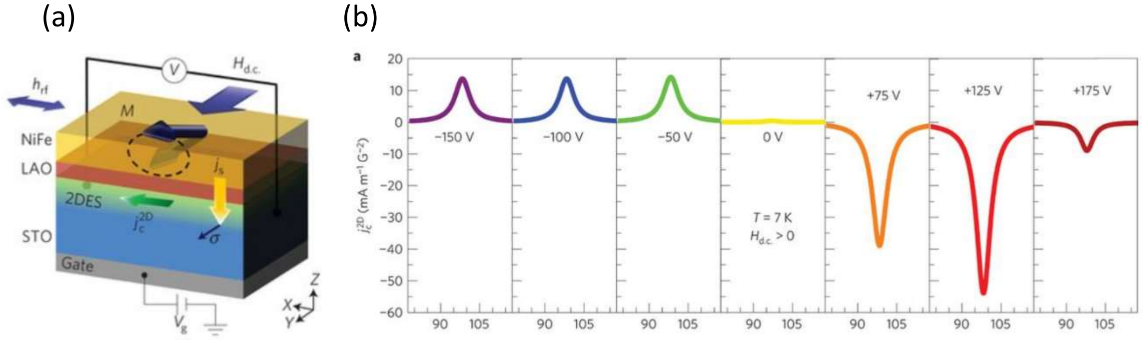

Figure 1-4. (a) Schematic of spin pumping measurement at LAO/STO interfaces with gate voltage [1-18] (b) Current spectrum detected with various gate voltages at LAO/STO interfaces [1-18].

Compared to metallic interface and oxide/oxide interfaces, there are only a few experiment reports of metal/oxide Rashba interface so far. The first experiment evidence of metal/oxide Rashba interfaces is the observation of efficient S-C conversion at Cu/Bi_2O_3 interfaces by spin pumping method in 2016 [1-19]. Estimated λ_{IEE} of Cu/Bi_2O_3 is 0.2-0.6 nm, which is comparable to Ag/Bi interfaces while the estimated α_{R} is one order smaller than Ag/Bi. Subsequently, a spin accumulation generated by charge current via DEE at Cu/Bi_2O_3 and Ag/Bi_2O_3 interfaces is observed by MOKE [1-27]. Later, Rashba-Edelstein magnetoresistance (EdMR), which is related to both IEE and DEE, is observed in CoFe/Cu/Bi_2O_3 systems [1-28]. From these studies, there are sufficient evidences of the Rashba-Edelstein effect at metal/oxide interfaces, where the S-C conversion efficiency

λ_{IEE} is comparable to metallic interfaces and typical SHE materials. In addition, because it is possible to apply the gate voltage on an insulating oxide layer, which is similar with oxide/oxide interface case, a tunable α_{R} may be expected at metal/oxide interface. Therefore, metal/oxide interface is considered as a good candidate for efficient spin-charge interconversion. However, in previous studies, only two kinds of metal/oxide interfaces, Ag/Bi_2O_3 and Cu/Bi_2O_3, have been investigated so far. Thus, the role of metal or oxide layer in the interfacial Rashba effect is still unknown and the guide principle for designing suitable metal/oxide Rashba interface is not clear yet. A systematically investigation, i.e. materials dependence, is necessary to understand how to enhance the conversion efficiency at metal/oxide interfaces for possible application in the spintronics field. For these purpose, in this thesis, we focus on the spin-charge interconversion via Rashba spin-orbit coupling at metal/oxide interface.

1.3 Motivation and purpose

As introduced in section 1.2, metal/oxide interface is considered as a good candidate for efficient spin-charge interconversion. Here we summarized the characteristics of metallic interfaces, oxide/oxide interface, and metal/oxide interface in Table. 1-1. The purpose of this thesis is to clarify the origins of the Rashba effect at metal/oxide interfaces and to enhance λ_{IEE} at metal/oxide interfaces. For this purpose, firstly, to understand the contribution of metal layer, we investigate the metal materials dependence of α_{R} and λ_{IEE} at metal (Cu, Ag, Au, Al)/ Bi_2O_3 interfaces by spin pumping method. Also a first-principle calculation, which is a collaboration work with Prof. Ishii's group in Kanazawa University, is performed to calculated the band structure and α_{R} at Cu, Ag, Au/ Bi_2O_3 interfaces. Secondly, we investigated the oxide materials dependence of α_{R} and λ_{IEE} at Cu/oxide interfaces by using SnO_2, HfO_2, Al_2O_3, SiO_2, ITO (Indium Tin Oxide) as the oxide materials. In addition, previous studies suggest that λ_{IEE} is related to an electron momentum relaxation time τ_p at interface and the momentum relaxation time τ_p^{NM} of metal layer. Therefore, we try to increaseτ_p and τ_p^{NM} by decreasing temperature and observe whether λ_{IEE} can be enhanced.

Type of interfaces	Origins	Example	α_{R} (eV·Å)	τ_{IEE}	λ_{IEE} (nm)
Metal/metal	Atomic SOC, Surface alloying	Ag/Bi	3	~fs	0.2-0.4
Oxide/oxide	2DEG in quantum well	LAO/STO	0.01-0.05	~ps	0-6.4
Metal/oxide	? (This work)	Cu/Bi_2O_3 (This work: metal/Bi_2O_3, Cu/Oxide)	0.3-0.4	~fs	0.2-0.6

Table. 1. Comparison of the origins, α_{R}, τ_{IEE}, and λ_{IEE} at 3 types of Rashba interfaces.

1.4 Outline

This thesis consists of 7 chapters.

Chapter 1 gives a general review of spintronics and spin conversion phenomenon, and introduces the background of this thesis, and then describes the motivation and purpose.

Chapter 2 summarizes the theory on Rashba effect, Rashba-Edelstein effect, spin pumping, and spin-transfer torque ferromagnetic resonance (ST-FMR).

Chapter 3 describes the sample fabrication, experiment method of spin pumping and ST-FMR, and the first-principle calculation method.

Chapter 4 describes the experiment and the calculation results of metal materials dependence of the S-C conversion efficiency and Rashba parameter at metal/Bi_2O_3 interfaces. A large modulation and sign change in conversion coefficient which corresponds to the variation of spin splitting are observed. The origin of this strong metal materials dependence is the electron distribution at interfaces which will be discussed in chapter 4.

Chapter 5 describes the oxide materials dependence of the S-C conversion efficiency and Rashba parameter at Cu/oxide interfaces. A surprisingly efficient S-C conversion is observed at Cu/ITO interfaces whose conversion coefficient is comparable to Cu/Bi_2O_3 interface even though the atomic SOC at Cu/ITO is about 5 times smaller than Cu/Bi_2O_3. An efficient C-S conversion at Cu, Ag/ ITO interfaces is also observed by ST-FMR method. These results indicate that heavy element is not necessary for efficient spin-charge interconversion. The origins of this efficient conversion is not clear yet and we will discuss the possible origin in chapter 5.

Chapter 6 describes the temperature dependence of S-C conversion efficiency at Cu, Ag/ Bi_2O_3 interfaces. The S-C conversion efficiency at Cu (Ag)/Bi_2O_3 interfaces enhances 40 (17)% at 10 K compared with RT by increasing the conductivity in Cu(Ag). By calculated the momentum relaxation time of metal, τ_p^{NM}, at each temperature, we found the relation $\lambda_{\mathrm{IEE}} \propto \tau_p^{NM}$. The origin and meaning of this relation will be discuss in chapter 6.

Chapter 7 summarizes the conclusions and the future prospects of this thesis.

Reference of chapter 1

[1-1] M. Baibich, J. Broto, A. Fert, F. Van Dau, F. Petroff, P. Etienne, G. Creuzet, A. Friederich and J. Chazelas, *Physical Review Letters* **61**, no. 21, pp. 2472-2475 (1988).

[1-2] G. Binasch, P. Grünberg, F. Saurenbach and W. Zinn, *Physical Review B* **39**, no. 7, pp. 4828-4830 (1989).

[1-3] M. I. Dyakonov and V. I. Perel, *Journal of Experimental and Theoretical Physics Letters* **13**, p. 467 (1971).

[1-4] J. Hirsch, *Physical Review Letters* **83**, no. 9, pp. 1834–1837 (1999).

[1-5] Y. Kato, *Science* **306**, no. 5703, pp. 1910-1913 (2004).

[1-6] E. Saitoh, M. Ueda, H. Miyajima and G. Tatara, *Applied Physics Letters* **88**, no. 18, p. 182509 (2006).

[1-7] L. Liu, T. Moriyama, D. Ralph and R. Buhrman, *Physical Review Letters* **106**, no. 3 (2011).

[1-8] T. Kimura, Y. Otani, T. Sato, S. Takahashi and S. Maekawa, *Physical Review Letters* **98**, no. 15 (2007).

[1-9] H. Nakayama, M. Althammer, Y. Chen, K. Uchida, Y. Kajiwara, D. Kikuchi, T. Ohtani, S. Geprägs, M. Opel, S. Takahashi, R. Gross, G. Bauer, S. Goennenwein and E. Saitoh, *Physical Review Letters* **110**, no. 20 (2013).

[1-10] W. Witczak-Krempa, G. Chen, Y. Kim and L. Balents, *Annual Review of Condensed Matter Physics* **5**, no. 1, pp. 57-82 (2014).

[1-11] L. Liu, O. Lee, T. Gudmundsen, D. Ralph and R. Buhrman, *Physical Review Letters* **109**, no. 9, 2012.

[1-12] P. P. J. Haazen, E. Murè, J. H. Franken, R. Lavrijsen, H. J. M. Swagten & B. Koopmans, *Nature Materials* **12**, pp. 299–303 (2013).

[1-13] Y. A. Bychkov and E. I. Rasbha, *Journal of Experimental and Theoretical Physics Letters* **39**, p.78 (1984).

[1-14] S. LaShell, B. McDougall and E. Jensen, *Physical Review Letters* **77**, no. 16, pp. 3419-3422 (1996).

[1-15] V. Edelstein, *Solid State Communications* **73**, no. 3, pp. 233-235, (1990)

[1-16] I. Mihai Miron, G. Gaudin, S. Auffret, B. Rodmacq, A. Schuhl, S. Pizzini, J. Vogel and P. Gambardella, *Nature Materials* **9**, no. 3, pp. 230-234 (2010).

[1-17] J. Sánchez, L. Vila, G. Desfonds, S. Gambarelli, J. Attané, J. De Teresa, C. Magén and A. Fert, *Nature Communications* **4**, no. 1 (2013).

[1-18] E. Lesne, Y. Fu, S. Oyarzun, J. Rojas-Sánchez, D. Vaz, H. Naganuma, G. Sicoli, J. Attané, M. Jamet, E. Jacquet, J. George, A. Barthélémy, H. Jaffrès, A. Fert, M. Bibes and L. Vila, *Nature Materials* **15**, no. 12, pp. 1261-1266 (2016).

[1-19] S. Karube, K. Kondou and Y. Otani, *Applied Physics Express* **9**, no. 3, p. 033001 (2016).

[1-20] A. D. Caviglia, M. Gabay, S. Gariglio, N. Reyren, C. Cancellieri, and J. M. Triscone, *Physical Review Letters* **104**, no. 12, pp. 126803 (2010).

[1-21] C. Ast, J. Henk, A. Ernst, L. Moreschini, M. Falub, D. Pacilé, P. Bruno, K. Kern and M. Grioni, *Physical Review Letters* **98**, no. 18 (2007).

[1-22] H. Bentmann, T. Kuzumaki, G. Bihlmayer, S. Blügel, E. Chulkov, F. Reinert and K. Sakamoto, *Physical Review B* **84**, no. 11 (2011).

[1-23] H. Bentmann, F. Forster, G. Bihlmayer, E. Chulkov, L. Moreschini, M. Grioni and F. Reinert, *Europhysics Letter* **87**, no. 3, p. 37003, (2009)

[1-24] G. Bihlmayer, S. Blügel and E. Chulkov, *Physical Review B* **75**, no. 19 (2007).

[1-25] A. Ohtomo & H. Y. Hwang, *Nature* **427**, pp. 423–426 (2004)

[1-26] A. Caviglia, M. Gabay, S. Gariglio, N. Reyren, C. Cancellieri and J. Triscone, *Physical Review Letters* **104**, no. 12 (2010).

[1-27] J. Puebla, F. Auvray, M. Xu, B. Rana, A. Albouy, H. Tsai, K. Kondou, G. Tatara and Y. Otani, *Applied Physics Letters* **111**, no. 9, p. 092402, (2017).

[1-28] J. Kim, Y. Chen, S. Karube, S. Takahashi, K. Kondou, G. Tatara and Y. Otani, *Physical Review B* **96**, no. 14 (2017).

Chapter 2

Theory

In this chapter, we summarize the theory of Rashba effect, Edelstein effect, spin pumping, and spin-transfer torque ferromagnetic resonance (ST-FMR).

2.1 Rashba effect

In this section, the basic theory of Rashba effect is introduced.

2.1.1 Spin-orbit coupling

When an electron moving in an electric field $\boldsymbol{E}$ with momentum $\boldsymbol{p}$, in its rest frame there is an effective magnetic field $\boldsymbol{B}$ given by

$$\boldsymbol{B} = \frac{\boldsymbol{p} \times \boldsymbol{E}}{m_e^* c^2} \tag{2-1}$$

where $\boldsymbol{p}$, $\boldsymbol{E}$, m_e^*, and c are the momentum of electron, electric field, effective mass of electron, and speed of light, respectively. This effective field $\boldsymbol{B}$ induces a momentum-dependent Zeeman energy H_{soc} :

$$H_{soc} = \frac{\mu_B (\boldsymbol{p} \times \boldsymbol{E}) \cdot \boldsymbol{\sigma}}{2 m_e^* c^2} \tag{2-2}$$

where μ_B is Bohr magneton and $\boldsymbol{\sigma}$ is the electron spin, e.g. the Pauli matrices. There is an additional factor 1/2 known as Thomas correction when electron moves in closed orbits in atoms. By using the relation $\boldsymbol{E} = -\nabla V$ and $\mu_B = e\hbar/2m_e^*$, equation (2-2) becomes to

$$H_{soc} = \frac{\hbar}{4 {m_e^*}^2 c^2} \boldsymbol{\sigma} \cdot (\nabla V \times \boldsymbol{p}) \tag{2-3}$$

where V is the potential. This Zeeman energy H_{soc}, depending on the trajectory of the electron, is known as the spin-orbit coupling (SOC).

2.1.2 Inversion symmetry and spin degeneracy

Unrelativistic Schrodinger equation is generally used as the starting point for calculating a crystal band structure. Because there is no spin dependent term, the energy band calculated should be spin degenerate. This spin degeneracy can be lifted by adding any spin dependent Hamiltonian, i.e. Zeeman energy or spin-orbit coupling. Here we discuss the physics behind the spin degeneracy from the symmetry features of the system.

In quantum mechanics, the time reversal symmetry (operation t → -t) leads to

$$E(k,\uparrow) = E(-k,\downarrow) \tag{2-4}$$

where E and k is the energy and the wave number of electrons, respectively. ↑ and ↓ denote the state of spin up and down electron. Furthermore, the spatial inversion symmetry (operation $k \rightarrow -k$) leads to

$$E(k,\uparrow) = E(-k,\uparrow) \tag{2-5}$$

From eq. (2-4) and (2-5), if both time reversal and spatial inversion symmetry exist, the energy of spin up and down electron are degenerate,

$$E(k,\uparrow) = E(k,\downarrow) \tag{2-6}$$

This relation can be broken by time reversal symmetry breaking or by spatial inversion symmetry breaking. For example, in a system with time reversal symmetry but without spatial inversion symmetry, there is

$$E(k,\uparrow) \neq E(k,\downarrow) \tag{2-7}$$

Since there is no external magnetic field for breaking time reversal symmetry, the only origin of the energy splitting is the spin-orbit coupling, which can be described by eq. (2-3). This inversion symmetry breaking can come from the crystal structure or, more generally, the surface or interface state of any materials. This kind of SOC comes from the inversion symmetry breaking at 2-dimensional surface of interface state is called as Rashba SOC.

2.1.3 Free electron model

The Rashba splitting at metal surface is first observed at Au(111) surface by angle-resolved photoemission spectroscopy (ARPES) [2-1]. Fig. 2-1 shows the parabolic dispersion with the Rashba spin-splitting at Au(111) surface [2-1]. According to this free-electron-like dispersion, the surface state of metal can be considered as a 2-dimension (2D) free electron gas with Rashba SOC. Here, we assume that the 2D state is at x-y plane. Because the electrons are free in x-y plane, the potential gradient ∇V has only z-component, $\nabla V = (0,0,E_z)$. The resulting SOC Hamiltonian H_{soc} can be described by

$$H_{soc} = \alpha_R(\boldsymbol{k} \times \hat{\boldsymbol{z}}) \cdot \boldsymbol{\sigma} \tag{2-8}$$

$$\alpha_R = \frac{\hbar^2 E_z}{4m_e^{*2}c^2} \tag{2-9}$$

where α_R is so-called Rashba parameter, which determines the magnitude of spin-splitting. The total Hamiltonian of 2D electron gas is given by

$$H = H_p + H_{soc} = \frac{\boldsymbol{p}^2}{2m_e^*} + \alpha_R(k \times \hat{z}) \cdot \boldsymbol{\sigma} \tag{2-9}$$

The eigenvalue of this Hamiltonian is

$$E = \frac{k^2}{2m_e^*} \pm \alpha_R k = \frac{k^2}{2m_e^*} \pm \frac{\hbar^2 E_z}{4m_e^{*2}c^2} k \tag{2-10}$$

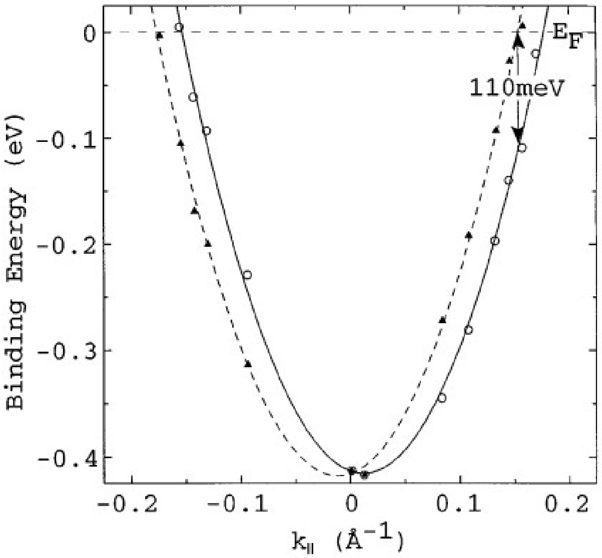

Figure 2-1. *E* vs *k* parabolic dispersion at Au(111) surface observed by ARPES [2-1]. The data is well fitted by eq. (2-10)

From eq. (2-9) and (2-10), there are two possible spin state of electrons. One is parallel to $\boldsymbol{k} \times \hat{\boldsymbol{z}}$ direction with energy $-\alpha_R k$, and another one is antiparallel to $\boldsymbol{k} \times \hat{\boldsymbol{z}}$ direction with energy $+\alpha_R k$. Fig. 2-2 shows the typical Rashba splitting and spin alignment. When there is no Rashba SOC, the spin up and down is degenerate. While Rashba SOC comes in, the spin bands are split and form a clockwise or anti-clockwise spin texture as shown in Fig. 2-2(b). This spin texture is known as the spin-momentum locking of Rashba effect.

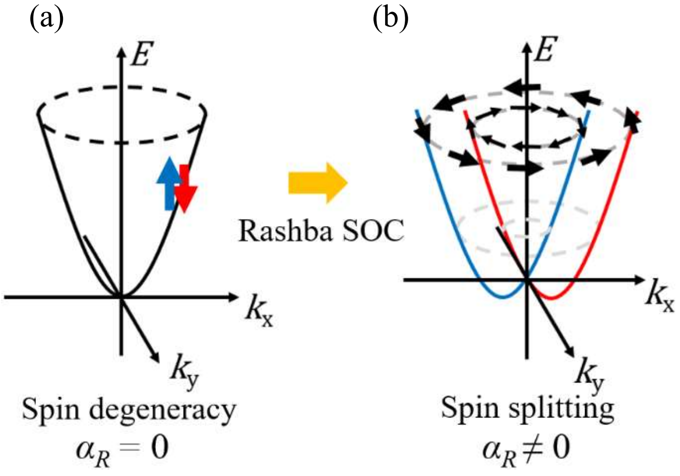

Figure 2-2. A schematic of typical Rashba spin-splitting and spin momentum locking at x-y plane.

The experiment data of the Rashba spin splitting at Au(111) surface is well fitted by eq. (2-10) as shown in Fig. 2-1. However, the magnitude of observed splitting energy $\Delta E = \alpha_R \mathrm{k}$ is much larger than the estimated value from $\alpha_R = \frac{\hbar^2 E_z}{4{m_e}^2 c^2}$. According to the calculation by Lang [2-2], a potential difference V between the surface and vacuum is in the order of work function Φ, and the region of the potential gradient dV/dz is around the Fermi wavelength λ_F. Thus, approximately there is $dV/dz = E_z \sim \Phi/\lambda_F$. In case of Au(111), using the reported value Φ=4.3 eV and λ_F~5 Å, ΔE becomes to 10^{-6} eV, which is 5 orders smaller than the experiment value ~110 meV. Authors of [2-1] confirmed that such small value is due to the artifact of the free electron model because the potential gradient in the Au atom is much larger than that comes from work function. Therefore, the dV/dz term in eq. (2-3) should include the contribution of the Coulomb force from metal nuclei and the contribution from work function.

2.1.4 Simple tight-binding model

Following the conclusion of Ref. [2-1], L. Petersen demonstrated a simple tight-binding model of Rashba effect in 1996. In this model, H_{soc} is derived from the Hamiltonian of p-state electrons near the nuclei and the Rashba splitting estimated is comparable to the experiment value. This tight-binding model indicates that a correct value of α_R can be obtained by considering the Coulomb force and the SOC of atoms. It is also found that the magnitude of Rashba spin-splitting is proportional to the strength of the atomic SOC.

The similar conclusion is obtained by the first-principle calculation performed by M. Nagano in 2009 [2-3]. In this study, a general form of α_R is derived. By using Rydberg atomic units, Eq. (2-3) can be rewritten to

$$H_{soc} = \frac{2}{c^2} \left(\nabla V \times \boldsymbol{p}\right) \cdot \boldsymbol{\sigma} \tag{2.10}$$

Here we consider a 2D surface/interface at x-y plane; momentum $\boldsymbol{p}$ can be divided into two terms, surface parallel component $\boldsymbol{p}_{\parallel}$ and surface perpendicular component $\boldsymbol{p}_{\perp}$, as

$$H_{soc} = \frac{2}{c^2} \left[\left(\nabla V \times \boldsymbol{p}_{\parallel}\right) \cdot \boldsymbol{\sigma} + \left(\nabla V \times \boldsymbol{p}_{\perp}\right) \cdot \boldsymbol{\sigma}\right] \tag{2.11}$$

The surface parallel part corresponds to Rashba Hamiltonian H_R. By assuming a 2D near-free-electron gas with $\boldsymbol{k} = (k_x, k_y)$, the wave function can be given by

$$\psi_{ss}^{k_{\parallel}}(\boldsymbol{r}) = \exp\{i(k_x\hat{\boldsymbol{x}} + k_y\hat{\boldsymbol{y}}\}\Phi(\mathrm{z}) \tag{2.12}$$

The Rashba splitting energy becomes

$$\varepsilon_R = \left\langle \psi_{ss}^{k_{\parallel}} \middle| H_{soc} \middle| \psi_{ss}^{k_{\parallel}} \right\rangle = \left|k_{\parallel}\right| \int d\boldsymbol{r} \frac{2}{c^2} \frac{\partial V}{\partial z} |\psi_{ss}^{k_{\parallel}}|^2 \tag{2.13}$$

The Rashba parameter is

$$\alpha_R = \frac{E_R}{\left|k_{\parallel}\right|} = \frac{2}{c^2} \int d\boldsymbol{r} \frac{\partial V}{\partial z} |\psi_{ss}^{k_{\parallel}}|^2 \tag{2.14}$$

From this equation, α_R is determined by the integral of potential gradient along z-direction times the z dependent electron distribution. M. Nagano calculated $|\psi_{ss}^{k_{\parallel}}|^2$ and the integrand of eq. (2.14) of Au(111) surface state from first-principle calculation as shown in Fig. 2-3. x-axis is the distance from surface atom and zero point is the position of surface atom. It is found that the non-zero value only appears in one Bohr around the surface atom, where the antisymmetric Coulomb term from the nucleus is dominant in $\partial V/\partial z$. This is known as the localized nature of Rashba effect. Since in this region the $\partial V/\partial z$ is antisymmetric, the asymmetric feature of $|\psi_{ss}^{k_\parallel}|^2$ determines both the magnitude and the sign of α_R.

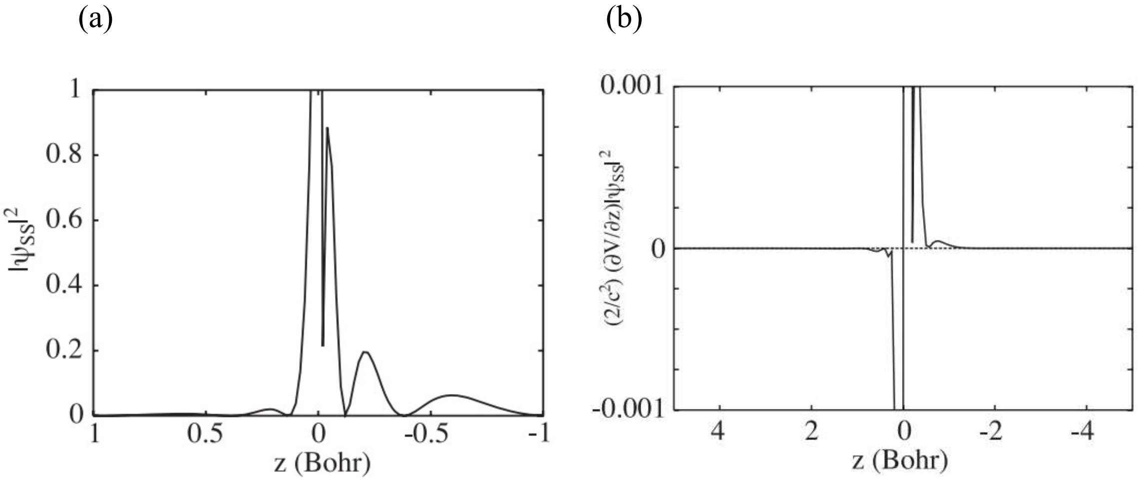

Figure 2-3 (a) $|\psi_{ss}^{k_\parallel}|^2$ at Au(111) surface along z-direction. (b) The integrand of eq. (2.14) along z-direction [2-3]

In conclusion, α_R is determined by, (i) $\partial V/\partial z$ from the Coulomb potential of nuclei, which is related to strength of SOC, (ii) localization of $|\psi_{ss}^{k_\parallel}|^2$, (iii) asymmetric feature of $|\psi_{ss}^{k_\parallel}|^2$. Note that though the surface potential gradient can be neglected in $\partial V/\partial z$ term, it is necessary for inducing the asymmetry of $|\psi_{ss}^{k_\parallel}|^2$. In addition, by comparing Au(111), Ag(111), and Sb(111) interfaces, M. Nagano confirmed that the shape of $|\psi_{ss}^{k_\parallel}|^2$ strongly depends on the hybridization state at the surface. Therefore, α_R cannot be determined by only atomic SOC and surface potential but also depend on the species and crystal structures of atoms [2-3].

2.2 Edelstein effect

In this section, the main topic of this thesis, the spin-charge interconversion via Edelstein effect, is described.

2.2.1 Direct Edelstein effect

As introduced in section 2.1.3, there is a spin-momentum locking effect at 2D Rashba system. When a charge current flows in this spin-momentum locking system, a spin accumulation will be generated and drive a diffusive spin current into an adjacent conductive layer. This charge-to-spin (C-S) conversion is called the direct Edelstein effect (DEE). A schematic of DEE is shown as Fig. 2-4 (a) and (b). Spin texture at Fermi energy can be mapped out in *k*-space as Fig. 2-4(a). When an electric field $-E_x$ is applied, the Fermi contour shifts in +x direction and a charge current flows. For the outer (inner) circle, a spin accumulation $\delta\sigma_{\uparrow}$ ($\delta\sigma_{\downarrow}$) is generated as shown in Fig. 2-4(b). Since there are more electron states at outer circle, totally a spin accumulation $\delta\sigma_{\uparrow}$ spin is generated and a diffusive spin current with y-direction spin flows into an adjacent conductive layer.

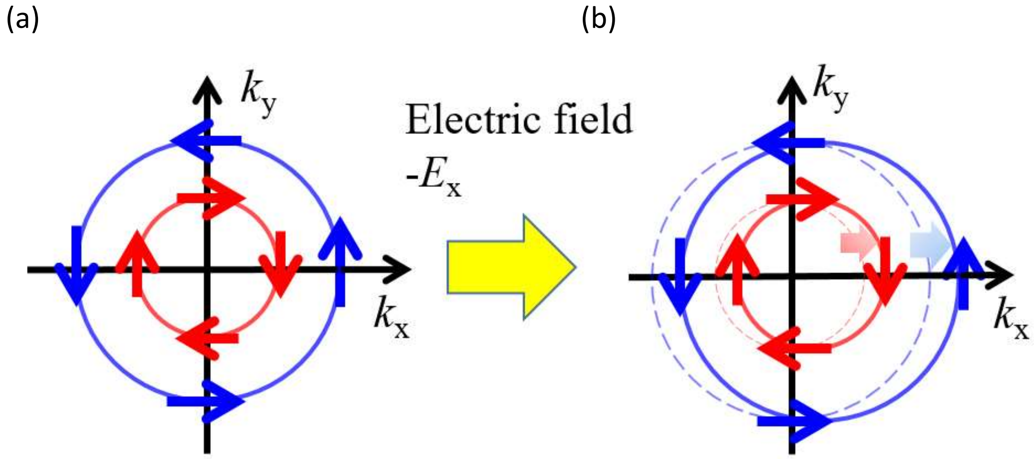

Figure 2-4 (a) Fermi contour with spin-momentum locking (b) Schematic of direct Edelstein effect.

The spin accumulation generated by DEE is demonstrated by P. Gambardella and I.M. Miron [2-5]. Firstly, the relation between the wave number and spin states of electrons at Fermi energy is calculated. The Hamiltonian in eq. (2-9) gives the eigenvectors

$$\psi_{\pm,\boldsymbol{k}} = \frac{e^{i\boldsymbol{k}\cdot\boldsymbol{r}}}{\sqrt{2A}}\begin{pmatrix}1\\ \mp ie^{i\xi_k}\end{pmatrix} \tag{2-15}$$

where $\boldsymbol{k} = k(\cos\xi, \sin\xi, 0)$ and A is the area of the 2D electron gas.

The spin expectation can be derived as

$$\langle\boldsymbol{\sigma}\rangle_{\pm,\boldsymbol{k}} = \langle\psi_{\pm,\boldsymbol{k}}|\boldsymbol{\sigma}|\psi_{\pm,\boldsymbol{k}}\rangle = \frac{1}{k}\begin{pmatrix}\pm k_y\\ \mp k_x\\ 0\end{pmatrix} = \begin{pmatrix}\pm\sin\xi\\ \mp\cos\xi\\ 0\end{pmatrix} \tag{2-16}$$

In Fig. 2-4(a), the radius of the outer circle and inner circle, $k_{\text{F}+}$ and $k_{\text{F}-}$, can be found by solving $\varepsilon_{-,k_{\text{F}-}} = \varepsilon_{+,k_{\text{F}+}} = \varepsilon_F$. By taking approximation to first order in α_R, this gives

$$k_{F\pm} \approx k_F\left(1 \mp \frac{m_e^*\alpha_R}{\hbar^2}\right) = k_F(1 \mp \beta) \tag{2-17}$$

where $\beta = \frac{m_e^*\alpha_R}{\hbar^2}$. This relation clearly demonstrates how the momentum of electrons depend on spin up or down state, e.g. $k_{F+} \neq k_{F-}$, which is the important feature of Rashba system.

Secondly, electric field inducing current density and spin accumulation are calculated. When an electric field E is applied, the Fermi contour is shifted by an amount of $\delta k_\pm = -eE\tau_e^\pm/\hbar$. were $\tau_e^\pm$ is the momentum relaxation time of spin up and down state. Note the τ_e^+ and τ_e^- is different because the momentum relaxation time generally depends on wavevector. For simplicity, it can be assumed that $\tau_e^\pm = \tau_e(1 \mp \beta)$ from eq. (2-17), where τ_e is the relaxation time of the 2D free-electron gas.

The Fermi-Dirac distribution of ± bands under electric field $\boldsymbol{E}$ is given by

$$f_{\pm,\mathbf{k}}^{shift} = (\partial f/\partial\varepsilon)e\tau_e^\pm v_{\pm,\mathbf{k}}\cdot\boldsymbol{E} \tag{2-18}$$

The current density contribution of ± bands can be calculated by Boltzmann equation.

$$\begin{aligned}\boldsymbol{j}_{\text{c}\pm} = -\frac{e}{4\pi^2}\int \mathbf{v}_{\pm,\mathbf{k}} f_{\pm,\mathbf{k}}^{shift} d\boldsymbol{k} &= -\frac{e}{4\pi^2}\int\left(\frac{\partial f}{\partial\varepsilon}\right)e\tau_e^\pm v_{\pm,\mathbf{k}}\mathbf{v}_{\pm,\mathbf{k}}\cdot\boldsymbol{E}d\boldsymbol{k}\\ &= -\frac{1}{4\pi^2}\frac{e^2\tau_e^\pm}{\hbar}\int_{S_{F\pm}}\frac{\mathbf{v}_{\pm,\mathbf{k}}}{v_{\pm,\mathbf{k}}}\mathbf{v}_{\pm,\mathbf{k}}\cdot\boldsymbol{E}dS_F\end{aligned} \tag{2-19}$$

where $S_{F\pm}$ denotes the integral over the two Fermi circles. By choosing $\boldsymbol{E} = E_{\boldsymbol{x}}$, the charge current density is

$$j_{\mathrm{c}\pm,x} = \frac{e^2\tau_e^{\pm}E}{4\pi^2\hbar}\int_0^{2\pi} v_{\mathrm{F}} cos^2\xi\, k_{F\pm} d\xi = \frac{e^2 E}{4\pi\hbar} v_{\mathrm{F}} k_{F\pm}\tau_e^{\pm} \tag{2-20}$$

Thus, the total current density becomes

$$j_{\mathrm{c}} = j_{\mathrm{c}+} + j_{\mathrm{c}-} = \frac{e^2 E}{2\pi\hbar} v_{\mathrm{F}} k_F \tau_e (1+\beta^2) \tag{2-21}$$

Similarly, the spin accumulation generated by electric field $\boldsymbol{E}$ can be calculated as

$$\begin{aligned}\langle\delta\boldsymbol{\sigma}\rangle_{\pm} &= \frac{1}{4\pi^2}\int \langle\boldsymbol{\sigma}\rangle_{\pm,\mathbf{k}} f_{\pm,\mathbf{k}}^{shift} d\boldsymbol{k} = \frac{1}{4\pi^2}\frac{-e\tau_e^{\pm}}{\hbar}\int_{S_{F\pm}} \frac{1}{k}\begin{pmatrix}\pm k_y\\ \mp k_x\\ 0\end{pmatrix}\frac{\mathbf{v}_{\pm,\mathbf{k}}}{v_{\pm,\mathbf{k}}}\mathbf{v}_{\pm,\mathbf{k}} \cdot \boldsymbol{E} dS_F \\ &= \frac{-e\tau_e^{\pm}E}{4\pi^2\hbar}\int_0^{2\pi}\begin{pmatrix}\pm\sin\xi\\ \mp\cos\xi\\ 0\end{pmatrix} cos\xi\, k_{F\pm} d\xi \;=\pm\frac{eE}{4\pi\hbar}\tau_e^{\pm} k_{F\pm}\hat{\boldsymbol{y}}\end{aligned} \tag{2-22}$$

The total spin accumulation is

$$\langle\delta\boldsymbol{\sigma}\rangle = \langle\delta\boldsymbol{\sigma}\rangle_{+} + \langle\delta\boldsymbol{\sigma}\rangle_{-} = \frac{-eE}{\pi\hbar} k_F \tau_e\, \beta\hat{\boldsymbol{y}} \tag{2-23}$$

Comparing to eq. (2-21), the relation between j_{c} and $\langle\delta\boldsymbol{\sigma}\rangle$ is

$$\langle\delta\boldsymbol{\sigma}\rangle = -\frac{m_e^*\alpha_R}{e\hbar\varepsilon_F} j_{\mathrm{c}}\,\hat{\boldsymbol{y}} \tag{2-24}$$

Note that, in a 2-dimensional system, $\langle\delta\boldsymbol{\sigma}\rangle$ is in units of m^{-2}, and j_c is in units of A m^{-1}. The spin accumulation $\langle\delta\boldsymbol{\sigma}\rangle$ can drive a diffusive spin current $j_{\mathrm{s\_DEE}}$ into adjacent conductive layer. By considering a total spin relaxation time in this process, τ_{DEE}, j_{s} can be described by

$$j_{\mathrm{s}}{}^{3D}/e = \langle\delta\sigma\rangle/\tau_{\mathrm{DEE}} \tag{2-25}$$

According to Ref. [2-6], τ_{DEE} should consist two contribution, tunneling time of spin from interface to bulk and spin scattering time in bulk. Because this spin current flows in 3D bulk layer while the charge current flows in 2D Rashba state, we denote them as $j_{\mathrm{s}}{}^{3D}$ and

${j_\mathrm{c}}^{2D}$. From eq. (2-23) and (2-24) with $\varepsilon_F = \frac{1}{2} m_e^* {v_\mathrm{F}}^2$, the charge-to-spin conversion efficiency q_DEE is given by

$$q_{DEE} \equiv \frac{{j_\mathrm{s}}^{3D}}{{j_\mathrm{c}}^{2D}} = \frac{\alpha_\mathrm{R}}{{v_\mathrm{F}}^2 \hbar \tau_\mathrm{DEE}} \tag{2-26}$$

2.2.2 Inverse Edelstein effect

There is also a reverse effect of DEE that injecting the spin current into the interface generates a charge current. This phenomenon is known as inverse Edelstein effect (IEE). For example, a schematic of IEE is shown as Fig. 2-5. When a spin current with y-direction spin polarization is injected into the 2D Rashba state, a spin accumulation $\delta\sigma_y$ will be generated at both outer and inner circle. Due to the spin-momentum locking, there should be a shift of the fermi contour otherwise the spin accumulation cannot be generated. As the results, the outer circle and inner circle is shifted to the +x and –x direction. Totally, the electrons gain some momentum at k_x direction and a charge current is generated from spin current.

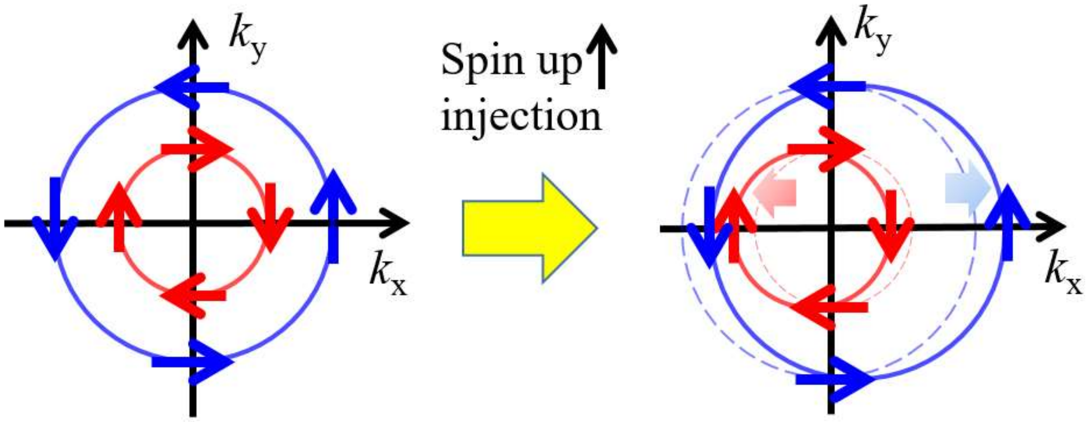

Figure 2-5 Schematic of Inverse Edelstein effect.

To obtain the spin-to-charge conversion, firstly, we introduced a simple model according to Ref [2-7]. From eq. (2-20) and (2-22), the relation between 2D spin accumulation $\langle \delta\boldsymbol{\sigma} \rangle_\pm$ and 2D charge current density $j_{\mathrm{c}\pm}$ is

$$\langle\delta\sigma\rangle_{\pm} = \pm\frac{1}{ev_{\mathrm{F}}}j_{\mathrm{c}\pm} = \pm\frac{m_e^*}{e\hbar k_{F\pm}}j_{\mathrm{c}\pm} \tag{2-27}$$

The splitting between outer circle and inner circle is

$$\Delta k = k_{F+} - k_{F-} = 2\beta = \frac{2m_e^*\alpha_R}{\hbar^2} \tag{2-28}$$

gives the 2D charge current density associated with the total 2D spin density$\langle\delta\boldsymbol{\sigma}\rangle = \langle\delta\boldsymbol{\sigma}\rangle_+ + \langle\delta\boldsymbol{\sigma}\rangle_-$

$$j_c = \frac{e\alpha_{\mathrm{R}}}{\hbar}\langle\delta\sigma\rangle \tag{2-29}$$

In IEE case, the spin accumulation $\langle\delta\sigma\rangle$ at the Rashba states is generated by the injected 3D spin current. By considering a spin relaxation time τ_{IEE} of Rashba state with spin-momentum locking, the relation between injected ${j_{\mathrm{s}}}^{3D}$ and $\langle\delta\sigma\rangle$ is

$${j_{\mathrm{s}}}^{3D}/e = \langle\delta\sigma\rangle/\tau_{\mathrm{IEE}} \tag{2-30}$$

Note that here τ_{IEE} is spin relaxation process at 2D Rashba state, therefore it is different with τ_{DEE}.

From eq. (2-29) and (2-30), the spin-to-charge conversion efficiency λ_{IEE} is

$$\lambda_{\mathrm{IEE}} \equiv \frac{{j_{\mathrm{c}}}^{2D}}{{j_{\mathrm{s}}}^{3D}} = \frac{\alpha_{\mathrm{R}}\tau_{\mathrm{IEE}}}{\hbar} \tag{2-31}$$

Furthermore, K. Shen demonstrate another derivation of λ_{IEE} by using a drift-diffusion equations model [2-8]. When a spin current with y-direction spin polarization, ${J_{\mathrm{s}}}^{y}$, injected into Rashba state, the coupled equtions of charge and spin currents are in a form introduced in Ref [2-9]:

$$\frac{d\langle\delta\sigma^y\rangle}{\mathrm{d}t} = -2m_e^*\alpha_{\mathrm{R}}J_y^z - \frac{\delta\sigma^y}{\tau_{\mathrm{sf}}} + \chi_s\frac{dB^y}{dt} \tag{2-32}$$

$$J_y^{Sz} = 2m_e^*\alpha_{\mathrm{R}}D\,\delta\sigma^y + \theta_{SH}J_x \tag{2-33}$$

$$J_x = -\theta_{SH}J_y^z \tag{2-34}$$

where $\langle \delta\sigma^y \rangle$ is the spin accumulation in y-direction polarization, τ_{sf} is the spin relaxation time of the system, D is the drift constant, θ_{SH} is the spin Hall angle, and J_x is the charge current density. J_y^{Sz} denote the spin current with z-direction polarization flowing in y-direction. In addition, because the $\chi_s B^y$ correspond to an additional spin accumulation σ^y, $\chi_s(dB^y/dt)$ is actually the spin density injected, $\chi_s(dB^y/dt) = J_{\mathrm{s}}{}^y$. Solving the eq. (2-32) ~ (2-34), we have

$$\langle \delta\sigma^y \rangle = \frac{\tau_{\mathrm{sf}}}{1 - i\omega\tau_{\mathrm{sf}}} \cdot J_{\mathrm{s}}{}^y \tag{2-35}$$

$$J_y^{Sz} = 2m_e^* \alpha_{\mathrm{R}} D \frac{\tau_{\mathrm{sf}}}{1 - i\omega\tau_{\mathrm{sf}}} \cdot J_{\mathrm{s}}{}^y \tag{2-36}$$

$$J_x = -\frac{2\pi}{e} \alpha_{\mathrm{R}} \sigma_{SH} \frac{\tau_{\mathrm{sf}}}{1 - i\omega\tau_{\mathrm{sf}}} \cdot J_{\mathrm{s}}{}^y \tag{2-37}$$

where σ_{SH} is the spin Hall conductivity related with θ_{SH}. Thus, the spin-to-charge conversion efficiency λ_{IEE} is

$$\lambda_{\mathrm{IEE}} \equiv \frac{J_x}{J_{\mathrm{s}}{}^y} = -\frac{2\pi}{e} \alpha_{\mathrm{R}} \sigma_{SH} \frac{\tau_{\mathrm{sf}}}{1 - i\omega\tau_{\mathrm{sf}}} \tag{2-38}$$

According to Ref. [2-8], the spin Hall conductivity is $\sigma_{SH} = -(e/8\pi)/(4\tau_p/\tau_{\mathrm{sf}})$, where τ_p^{int} is the momentum relaxation time at Rashba state. In the low frequency limit, eq. (2-38) leads to $\lambda_{\mathrm{IEE}} = \alpha_{\mathrm{R}} \tau_p$. Because the natural unit is used in this calculation which let $\hbar = 1$, λ_{IEE} can be described by

$$\lambda_{\mathrm{IEE}} = \frac{\alpha_{\mathrm{R}} \tau_p}{\hbar} \tag{2-39}$$

Note that in eq. (2-31), the λ_{IEE} is proportional to a spin relaxation time but not τ_p, which is different with eq. (2-31). This is because eq. (2-39) is derived from the weak spin-orbit limit (diffusive regime), while in the strong spin-orbit system, the momentum relaxation process actually dominant the spin relaxation time, therefore $\tau_{\mathrm{IEE}} = \tau_p$ [2-7].

2.2.3 Different time scale in DEE and IEE

As introduced in section 2.2.1 and 2.2.2, for C-S conversion via DEE, the conversion efficiency is $q_{DEE} = \alpha_{\mathrm{R}}/({v_{\mathrm{F}}}^2\hbar\tau_{\mathrm{DEE}})$. For S-C conversion via IEE, the efficiency is $\lambda_{\mathrm{IEE}} = \alpha_{\mathrm{R}}\tau_{\mathrm{IEE}}/\hbar = \alpha_{\mathrm{R}}\tau_p/\hbar$. We would like to emphasize that, though τ_{DEE} and τ_{IEE} are both spin relaxation time, this two time are different due to the different spin relaxation process. For a spin accumulation at 2D Rashba system, there are two possible process of spin relaxation. The first one is the spin relaxation occurred by the momentum scattering in 2D Rashba system. Fig. 2.6(a) shows a schematic of spin relaxation process with the spin-momentum locking. When electron scattering happens, both the direction and magnitude of the electron momentum is changed. Due to the spin-momentum locking, the electron feels a large effective Rashba field during the scattering and the spin relaxation takes place. Besides the relaxation in 2D state, the spin accumulation can also escape from the Rashba system to the 3D adjacent layer, which becomes the second spin relaxation process as shown in Fig. 2.6(b).

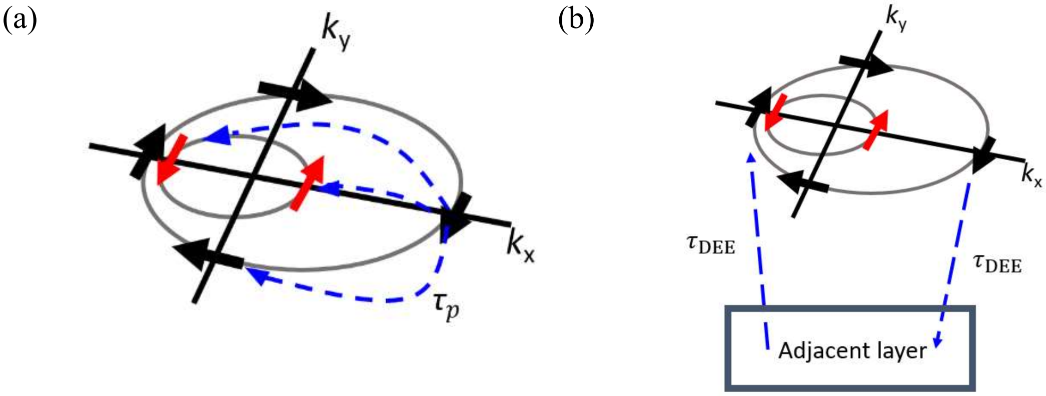

Figure 2-6. (a) Spin relaxation process at 2D Rashba state. (b) Spin relaxation due to the escaping spins from 2D Rashba state to the adjacent layer.

In the experiment of DEE, spin accumulation is generated by injecting 2D charge current $j_{\mathrm{c}}^{\mathrm{2D}}$ into 2D Rashba state. Since the shift of Fermi contour is already determined by the magnitude of charge current, the amount of spin accumulation is not related with momentum relaxation time, which is shown in eq. (2.24). This spin accumulation drives a 3D spin current $J_{\mathrm{s}}^{\mathrm{3D}}$ through the process in Fig. 2-6(b) and this process is known as DEE.

Thus, in DEE the spin relaxation time τ_{DEE} is related to the spin relaxation during the transition between interface and bulk and the spin scattering in the bulk.

In the experiment of IEE, spin accumulation is generated by injecting spin current $J_s^{3\mathrm{D}}$ into Rashba state. The amount of spin accumulation generated is related to the spin relaxation time as described by eq. (2-30). In this case both two of relaxation process should occur at the same time. However, the spin escaping or diffusion process in Fig. 2-6(b) actually generates a backflow of spin current, which corresponds to a decreasing of injected spin current. Generally, in spin pumping measurement, the definition of injected spin current at 2D Rashba state is $J_s^{inject} = J_s^{total} - J_s^{backflow}$, where J_s^{inject} is the injected spin current, J_s^{total} is the total generated spin current from ferromagnetic layer, and $J_s^{backflow}$ is the backflow of spin current. Therefore, if we calculate λ_{IEE} from $\lambda_{\mathrm{IEE}} = j_{\mathrm{c}}{}^{2D}/J_s^{inje}$, the spin diffusion process of Fig. 2-6(b) is automatically considered in the calculation. Thus, τ_{IEE} only depend on momentum relaxation τ_p at Rashba state. One can also use another definition that $\lambda_{\mathrm{IEE}} = j_{\mathrm{c}}{}^{2D}/J_s^{total}$ where the backflow of spin current is not included in the calculation. Since J_s^{total} is larger than J_s^{inject}, λ_{IEE} becomes smaller in this definition. In this case, both two relaxation processes should be included in the τ_{IEE}; that is, $(\tau_{\mathrm{IEE}})^{-1} = \left(\tau_{\mathrm{p}}\right)^{-1} + (\tau_{DEE})^{-1}$. Thus, τ_{IEE} is shorter than τ_{p} and τ_{DEE}. Since in spin pumping measurement, only J_s^{inject} can be estimated directly from experiment, the definition $\lambda_{\mathrm{IEE}} = j_{\mathrm{c}}{}^{2D}/J_s^{inject}$ with $\lambda_{\mathrm{IEE}} = \alpha_{\mathrm{R}}\tau_p/\hbar$ is much more suitable for experiments. In this thesis, we will use this definition for IEE conversion efficiency.

2.3 Spin pumping

A precessing magnetic moment of magnetic materials acts as a source of spin angular momentum and pumped a spin current into the adjacent non-magnetic material. This effect is known as spin pumping. Here, we start with a basic concept of spin pumping and introduced the theory description of spin pumping developed by Y. Tserkovnyak and A. Brataas [2-10 ,2-11].

The magnetization dynamics of a bulk ferromagnetic materials can be described by the Landau-LifshitzGilbert (LLG) phenomenological equation [2-12]

$$\frac{d\boldsymbol{m}}{dt} = -\gamma\boldsymbol{m} \times \boldsymbol{H}_{eff} + \delta\boldsymbol{m} \times \frac{d\boldsymbol{m}}{dt} \tag{2-40}$$

where $\boldsymbol{m}$ is the direction of magnetization, γ is gyromagnetic ratio, $\boldsymbol{H}_{eff}$ is the effective magnetic field, and $\boldsymbol{\alpha}$ is so-called Gilbert damping constant. When $\boldsymbol{H}_{eff}$ is constant and δ is zero, the magnetization precessess around $\boldsymbol{H}_{eff}$ with frequency $\omega = \gamma\boldsymbol{H}_{eff}$. When δ>0, the damping process gradually decrease the cone angle of precession motion and forces the magnetization $\boldsymbol{m}$ aligned to the direction of $\boldsymbol{H}_{eff}$**.** It has been known that in experiment, when a ferromagnetic material contacts with a non-magnetic metal, the damping constant will be enhanced. This enhancement can be explained by considering the spin current generated from ferromagnetic materials. In eq. (2-40), the precession $d\boldsymbol{m}/dt$ induced by the torque $= -\gamma\boldsymbol{m} \times \boldsymbol{H}_{eff}$ is physically equivalent to a spin current. Thus, the damping term can be understood as a leakage of spin current. When there is an adjacent normal metal layer, the spin current is allowed to leak into the metal layer and therefore enhance the damping in the ferromagnetic material. The spin current flowing into normal metal layer will generate a spin accumulation which results in a back blow of spin current $\boldsymbol{I}_s^{back}$. By assuming the normal metal layer is an ideal sink of spin current and $\boldsymbol{I}_s^{back} = 0$, Y. Tserkovnyak demonstrated that spin current pumped from FM layer $\boldsymbol{I}_s^{pump}$ is

$$\boldsymbol{I}_s^{pump} = \frac{\hbar}{4\pi} g^{\uparrow\downarrow} \left[\boldsymbol{m} \times \frac{d\boldsymbol{m}}{dt}\right] \tag{2-41}$$

where $g^{\uparrow\downarrow}$ is so-called spin mixing conductance.

From eq. (2-41), it is clear that the spin direction of the pumped spin current is time dependent. Fig. 2-7 shows the schematic of spin pumping mechanism described by eq. (2-41). $[\boldsymbol{m} \times d\boldsymbol{m}/dt]$ term always has a component in the direction of effective field, by choosing the effective field in z-direction, the average dc spin current J_s with the spin direction z is:

$$J_s = \frac{\omega}{2\pi} \int_0^{2\pi/\omega} \frac{\hbar}{4\pi} g_{eff}^{\uparrow\downarrow} \frac{1}{M_s} \left[\boldsymbol{m} \times \frac{d\boldsymbol{m}}{dt}\right]_z \tag{2-42}$$

here $[\boldsymbol{m} \times d\boldsymbol{m}/dt]_z$ denotes the z component of $[\boldsymbol{m} \times d\boldsymbol{m}/dt]$.

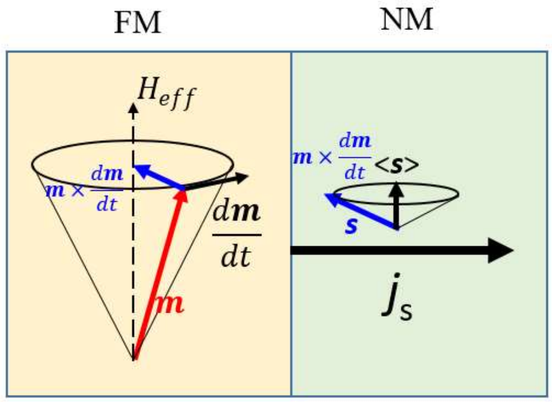

Figure. 2-7. A schematic of the spin current generated by spin pumping from the interface of ferromagnets(FM) and normal metal(NM)

Based on eq. (2-42), K. Ando et al. derive a phenomenological formulation of spin current by solving LLG equation [2-13].

Firstly, we consider an equilibrium condition of ferromagnetic layer under external field $\boldsymbol{H}$ as shown in Fig. 2-8. By taking into account the static demagnetizing field $\boldsymbol{H}_M$ induced by $\boldsymbol{M}$, the effective magnetic field $\boldsymbol{H}_{eff}$ is

$$\boldsymbol{H}_{eff} = \boldsymbol{H} + \boldsymbol{H}_M \tag{2-43}$$

$\boldsymbol{H}$ and $\boldsymbol{H}_M$ is :

$$\boldsymbol{H} = \begin{pmatrix} 0 \\ sin(\theta_M - \theta_H) \\ cos(\theta_M - \theta_H) \end{pmatrix} \quad , \quad \boldsymbol{H_M} = -4\pi M_s \begin{pmatrix} 0 \\ sin\theta_M \\ cos\theta_M \end{pmatrix}$$

where θ_M is the angle between $\boldsymbol{M}$ and the out-of-plane direction (y' axis), θ_H is the angle between $\boldsymbol{H}$ and y' axis. In the static equilibrium condition, there is $\boldsymbol{M} \times \boldsymbol{H}_{eff} = 0$, which gives the relation

$$2Hsin(\theta_M - \theta_H) + 4\pi M_s sin2\theta_M = 0 \tag{2-45}$$

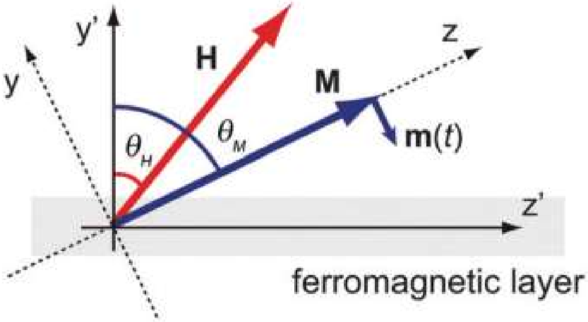

Figure. 2-8 A schematic of magnetization ***M*** and external field ***H*** of a ferromagnetic layer.

By applying an rf magnetic field $\boldsymbol{h}_{rf}(t)$ in x axis to excite the ferromagnetic resonance, magnetization $\boldsymbol{M}(t)$ precessing around z-axis can be describe by $\boldsymbol{M}(t) = \boldsymbol{M} + \boldsymbol{m}(t)$, where $\boldsymbol{M}$ and $\boldsymbol{m}(t)$ are the static and the dynamic components of the magnetization respectively. Take into accout the demagnetizing field $\boldsymbol{H}_{\mathrm{m}}(t)$ induced by $\boldsymbol{m}(t)$, the effective field $\boldsymbol{H}_{eff}$ is

$$\boldsymbol{H}_{eff} = \boldsymbol{H} + \boldsymbol{H}_M + \boldsymbol{H}_{\boldsymbol{m}}(t) + \boldsymbol{h}_{rf}(t) \qquad \text{(2-46)}$$

$\boldsymbol{H}_{\boldsymbol{m}}(t)$ and $\boldsymbol{h}_{rf}(t)$ are

$$\boldsymbol{H}_{\boldsymbol{m}}(t) = -4\pi m_y(t) sin\theta_M \begin{pmatrix} 0 \\ sin\theta_M \\ cos\theta_M \end{pmatrix} \quad , \quad \boldsymbol{h}_{rf}(t) = \begin{pmatrix} he^{i\omega t} \\ 0 \\ 0 \end{pmatrix}$$

Solving LLG equation below can give us the exact $\boldsymbol{M}(t)$:

$$\frac{d\boldsymbol{M}(t)}{dt} = -\gamma \boldsymbol{M}(t) \times \boldsymbol{H}_{eff} + \frac{\delta}{\boldsymbol{M}_s} \boldsymbol{M}(t) \times \frac{d\boldsymbol{M}(t)}{dt} \qquad \text{(2-47)}$$

A small precession of $\boldsymbol{m}(t) = \left(m_x e^{i\omega t}, m_y e^{i\omega t}, 0\right)$ around the z-axis is assumed as a solution of eq. (2-46). Here, $\omega = 2\pi f$, where f is the frequency of rf field. The ferromagnetic resonance condition is found as

$$\left(\frac{\omega}{\gamma}\right)^2 = [H_R cos(\theta_M - \theta_H) - 4\pi M_s cos2\theta_M][H_R cos(\theta_M - \theta_H) - 4\pi M_s cos^2\theta_M] \quad \text{(2-48)}$$

where H_R is the resonance field.

By using eq. (2-45), (2-48) to solve LLG equation, there is

$$m_x(t) = \frac{4\pi M_s}{8\pi\delta\omega}\frac{\left\{2\delta\omega\cos\omega t + \sin\omega t\left[4\pi M_s \sin^2\theta_M + \sqrt{(4\pi M_s)^2\gamma^2\sin^4\theta_M + 4\omega^2}\right]\right\}}{\sqrt{(4\pi M_s)^2\gamma^2\sin^4\theta_M + 4\omega^2}} \tag{2-49}$$

$$m_y(t) = -\frac{4\pi M_s h\gamma \cos\omega t}{4\pi\delta\sqrt{(4\pi M_s)^2\gamma^2\sin^4\theta_M + 4\omega^2}} \tag{2-50}$$

Insert eq. (2-49) and (2-50) into eq. (2-42), spin current density is

$$J_s = \frac{\hbar g_{\mathrm{eff}}^{\uparrow\downarrow}\gamma^2 {h_{\mathrm{rf}}}^2\left[4\pi M_s\gamma\sin^2\theta_M + \sqrt{(4\pi M_s)^2\gamma^2\sin^4\theta_M + 4\omega^2}\right]}{8\pi\delta^2\left[(4\pi M_s)^2\gamma^2\sin^4\theta_M + 4\omega^2\right]} \tag{2-51}$$

If $\boldsymbol{M}$ is at in-plane direction, $\theta_M = \pi/2$, j_s becomes to

$$J_s = \frac{\hbar g_{\mathrm{eff}}^{\uparrow\downarrow}\gamma^2 {h_{\mathrm{rf}}}^2\left[4\pi M_s\gamma + \sqrt{(4\pi M_s)^2\gamma^2 + 4\omega^2}\right]}{8\pi\delta^2\left[(4\pi M_s)^2\gamma^2 + 4\omega^2\right]} \tag{2-52}$$

which is the formula we used in this thesis.

2.4 Spin-torque ferromagnetic resonance

The magnetization of ferromagnets keeps its precession motion in FMR with a damping constant δ. In spin pumping, a spin current leaking from FM layer to NM layer leading to an enhanced δ. In contrast, a spin current generated from NM layer by charge-to-spin conversion flowing into the FM layer can lead to a spin-transfer torque to the magnetization which modulates the resonance properties damping constant of FMR, i.e. damping constant. This process is called spin-torque (ST) FMR, which can be understood as a reverse effect of spin pumping. ST-FMR method enables us to estimate the injected spin current by measuring the DC voltage from the change of anisotropic magnetoresistance (AMR) in FM layer. Here we introduce the basic theory and analysis method demonstrated by L. Liu, *et al*. [2-14].

The LLG equation containing the spin torque term with a rf current is [2-15]:

$$\frac{d\boldsymbol{m}}{dt} = -\gamma \boldsymbol{m} \times \boldsymbol{H}_{eff} + \delta \boldsymbol{m} \times \frac{d\boldsymbol{m}}{dt} + \gamma \frac{\hbar}{2e\mu_0 M_s t} \times J_{s.rf}(\boldsymbol{m} \times \boldsymbol{\sigma} \times \boldsymbol{m}) - \gamma \boldsymbol{m} \times \boldsymbol{H}_{rf} \tag{2-53}$$

Here μ_0 is the permeability in vacuum, M_s is the saturation magnetization of FM, t is the thickness of the FM layer. $J_{s.rf}$ is ac spin current density injected into Py, $\boldsymbol{H}_{rf}$ is the Oersted field generated by the rf current, and $\boldsymbol{\sigma}$ is the direction of injected spin current. We consider a rf current flowing in a bilayer structure ferromagnet and spin Hall material, i.e. Py/Pt, as shown in Fig. 2-9. Second term in eq. (2-52), a damping torque, is shown as $\boldsymbol{\tau}_{\alpha}$. Rf current flowing in the bilayer at x-direction generates $\boldsymbol{H}_{rf}$ at y-direction and also a spin current with $\boldsymbol{\sigma}$ in y-direction. Therefore, the third term of eq. (2-53) becomes a spin-transfer torque at in-plane direction, which is shown as $\boldsymbol{\tau}_{\mathrm{STT}}$, while the fourth term is a Oersted field torque at out-of-plane direction, which is shown as $\boldsymbol{\tau}_{\mathrm{H}}$. These two torques, $\boldsymbol{\tau}_{\mathrm{STT}}$ and $\boldsymbol{\tau}_{\mathrm{H}}$ change the magnetization direction $\boldsymbol{m}$ and result in AMR which can be electrically detected by measuring voltage.

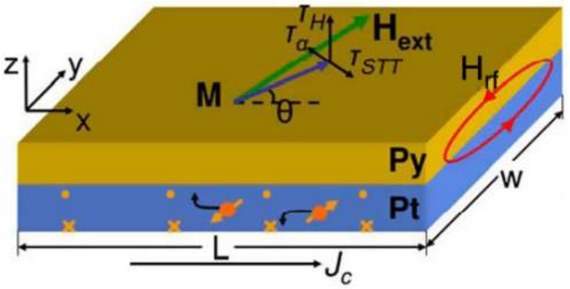

Figure. 2-9 Schematic of a Pt/Py bilayer thin film with the illustration of spin-transfer $\boldsymbol{\tau}_{\mathrm{STT}}$, Oersted field torque $\boldsymbol{\tau}_{\mathrm{H}}$, and damping torque $\boldsymbol{\tau}_{\alpha}$ [2-14].

The contribution of $\boldsymbol{\tau}_{\mathrm{STT}}$ and $\boldsymbol{\tau}_{\mathrm{H}}$ in AMR can be separated by analyzisng the symmetric and antisymmetric part of the voltage spectrum. The typical voltage spectrum of ST-FMR is shown as Fig. 2-10.

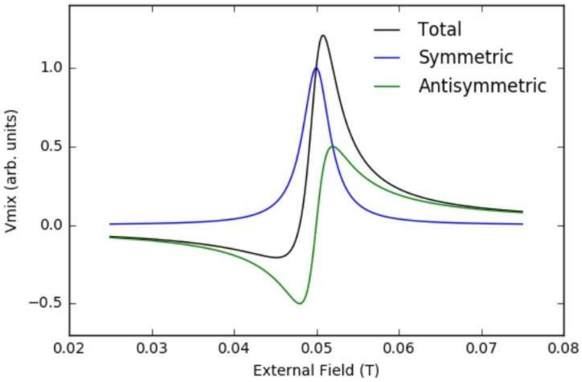

Figure. 2-10. Schematic of voltage spectrum of ST-FMR consisting of a symmetric contribution and antisymmetric contribution.

The mixing voltage signal spectrum in response to a combination of in-plane and out-of-plane torques has been calculated as [2-15, 16]

$$V_{mix} = -\frac{1}{4}\frac{dR}{d\theta}\frac{\gamma I_{rf} cos\theta}{\Delta 2\pi (df/dH)|_{H_{ext}=H_0}}[SF_s(H_{ext}) + AF_A(H_{ext})] \tag{2-54}$$

and

$$F_s(H_{ext}) = \Delta^2/[\Delta^2 + (H_{ext} - H_0)^2]\,, S = \hbar J_{s,rf}/2e\mu_0 M_s t$$

$$F_A(H_{ext}) = F_s(H_{ext})(H_{ext} - H_0)/\Delta\,, A = H_{rf}\sqrt{1 + (4\pi M_{eff}/H_{eff})}$$

The contribution of $\boldsymbol{\tau}_{\mathrm{STT}}$ is $SF_s(H_{ext})$, a symmetric Lorentzian function with resonance field H_0 and linewidth Δ, while the contribution of $\boldsymbol{\tau}_{\mathrm{H}}$ is $AF_A(H_{ext})$, an antisymmetric Lorentizain function. Here, R, I_{rf}, and f are the resistance of the bilayer, the rf current, and the resonance frequency, respectively. By fitting the voltage spectrum with eq. (2-54), the parameters, H_0, Δ, S, and A can determined. Assuming that the microwave skin depth is much greater than the Py thickness, in this case the Oersted field from the charge current in the Py have no net torque in Py. Thus, the Oersted field can be calculated from the charge current density $J_{c,rf}$ in the Pt layer, $H_{rf} = J_{c,rf}d/2$, where d is the thickness of Pt layer. The ratio between and $J_{c,rf}$, the charge-to-spin conversion efficiency or the spin Hall angle, can be described by

$$\frac{J_{s,rf}}{J_{c,rf}} = \frac{S}{A}\frac{e\mu_0 M_s td}{\hbar}\sqrt{1 + (4\pi M_{eff}/H_{eff})} \tag{2-55}$$

From this analysis, it seems that the spin Hall angle depends on the thickness of ferromagnetic layer *d*. In experiment, the thickness dependence of FM layer on the SHA is reported at the Py/Pt and Py/Pd systems [2-17]. Since the spin Hall angle (SHA) should be an intrinsic characteristic of SHE, this thickness dependence suggests that there may be some additional signals coming from the rf curret flowing in FM layer. Therefore, it is difficult to estimate a correct value of SHA from eq. (2-55). To solve this problem, there is an alternative way of determining charge-to-spin conversion efficiency by applying additional dc charge current for modulating damping constant in FM layer. According to the theory of spin-transfer torque, a dc spin current generated from dc charge current will modulated the damping constant of FMR in FM layer. The relation between damping constant and spin current injected is [2-18]

$$\Delta\delta = \frac{sin\theta}{(H_{ext} + 2\pi M_{eff})\mu_0 M_s t}\frac{\hbar J_s}{2e} \tag{2-56}$$

By fitting the voltage spectrum with eq. (2-54) the linewidth Δ can be determined, and the damping constant can be derived by the frequency dependence of linewidth from the relation $\Delta = 2\pi f\delta/\gamma + \Delta_0$. Then, from the relation between δ and dc charge current density J_c, the ratio $J_{s,dc}/J_{c,dc}$ can be estimated. In this thesis, we use the ST-FMR measurement with the modulation of damping constant to determine the charge-to-spin conversion coefficient.

Reference of chapter 2

[2-1] S. LaShell, B. McDougall and E. Jensen, *Physical Review Letters* **77**, no. 16, pp. 3419-3422 (1996)

[2-2] N.D. Lang, *Solid State Physics* **28**, no. 225 (1973)

[2-3] M. Nagano, A. Kodama, T. Shishidou and T. Oguchi, *J. Phys. Condens. Matter.* **21**, no. 6, p. 064239 (2009)

[2-4] C. Ast, J. Henk, A. Ernst, L. Moreschini, M. Falub, D. Pacilé, P. Bruno, K. Kern and M. Grioni, *Physical Review Letters* **98**, no. 18 (2007).

[2-5] P. Gambardella and I. Miron, *Philosophical Transactions of the Royal Society A: Mathematical, Physical and Engineering Sciences* **369**, no. 1948, pp. 3175-3197, 2011.

[2-6] S. Zhang and A. Fert, *Physical Review B* **94**, no. 18 (2016).

[2-7] J. Sánchez, L. Vila, G. Desfonds, S. Gambarelli, J. Attané, J. De Teresa, C. Magén and A. Fert, *Nature Communications* **4**, no. 1 (2013).

[2-8] K. Shen, G. Vignale and R. Raimondi, *Physical Review Letters* **112**, no. 9, (2014).

[2-9] C. Gorini, P. Schwab, R. Raimondi and A. Shelankov, *Physical Review B* **82,** no. 19 (2010).

[2-10] Y. Tserkovnyak, A. Brataas and G. Bauer, *Physical Review Letters* **88**, no. 11 (2002).

[2-11] Y. Tserkovnyak, A. Brataas and G. Bauer, *Physical Review B* **66**, no. 22 (2002).

[2-12] L. D. Landau, E. M. Lifshitz, and L. P. Pitaevski, *Statistical Physics*, Part 2, 3rd ed. (1980).

[2-13] K. Ando, S. Takahashi, J. Ieda, Y. Kajiwara, H. Nakayama, T. Yoshino, K. Harii, Y. Fujikawa, M. Matsuo, S. Maekawa and E. Saitoh, *Journal of Applied Physics* **109**, no. 10, p. 103913 (2011).

[2-14] L. Liu, T. Moriyama, D. Ralph and R. Buhrman, *Physical Review Letters* **106**, no. 3 (2011).

[2-15] J. Slonczewski, *Journal of Magnetism and Magnetic Materials* **159**, no. 1-2, pp. L1-L7 (1996).

[2-16] J. Sankey, Y. Cui, J. Sun, J. Slonczewski, R. Buhrman and D. Ralph, *Nature Physics* **4**, no. 1, pp. 67-71 (2007).

[2-17] K. Kondou, H. Sukegawa, S. Mitani, K. Tsukagoshi and S. Kasai, *Applied Physics Express* **5**, no. 7, p. 073002 (2012).

[2-18] S. Kasai, K. Kondou, H. Sukegawa, S. Mitani, K. Tsukagoshi and Y. Otani, *Applied Physics Letters* **104**, no. 9, p. 092408 (2014).

Chapter 3

Method

In this chapter, we summarize the fabrication processes of samples and devices in this study, and then introduce the experiment setup of spin pumping and spin torque ferromagnetic resonance (ST-FMR) measurement. At last, we describe the first-principle calculation method.

3.1 Sample fabrication

3.1.1 Lift off method

Fig. 3-1 simply shows the fabrication steps (Lift off method) of our samples. At first, the photosensitive resist is spin coated on the top of substrate for making patterns by photolithography (Fig. 3.1 (b) and (c)). Materials used in our devices such as ferromagnet/metal/oxide trilayer, Ti/Au electrode, or Al_2O_3 insulator layer were deposited by e-beam evaporation or sputtering (Fig. 3.1 (d)). Finally, lift-off and cleaning process were done (Fig. 3.1 (d)) to remove the resist. The detail of each step will be explained below.

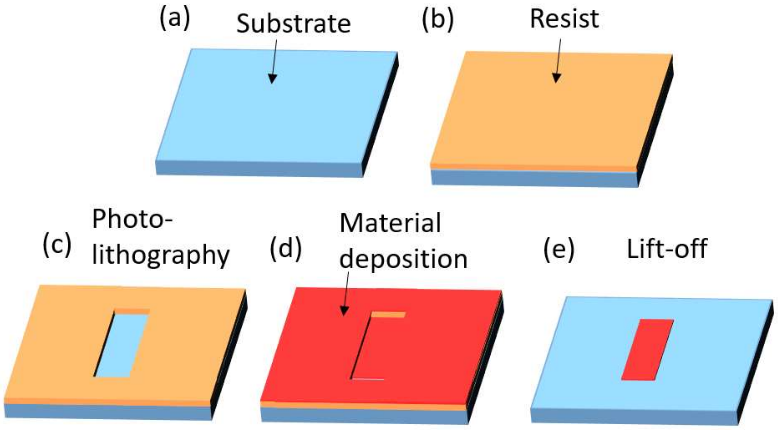

Figure 3-1 Fabrication steps consist of (a) substrate preparation, (b) putting resist, (c) photolithography, (d) material deposition, (e) lift-off.

3.1.2 Photolithography

Photolithography is a powerful technique used in fabrication of micrometer scale. It uses a light to exposure the pattern on a photoresist. In this thesis, we used a mask-less UV photolithography D-Light-DL100RS system. The laser position is controlled by mirrors in this system so a photomask is not necessary for making pattern.

Fabrication process starting from the substrate preparation to patterning process is described as below:

1. Si substrate with 300nm SiO_2 layer on top is cut in a dimension of 10 to 20 mm by using a scriber.
2. Cleaning of substrate: the substrate is plunged into acetone and put in an ultrasonic bath for 15 min then dried with a nitrogen N_2 gun. Then, the substrate is plunged into IPA (isopropyl alcohol) and put in ultrasonic bath again for 1 min to remove the acetone on substrate and dried with N_2 gun. At the end, an ultraviolet cleaning is done for 5 min to remove all the organic on the surface.
3. HDMS (1,1,1,3,3,3 - Hexamethyldisilazane, $C_6H_{10}NSi_2$), which is generally used to make the resist stick to sample more easily, is spin-coated on the top of substrate at 500 rpm for 5 seconds and then 5000rpm for 40 seconds
4. The sample is baked in an oven at 80° C for 5 minutes.
5. The sample is cooled down at room temperature for 5 min then AZ1500 resist is spin-coated at 500rpm for 5 seconds then 5000rpm for 40 seconds.
6. The sample is baked in an oven at $80^{\circ}C$ for 10 minutes
7. The sample is exposed using photolithography at 95 mJ/mm^2.
8. Patterns are developed for 45 seconds and rinsed in flowing water for 1 minute.
9. The pattern is checked by an optical microscope.

3.1.3 Electron beam (E-beam) evaporation

Electron beam evaporation is a technique that using an electron beam to heat the target source materials and thermally evaporate the atoms of materials for deposition on substrate. Compare to resistance evaporation technique, E-beam evaporation has several advantages. For example, the direct transfer of high energy from electron beam to the target material enables us to evaporate materials with high melting points like metals. In addition, because the E-beam system can only heat a smaller region of the target material instead of heat the entire crucible, the possible contamination effect from the crucible is lower than resistance evaporation. A schematic of E-beam evaporation process is shown in Fig. 3-2. Firstly, a current with high voltage ~4 k*V* is applied into a tungsten filament of the electron gun and then a thermal emission of electrons is generated. By applying an external magnetic field, the trajectory of electrons can be controlled by Lorentz force. The electron beam hits the target and heats it to thermal evaporation. Then, these evaporated atoms of target are deposited on the substrate. In E-beam evaporation a high vacuum degree is required to prevent the scattering between the gas atoms and evaporated target atoms; the base pressure in the vacuum chamber for deposition is 3×10^{-5} Pa in this study. Table 3-1 shows the deposition rate and the thickness of each material used in this study.

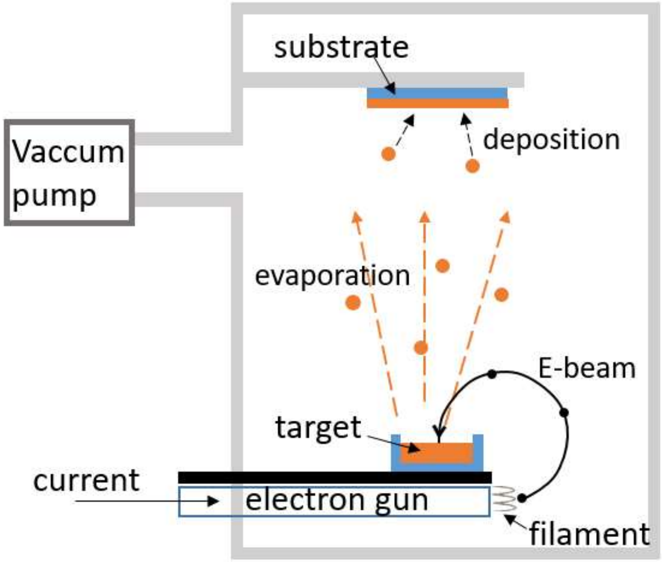

Figure 3-2. Schematic illustration of E-beam evaporation

Materials	Deposition rate (Å/s)	Thickness (nm)
$Ni_{80}Fe_{20}$ (Py)	0.4-0.5	5
Cu	2.0	20, 30
Ag	2.0	20, 30
Al	2.0	20
Au	2.0	25, 35, 150
Ti	0.3-0.4	5
Bi_2O_3	0.2	30
SiO_2	0.2	30
HfO_2	0.2	30
Al_2O_3	0.2	30
SnO_2	0.2	30

Table 3-1. Deposition rate and thickness of E-beam evaporation of each material used in this thesis.

3.1.4 Sputtering

When high energy particles collide with target source material, atoms are ejected from a target material and then deposited on the substrate. This process is known as sputtering. The required kinetic energy of incoming particles is larger than 1 eV, which is much higher than conventional thermal energy in order of 0.1 eV. Sputtering can be done by using DC voltage (DC sputtering) or using AC voltage (RF sputtering). A schematic image of sputtering process is shown in Fig. 3-3. At first, substrate and target material are placed in a vacuum chamber containing an inert gas, usually argon. A high voltage about 3-5 kV is applied across the target source material and substrate, and then the free electrons start to flow in the plasma environment. Ar gas atoms are ionized by the collision with electrons and attracted to the negatively charged target; due to the high kinetic energy of Ar ions, atoms are ejected from the target and are deposited on the surface of the substrate. In this study, an 180 nm Al_2O_3 layer used for insulating is deposited by rf sputtering, and a 200 nm ITO (Indium Tin oxide) layer is deposited by dc sputtering.

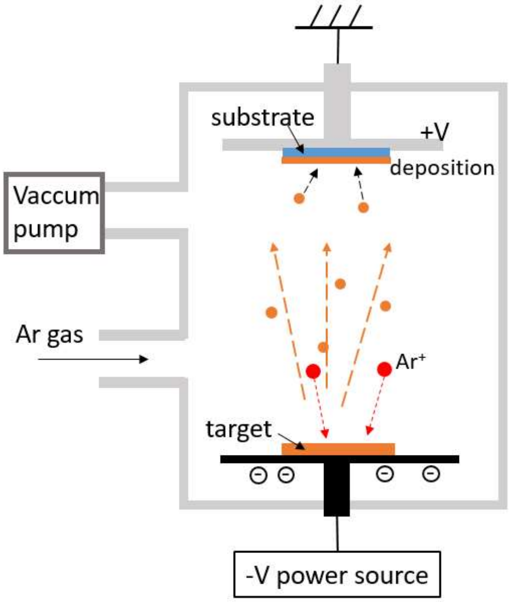

Figure 3-3. Schematic illustration of sputtering process.

3.1.5 Fabrication of spin pumping and spin-torque FMR device

In this study, we use spin pumping and ST-FMR method to detect spin conversion. The device fabrication steps are as follow:

1. Bottom electrode: At first, a bottom electrode of Ti(5nm)/Au(25 or 35nm) is deposited by E-beam evaporation. The schematic of bottom electrode is shown in Fig. 3-4(a). The thickness of bottom electrode is better to be larger than the thickness of conductive layer of measured sample wire to prevent the natural oxidation happen at the contact part.
2. Sample wire: Py(5nm)/metal (20 or 30 nm)/oxide(30nm) tri-layer is deposited between the bottom electrode. The dimension of the sample wire is 14 μm x 200 μm. Because Py and metal layer is easily oxidized in atmosphere, it is better to put the photoresist on the sample just after the lift-off process to protect the sample. In addition,

because the conduction between sample and bottom electrode is formed during the deposition in high vacuum so there is no natural oxidation of Py and metal layer at the contact part and therefore a better contact can be obtained by putting the bottom electrode before depositing sample wire.

3. Top electrode: After the sample wire, a top electrode of Ti(5 nm)/Au(150 nm) is deposited as shown in Fig. 3-4(b). Top electrode will contact with a probe for electrical detection so a thicker Au layer (150-200 nm) is preferred.
4. Insulating layer: An 180nm insulating Al_2O_3 layer is deposited to protect the sample. Also in spin pumping measurement case, an insulating layer can prevent the rf current in the waveguide leaking into the sample wire or electrode.
5. Coplanar waveguide (CPW): At last, a CPW of Ti(5nm)/Au(150nm) is deposited. Because in the experiment the rf field is generated by injecting current into CPW, the position of CPW with respected to the sample wire should be the same when doing photolithography to make sure there is no difference of the magnitude of rf field in every samples and devices.

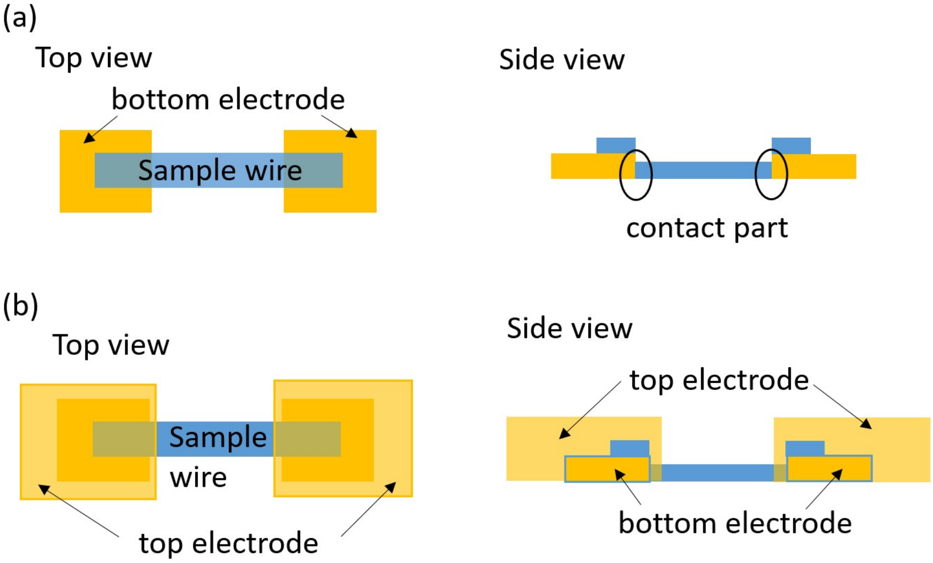

Figure 3-4. Schematic illustration of (a) bottom electrode and (b) top electrode.

3.2 Experiment setup

3.2.1 Spin pumping measurement

Fig. 3-5 shows the schematic illustration of experiment setup in spin pumping measurement. A sample wire of Py/metal/oxdie tri-layer, is placed beside a signal line of coplanar waveguide (CPW) made by Ti/Au. The wires are fabricated by optical lithography and lift-off method. A rf current is injected into the signal line to generate a rf magnetic field h_{rf}. By sweeping the external magnetic field H, FMR can be excited at the resonance field in Py layer. As introduced in chapter 2, the precession motion of the magnetization in Py layer pumped a spin current into the metal layer and reach the metal/oxide interface. A charge current generated by spin-to-charge conversion through IEE or ISHE is then detected as a voltage signal. In this study, the power of rf current of spin pumping measurement is 16 to 24 dBm, and the frequency is from 5 GHz to 10 GHz. The measurement is performed from 10 K to 300 K. For low temperature measurement, we use a probe system of NAGASE company. The sample is put in a vacuum chamber with pressure about 10^{-4} Pa and be cooled down by helium compressors. The measurement at room temperature is done at either atmosphere or pressure in 10^{-4} Pa. We found that the vacuum degree has no notable effect to the spin pumping measurement.

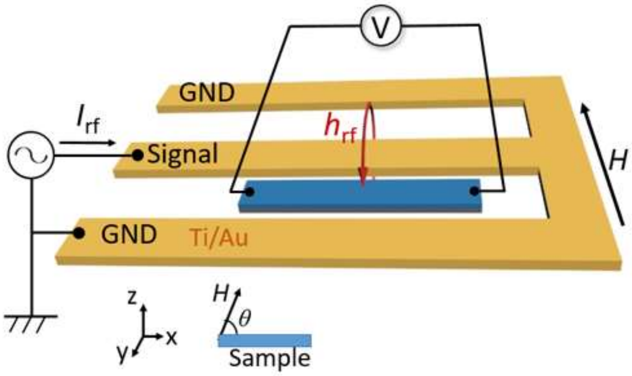

Figure 3-5. The experiment setup of spin pumping measurement.

3.2.2 Spin torque ferromagnetic resonance (ST-FMR) measurement

Fig. 3-6 shows the schematic image of a device structure consisting of a multi-layer wire and Ti/Au CPW. The CPW is deposited on both ends of the wire so that the wire element act as a part of the waveguide. A voltage meter and signal generation are connected to the CPW through a bias tee as shown in Fig. 3-6. When rf current I_{rf} and direct current I_{dc} is applied to the sample, FMR in Py layer is excited by rf magnetic field due to I_{rf}. The I_{dc} generates a spin accumulation at the metal/oxide interface though DEE; a diffusive spin current is driven by spin accumulation towards the Py layer and modulate the damping torque by spin torque as introduced in chapter 2. The power of rf current is 20 dBm and the frequency is 8 GHz is ST-FMR measurement. The external magnetic field is applied at 45 and 225 degrees with respect to the easy axis of the same wire. The ST-FMR measurement is performed at room temperature.

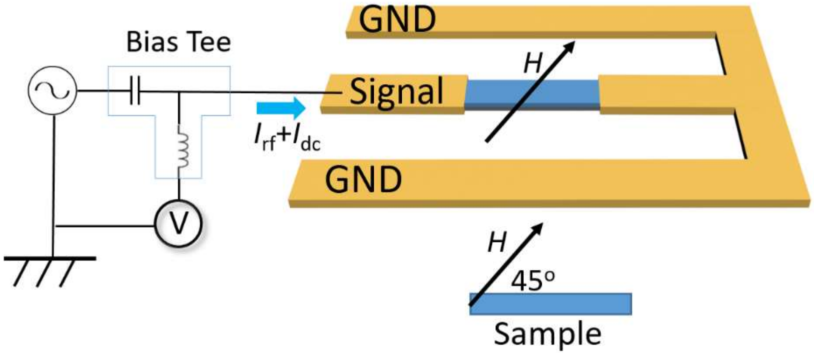

Figure 3-6. The experiment setup of ST-FMR measurement.

3.3 First-principle calculation method

In this thesis, a first-principle calculation with collaboration of the group of Prof. Ishii in Kanazawa University is performed to calculate the Rashba parameter at various metal/Bi_2O_3 interface. A density functional calculation within the general gradient approximation [3-1] is performed by using OpenMX code [3-2], with the fully relativistic total angular momentum dependent pseudopotentials taking spin-orbit interaction (SOI) into account [3-3]. We adopted norm-conserving pseudopotentials with an energy cutoff of 300 Ry for charge density including the 5d, 6s and 6p-states as valence states for Bi; 2*s* and 2*p* for O; 3s, 3p, 3d and 4s for Cu; 4p, 4d and 5s for Ag; 5p, 5d and 6s for Au. We used 16×12×1 regular *k*-point mesh. The numerical pseudo atomic orbitals are used as follows: the numbers of the *s*-, *p*- and *d*-character orbitals are three, three and two, respectively; The cutoff radii of Bi, O, Cu, Ag and Au are 8.0, 5.0, 6.0, 7.0 and 7.0, respectively, in units of Bohr. The dipole-dipole interaction between slab models can be eliminated by the effective screening medium (ESM) method [3-4].

Reference of chapter 3

[3-1] J. Perdew, K. Burke and M. Ernzerhof, *Physical Review Letters* **77**, no. 18, pp. 3865-3868 (1996).

[3-2] Ozaki, T. *et al*., User's manual of OpenMX Ver. 3.8, http://www.openmx-square.org/openmx_man3.8/openmx3.8.pdf (2016).

[3-3] G. Theurich and N. Hill, *Physical Review B* **64**, no. 7 (2001).

[3-4] M. Otani and O. Sugino, *Physical Review B* **73**, no. 11 (2006).

Chapter 4

Modulation of Rashba spin-splitting by changing electron distribution at various non-magnetic metal/Bi_2O_3 interfaces

The conversion efficiency of both direct Edelstein effect (DEE) and inverse Edelstein effect (IEE) is proportional to Rashba parameter α_{R}. Therefore, how to design the interfaces with large Rashba spin-splitting is important for spin-charge interconversion in spintronic devices. As introduced in Chapter 2, α_{R} can be described by $\alpha_{\mathrm{R}} = (\frac{2}{c^2}) \int (\partial V/\,\partial z)\, |\psi|^2\, dz$, where c, $\partial V/\,\partial z$ and $|\psi|^2$ are respectively the speed of light, potential gradient and electron density distribution. Zero point of z locates at the center of atoms at interface. Because this integral is strongly affected by asymmetric and localized feature of $|\psi|^2$ [4-1, 4-2], even a small modulation of $|\psi|^2$ can have notable effect on α_{R}. This suggests that Rashba spin-splitting can be controlled effectively by tuning the interfacial condition, i.e. changing metal materials at metal/Bi_2O_3 interfaces. To understand how to design the materials for large Rashba spin-splitting at metal/oxide interface, in this chapter, the S-C conversion and Rashba parameter in various metal (Cu, Ag, Al, Ag)/Bi_2O_3 interfaces is investigated. We observed large modulation and sign change in conversion coefficient which corresponds to the variation of spin-splitting. The experimental results together with first-principles calculations indicate that such large variation is caused by materials dependent electron distribution near the interface. The results suggest that control of interfacial electron distribution by tuning the difference in work function across the interface may be an effective way to tune the magnitude and sign of spin-to-charge conversion and Rashba parameter at interface.

4.1 Detection of spin-to-charge current conversion at metal (Ag, Cu, Au, Al) /Bi_2O_3 interfaces

Fig. 4-1(a) is a schematic illustration of the measurement setup. We prepared four different NM material samples. Each $Ni_{80}Fe_{20}$ (Py: 5 nm)/NM (Ag, Cu, Au, or Al 20 nm)/ Bi_2O_3 (30 nm) tri-layer wire is placed beside a signal line of coplanar waveguide (CPW). The measured samples are fabricated by using photo-lithography and e-beam evaporation (see chapter 3). The length and width of the wire are 200 μm and 14 μm, respectively. Fig. 4-1(b) is the schematic of spin-to-charge conversion at the NM/Bi_2O_3 interface. Ferromagnetic resonance (FMR) in Py layer is excited by rf current generated magnetic field h_{rf} in the CPW. Spin current caused by FMR is injected into NM/Bi_2O_3 layer. This spin current gives rise to an electric dc voltage V through the inverse spin Hall effect (ISHE) and/or inverse Edelstein effect (IEE). The power of rf current is 20 dBm and the frequency is from 6 to 9.5 GHz. All measurements were performed at room temperature. Clear signals due to spin-to-charge (S-C) conversion are detected for all sample as shown in Fig. 4-2.

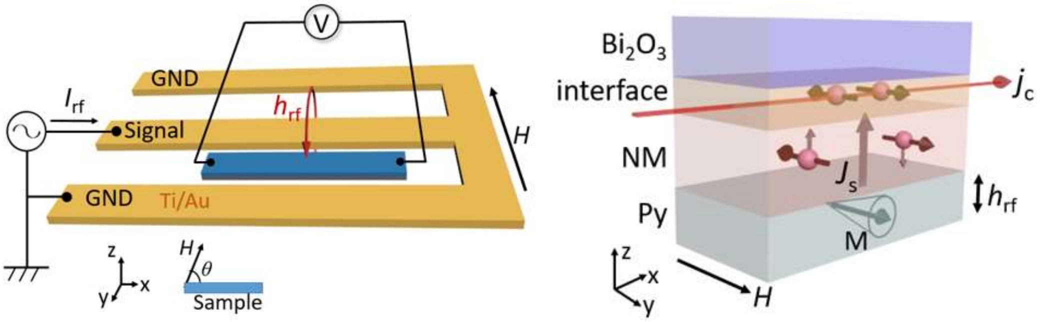

Figure 4-1 (a) Experimental setup for the spin pumping measurement. (b) Schematic of spin-to-charge conversion at the NM/Bi_2O_3 interface.

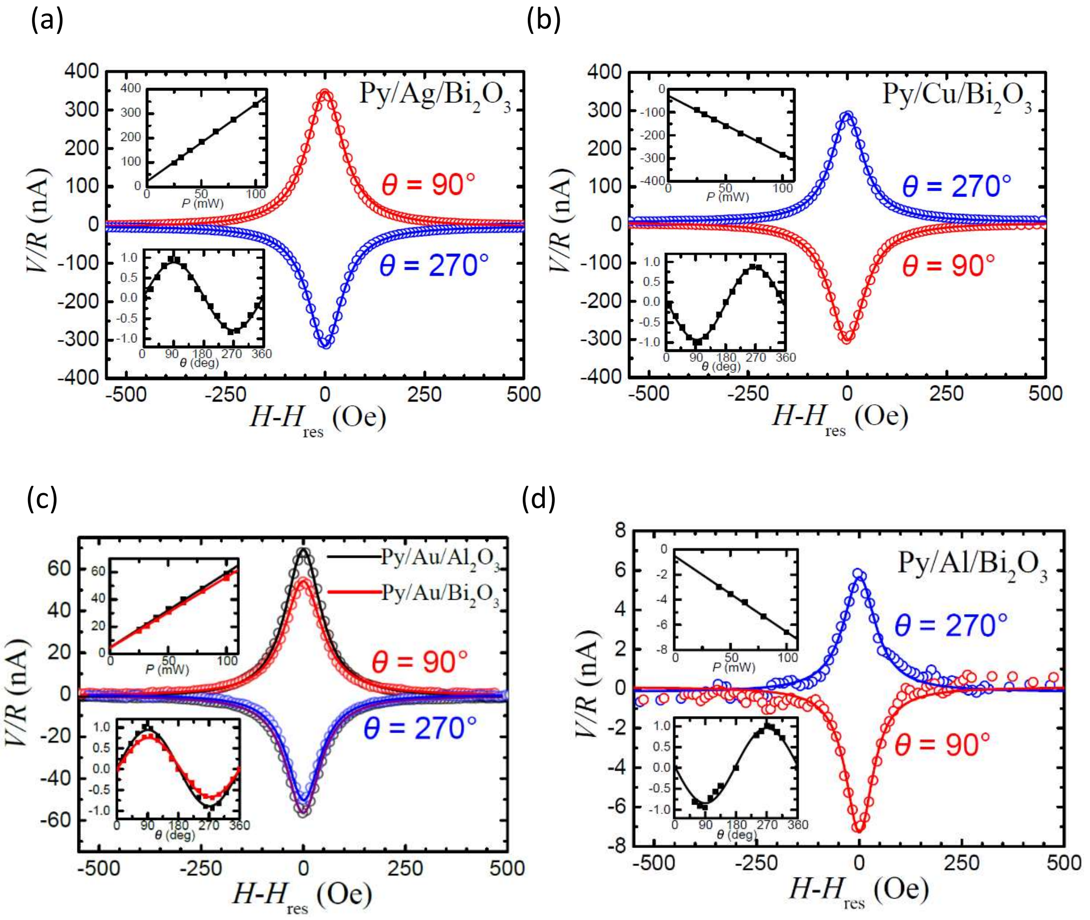

Figure 4-2 Detected *V/R* spectrum of (a) $Py/Ag/Bi_2O_3$; (b) $Py/Cu/Bi_2O_3$; (c) $Py/Au/Bi_2O_3$ and $Py/Au/Al_2O_3$; (d) $Py/Al/Bi_2O_3$. The rf power-dependence of 5 samples is shown in the upper insets, and the angle-dependence of the normalized signal V/R is shown in the lower insets**.**

At the vertical axis, we show the output current values estimated from *V* because the sample resistance *R* is different in each sample. The angle *θ* is the angle between sample wire and external magnetic field *H*. From this measurement, a strong NM materials dependence in amplitude and sign of detected signals is observed. The signal amplitude is almost the same between $Py/Cu/Bi_2O_3$ and $Py/Ag/Bi_2O_3$, but surprisingly their signs are opposite each other. While the amplitude of $Py/Au(Al)/Bi_2O_3$ is one order or two orders of magnitude smaller than Cu/Bi_2O_3. It has been reported that there is almost no S-C conversion signal of Py/Cu and Py/Ag bilayers detected by spin pumping method so the

SHE contribution of Cu and Ag is neglected small [4-3, 4-4]. The possibility of Bi impurity induced extrinsic spin Hall effect in NM can be excluded because the SH angles induced by Bi in Cu and Ag are both negative [4-5]. Therefore, the influence of Bi impurities cannot explain the sign change of S-C conversion between Ag/Bi_2O_3 and Cu/Bi_2O_3. In addition, there is no notable difference between resistivities of Cu/Al_2O_3 and Cu/Bi_2O_3 bilayers, indicating that the contribution of Bi impurities should be small, and the S-C conversions in Py/(Cu, Ag)/Bi_2O_3 are dominated by IEE at their (Cu, Ag)/Bi_2O_3 interfaces.

While the contribution of ISHE in Au may be notable since SHA of Au is one order of magnitude lager than Cu and Ag [4-6, 4-7]. To estimate the contribution of ISHE in Au, we prepared the reference sample of Py/Au/Al_2O_3 trilayer. Figure 4-2(c) shows the output spectrum of Py/Au/Al_2O_3 and Py/Au/Bi_2O_3. From the signal amplitude in Py/Au/Al_2O_3, we estimated spin Hall angle θ_{SH} in Au layer is +0.40±0.07%; the details calculation will be shown in section 4-3. This value is in good agreement with reported values [4-7, 4-8]. By comparing the signal amplitudes of Py/Au/Al_2O_3 and Py/Au/Bi_2O_3, we found that the sign of S-C conversion at Au/Bi_2O_3 interface should be opposite to SHA in Au.

The rf power-dependence of 5 samples is shown in the upper insets to Fig. 4-2(a)-(d). The detected signals increase linearly with the rf power, being consistent with the prediction of spin pumping model [4-9]; It also indicates that the spin pumping experiment are in the linear regime of FMR. Furthermore, the angular dependence of magnetic field of the normalized signal is shown in the lower insets to Fig. 4-2(a)-(d). All of them show the sinusoidal shape which can be explained by typical Rashba model as introduced in chapter 2. This confirms that the observed S-C conversion signals arise from FMR spin pumping.

4.2 Estimation of spin current

The injected spin current can be derived by analyzing the *V/R* spectrum of spin pumping measurement. The enhancement of the magnetic damping constant gives the spin injection efficiency known as spin mixing conductance [4-8],

$$g_{\mathrm{eff}}{}^{\uparrow\downarrow}=\frac{\mu_0 M_{\mathrm{s}} t_{\mathrm{F}}}{g\mu_{\mathrm{B}}}\left(\delta_{\mathrm{F/N/O}}-\delta_{\mathrm{F/N}}\right) \tag{4.1}$$

where $t_{\mathrm{F}},$ $\delta_{\mathrm{F/N/O}}$, and $\delta_{\mathrm{F/N}}$ are the saturation magnetization, the thickness of Py, the damping constant for Py/NM/Bi$_2$O$_3$, and the damping constant for Py/Cu, respectively. The injected spin current density at Py/NM interface J_{s}^{0} is given by [4-13]

$$J_{\mathrm{s}}^{0} = \frac{2e}{\hbar} \times \frac{\hbar g_{\mathrm{eff}}^{\uparrow\downarrow} \gamma^2 (\mu_0 h_{\mathrm{rf}})^2 \left[\mu_0 M_{\mathrm{s}} \gamma_{\mathrm{e}} + \sqrt{(\mu_0 M_{\mathrm{s}})^2 \gamma_{\mathrm{e}}^2 + 4\omega^2}\right]}{8\pi \delta_{\mathrm{F/N/O}}^2 \left[(\mu_0 M_{\mathrm{s}})^2 \gamma_{\mathrm{e}}^2 + 4\omega^2\right]} \quad (4.2)$$

where γ, h_{rf} and ω are the gyromagnetic ratio, applied rf field and the angular frequency, respectively.

Fig. 4-3(a) shows rf current frequency as a function of the magnetic resonant filed. By fitting with Kittel formula, $(\omega/\gamma)^2 = \mu_0 H_{\mathrm{dc}}(\mu_0 H_{\mathrm{dc}} + \mu_0 M_{\mathrm{s}})$, the saturation magnetization $\mu_0 M_{\mathrm{s}}$ of the Py can be derived. Fig. 4-3(b) shows the half width at half maximum (HWHM) as a function of rf current frequency. From the slope, we can derived the effective magnetic damping constant δ_{eff} for Py by using the relation, $\Delta H = \delta_{\mathrm{eff}} \omega/\gamma + \Delta H_0$, where ΔH_0 is the offset of the HWHM, respectively [4-14]. For Py/Cu bilayer, almost all of the injected spin current is reflected back to the Py layer without spin relaxation in Cu layer [4-15] because the spin diffusion length in Cu of 400 nm at 290K [4-16] is much larger than NM layer thickness of 20 nm. Therefore, Py/Cu bilayer sample shows the smallest slope corresponding to the smallest damping of FMR. In contrast, all of the other samples show the enhancement of damping in FMR. It implies that for Py/Ag/Bi$_2$O$_3$ and Py/Cu/Bi$_2$O$_3$,

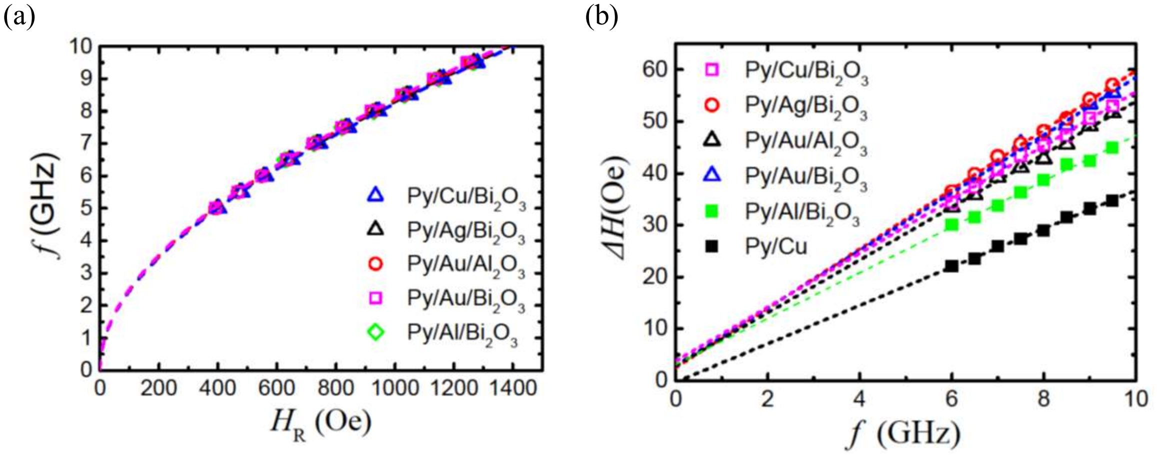

Figure 4-3. (a) Rf current frequency as a function of the magnetic resonant filed. (b) Half width at half maximum (HWHM) as a function of rf current frequency.

spin current is injected into the interface. On the other hand, for Py/Au/Bi_2O_3, both SOC in Au bulk and at Au/Bi_2O_3 interface contribute to the enhanced the damping of FMR.h_{rf} is determined by precession cone angle measurement developed by M. V. Costache *et al.* [4-17]. We measured the cone angle θ_{c} of the of Py(5 nm)/Al_2O_3(30 nm) bilayer sample in FMR with 20 dBm rf current at 9 GHz. Fig. 4-4(a) shows the experiment setup which has complete the same design as our spin pumping measurement but with a bias current injecting into Py layer for detecting the resistance from V/I curve. The anisotropic magneto-resistance (AMR) of Py layer with parallel magnetic field $H_{/\!/}$ and perpendicular magnetic field $H_{\perp}$ with respect to current direction is shown in Fig. 4-5(a). The resistance difference ΔR between $H_{/\!/}$ and $H_{\perp}$ due to AMR is about 10 Ω. When Py layer is excited to FMR resonance, the resistance change due to AMR of the precession motion as shown in Fig. 4-4(b). The detected voltage spectrum with controlled bias current is shown as Fig. 4-5(b). Fig. 4-5(c) shows the detected voltage as a function of bias current. From linear fitting, the slope of Fig. 4-5(c) gives resistance change in FMR, ΔR_{FMR} = 0.042 Ω. From the relation, $\Delta R_{FMR}/\Delta R = \sin^2\theta_{\mathrm{c}}$ and $\theta_{\mathrm{c}} = h_{\mathrm{rf}}/2\Delta H$ the estimated cone angle of Py/Al_2O_3 is 3.7° and the h_{rf} is 9.4 Oe. As the results, the estimated spin current density J_{s}^{0} of Py/Ag/Bi_2O_3, Py/Au/Al_2O_3, Py/Au/Bi_2O_3, Py/Al/Bi_2O_3, and Py/Cu/Bi_2O_3 is 13.6×10^{7}A/m^2, 7.7×10^{7} A/m^2, 8.9×10^{7} A/m^2, 9.0×10^{7} A/m^2, and 11.4×10^{7} A/m^2, respectively. The injected spin current J_{s}^{0} at Py/NM interface propagates and exponentially decays in the NM layer. The spin current at NM/Bi_2O_3 interface is $J_{\mathrm{s(NM/Bi_2O_3)}} = J_{\mathrm{s}}^{0} \times \exp(-t_{\mathrm{N}}/\lambda_{\mathrm{N}})$, where t_{N} and λ_{N} are the thickness and spin diffusion length of NM, respectively. For NM=Ag, Cu, Al, their λ_{N} is larger than 300 nm on room temperature [4-16, 4-18, 4-19], which is much larger than λ_{N}=20 nm; therefore there is almost no effect of the decay term. For NM=Au, we use λ_{N}=35 nm from a reported value [4-8].

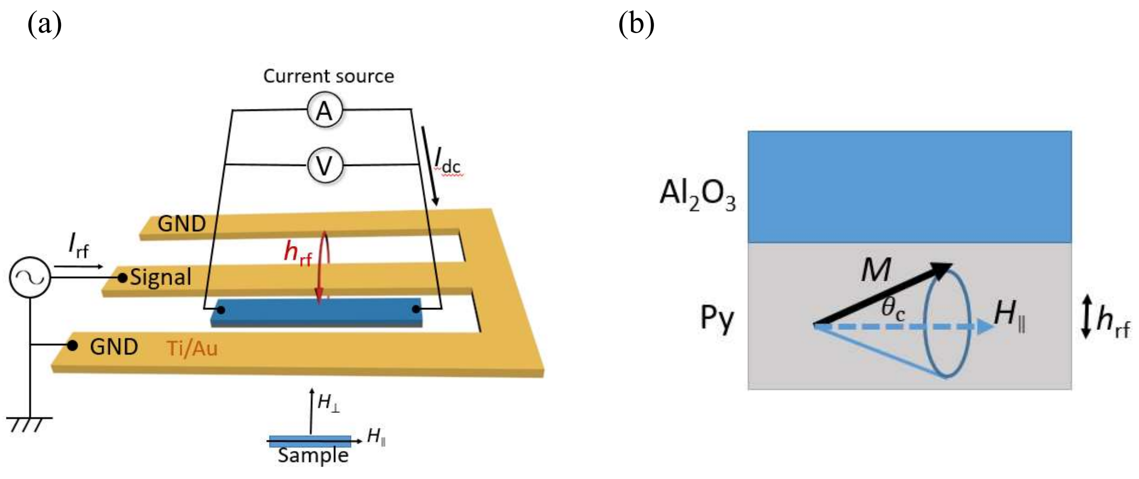

Figure 4-4. (a) Experimental setup for the cone angle measurement. A bias current is injected into Py/Al_2O_3 bilayer sample to measure the *V/I* curve. (b) Schematic of magnetization precession of Py with cone angle θ_c in ferromagnetic resonance (FMR).

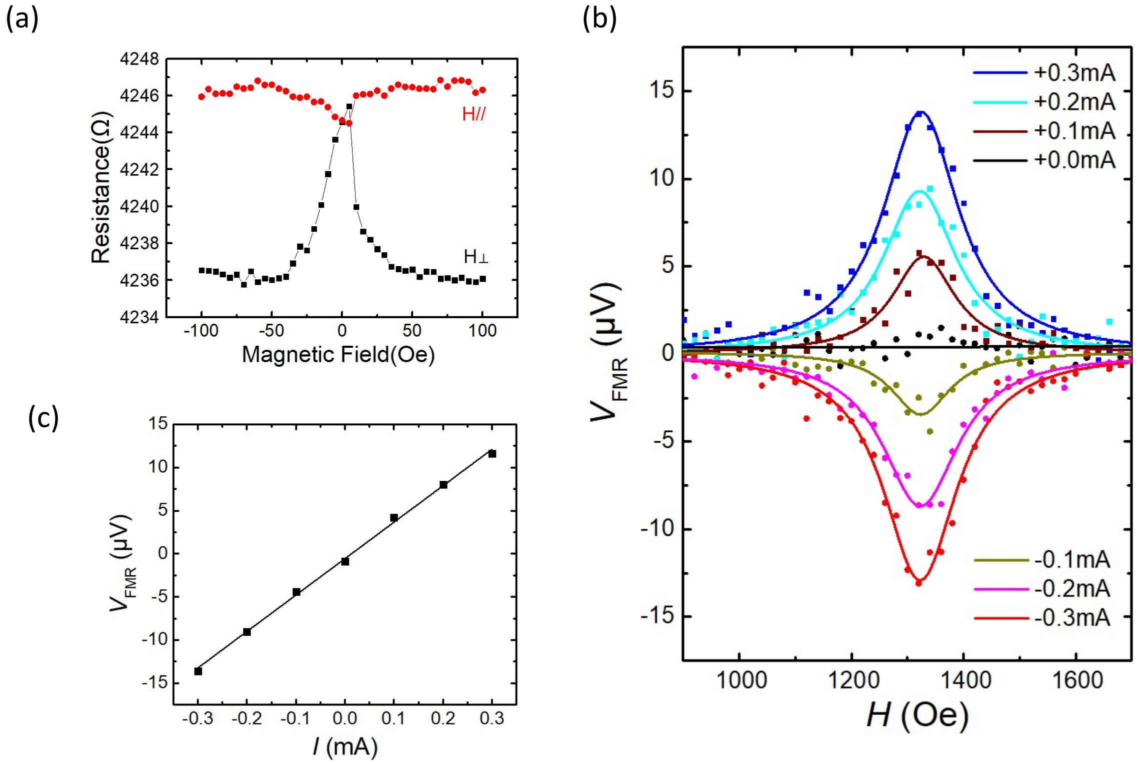

Figure 4-5 (a) Magnetoresistance due to AMR effect of Py(5nm) in parallel magnetic field $H_{//}$ and perpendicular magnetic field $H_\perp$ with respect to current direction. (b) Detected voltage difference V_{FMR} due to precession of FMR with bias current from -0.3mA to +0.3mA (c)Detected FMR voltage as a function of bias current

4.3 Separation of inverse spin Hall effect and inverse Edelstein effect

When measuring the spin-to-charge (S-C) conversion at the Bi_2O_3 interface of Ag, Cu, and Al, the spin Hall effect of these NM materials is negligible small. However, in Au/Bi_2O_3 case spin Hall angle of Au is one order larger than others and makes notable contribution. For analyzing Py/Au/Bi_2O_3 sample, the contribution of SHE of Au and IEE in Au/Bi_2O_3 interface need to be separated. Firstly, we measure the spin Hall angle of Au by measuring S-C conversion in Py/Au/Al_2O_3 sample. By solving the spin diffusion equation with the boundary condition that spin current is zero at Au/Al_2O_3 interface, the spin current flowing in the Au layer is

$$J_{\mathrm{s}}(y) = \frac{\sinh[(t_{\mathrm{N}} - y)/\lambda_{\mathrm{N}}]}{\sinh(t_{\mathrm{N}}/\lambda_{\mathrm{N}})} J_{\mathrm{s}}^{0} \qquad (4.3)$$

where t_{N}, and λ_{N} are the thickness of NM layer, and the spin-diffusion length of NM layer, respectively. J_{s}^{0} is the spin current injected at Py/Au interface which is shown in eq. (3). Here, we use λ_{N} = 35 nm from a reported value [4-8]. The average spin current density is $\langle J_{\mathrm{s}} \rangle = \frac{1}{t_{\mathrm{N}}} \int_{0}^{t_{\mathrm{N}}} J_{\mathrm{s}}(y)$ and the average charge current density in three dimension is $\langle J_{\mathrm{c}} \rangle = \theta_{\mathrm{SH}} \langle J_{\mathrm{s}} \rangle$. Therefore, the spin Hall angle θ_{SH} can be calculated by

$$\langle J_{\mathrm{c}} \rangle = \theta_{\mathrm{SH}} \left(\frac{2e}{\hbar} \right) \frac{\lambda_{\mathrm{N}}}{t_{\mathrm{N}}} \tanh\left(\frac{t_{\mathrm{N}}}{2\lambda_{\mathrm{N}}} \right) J_{\mathrm{s}}^{0} \qquad (4.4)$$

As the result, θ_{SH} of Au is +0.40±0.07%, which is in a good agreement with reported value measured by spin-pumping method . The next step is considering the interface effect of Au/Bi_2O_3. Because some spin current is injected into the Au/Bi_2O_3 interface, the backflow of spin current is reduced and the injected spin current increased at Py/Au interface, i.e. $J_{\mathrm{s}(\mathrm{Au/Bi_2O_3})} = J_{\mathrm{s}(\mathrm{Au/Al_2O_3})} + \Delta J_{\mathrm{s}}$ and $\Delta J_{\mathrm{s}} > 0$. Since the backflow of spin current decays from y = t_{N} to y = 0, that is ΔJ_{s}(y) = $\Delta J_{s}^{0} e^{y/\lambda_{\mathrm{N}}}$ and ΔJ_{s}^{0} = ${J_{\mathrm{s}}}^{0}{}_{(\mathrm{Au/Bi_2O_3})} - {J_{\mathrm{s}}}^{0}{}_{(\mathrm{Au/Al_2O_3})}$. The spin current in Au/Bi_2O_3 can be expressed as

$$J_{\mathrm{s}}(y) = \frac{\sinh[(t_{\mathrm{N}} - y)/\lambda_{\mathrm{N}}]}{\sinh(t_{\mathrm{N}}/\lambda_{\mathrm{N}})} J_{s\,(\mathrm{Au/Al_2O_3})}^{0} + \Delta J_{s}^{0} e^{y/\lambda_{\mathrm{N}}} \qquad (4.5)$$

Again, the average spin current density is $\langle J_s \rangle = \frac{1}{t_N}\int_0^{t_N} J_s(y)$. We assumed that the θ_{SH} of the Au bulk in Au/Bi_2O_3 and Au/Al_2O_3 are approximately equal since the typical thickness of interface layer is only 0.4 nm. By separating the contribution of ISHE and IEE, the 3D charge current density $\langle J_c \rangle$ can be expressed as

$$\langle J_c \rangle = \langle J_s \rangle \theta_{SH} + J_{s(\text{interface})} \times \lambda_{\text{IEE}} t_N \quad (4.6)$$

and then the λ_{IEE} of Au/Bi_2O_3 interface is derived.

4.4 Conversion coefficient and Rashba parameter at various metal/Bi_2O_3 interfaces

The S-C conversion coefficient of IEE is defined as $\lambda_{\text{IEE}} \equiv j_{c(2D)}/J_s$, where $j_{c(2D)}$ is the charge current density at 2D interface and J_s is the spin current density. Here, the units of j_c and J_s are A/m and A/m^2, respectively. Therefore, λ_{IEE} has a unit of length. For NM=Ag, Cu, Al, because the S-C conversion from ISHE can be neglected, $j_{c(2D)}$ is simply calculated by $j_c = V/wR$ where V, w, and R are detected voltage, the width of the sample wire, and total resistance of the wire, respectively. For NM=Au case, contribution of SHE and IEE need to be separated for estimating λ_{IEE}. The calculated λ_{IEE} of various metal/ Bi_2O_3 interfaces is shown in Table 4-1; λ_{IEE} at Cu, Ag /Bi_2O_3 interfaces is comparable with the reported value λ_{IEE} = 0.3 nm for Ag/Bi interface measured by spin pumping method [4-10], and is one-order larger than λ_{IEE} = 0.009 nm for Cu/Bi measured by lateral spin valves method [4-11]. The λ_{IEE} can be expressed by using the Rashba parameter α_R and momentum relaxation time τ_p^{int} at the interface [4-12], $\lambda_{\text{IEE}} = \alpha_R \tau_p^{\text{int}}/\hbar$. It has been reported that τ_p^{int} is governed by the momentum relaxation time τ_p^{NM} in the NM layer in contact with Rashba interface [4-4]. By using an approximation $\tau_p^{\text{NM}} \sim \tau_p^{\text{int}}$ with a τ_p^{NM} derived from the resistivity of NM layer, effective Rashba parameter $\alpha_R{}^{\text{eff}}$ was calculated. Table 1 shows the strong NM dependence of λ_{IEE} and $\alpha_R{}^{\text{eff}}$ at NM/Bi_2O_3 interfaces measured at 5 devices of the same sample. We found that Cu/Bi_2O_3 and Ag/Bi_2O_3 have larger $|\alpha_R{}^{\text{eff}}|$ and sign of $\alpha_R{}^{\text{eff}}$ at Ag/Bi_2O_3 is positive while others are negative. The $|\alpha_R|$ calculated by first-principle calculation (see section 4.7)is also shown in Table 1.

Table 1 | Conversion coefficient λ_{IEE}, Rashba parameter $\boldsymbol{\alpha}_{\mathbf{R}}{}^{\mathbf{eff}}$, Damping constant $\boldsymbol{\delta}_{\mathbf{eff}}$, and spin mixing conductance $\boldsymbol{g}_{\mathbf{eff}}{}^{\uparrow\downarrow}$.

Interface	λ_{IEE}(nm)	$\boldsymbol{\alpha}_{\mathbf{R}}{}^{\mathbf{eff}}$(eV·Å)	$\lvert\boldsymbol{\alpha}_{\mathbf{R}}\rvert$(eV·Å) (calculation)	$\boldsymbol{\delta}_{\mathbf{eff}}$	$\boldsymbol{g}_{\mathbf{eff}}{}^{\uparrow\downarrow}$ (10^{18} m^{-2})
Ag/Bi_2O_3	+0.15 ±0.03	+0.16 ±0.03	0.50	0.0168	10.78
Cu/Bi_2O_3	-0.17 ±0.03	-0.25 ±0.04	0.91	0.0154	8.27
Au/Bi_2O_3	-0.09 ±0.03	-0.10 ±0.04	0.29	0.0142	3.77
Al/Bi_2O_3	-0.01 ±0.002	-0.055 ±0.011	-------	0.0133	4.49

Table 4-1. Conversion coefficient $\lambda_{\mathbf{IEE}}$, Rashba parameter $\boldsymbol{\alpha}_{\mathbf{R}}{}^{\mathbf{eff}}$, damping constant $\boldsymbol{\delta}_{\mathbf{eff}}$, and spin mixing conductance $\boldsymbol{g}_{\mathbf{eff}}{}^{\uparrow\downarrow}$ in various NM/Bi_2O_3 interfaces.

To check the system error of our spin pumping measurement and analysis method, we investigated λ_{IEE} and $\alpha_{\mathrm{R}}{}^{eff}$ at different rf current frequency in spin pumping method as shown in Fig. 4-6. Because the spin current generated by spin pumping in average is a dc spin current, the S-C conversion and Rashba parameter at NM/Bi_2O_3 should not depend on the frequency of rf current. As expected, by measuring one Py/Cu/Bi_2O_3 sample at 6,7,8, and 9 GHz, λ_{IEE} is 0.19±0.005nm and $\alpha_{\mathrm{R}}{}^{eff}$ is 0.27±0.007 (eV·Å) as shown in Fig. 4-6. This 2.6% system error is much smaller than the standard deviation of different devices, indicates that our measurement technique is convincible. Note that the value here is measured by only one device of the sample at different frequency while the values in Table 4-1 are measured by 5 devices of the same sample at 9 GHz.

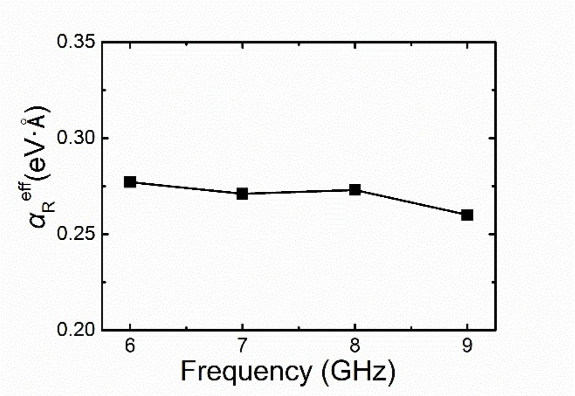

Figure 4-6. Frequency dependence of Rashba parameter

4.5 Discussion of metal materials dependence

Here we discuss the materials dependence of two important origins of Rashba effect, atomic SOC and broken inversion symmetry. Firstly, we compare the influence of SOC of different NM materials. Even though Au has one order larger SOC than Ag and Cu, its Bi_2O_3 interface has smaller $|\alpha_R{}^{eff}|$. This result suggests that the SOC of NM layer is not essential to Rashba effect at NM/Bi_2O_3 interfaces. This trend is the same with the first-principles calculations and experimental results in ARPES measurement in Ag(111)/Bi and Cu(111)/Bi Rashba interfaces [4-20]. The reason is that the SOC of Bi dominantes the large Rashba spin splitting at NM/Bi_2O_3 interface so the contribution of SOC of NM is too smaller to be detected. As the results, the strong NM dependency is not due to different SOC strength of NM materials. Secondly, we discuss the materials dependence of broken inversion symmetry. Several possible origins of broken inversion symmetry is discussed below, which are film crystallinity, atomic structure, and work function difference at interface.

4.5.1 Film crystallinity

We use X-ray diffraction (XRD) to get the crystallinity information at NM/Bi_2O_3 interface of each Py/NM/Bi_2O_3 samples. The general results of Py/Ag/Bi_2O_3 and Py/Cu/Bi_2O_3 are on the top of figure 4-7(a) and (b). Three main peaks which correspond to Bi_2O_3, Ag(111) or Cu(111), and Ni(111), are observe. The results indicate that in Cu, Ag, and Au layer, mainly there is (111) alignment. In contrast, the peak of Bi_2O_3 is quite broaden so the Bi_2O_3 should be amorphous. In addition, to get the information at metal/Bi_2O_3 interface, we performed the grazing incident X-ray diffraction measurement (GI XRD). By using a small incident angle ~0.4 degree, the X-ray mostly reflected at metal/ Bi_2O_3 interface and therefore give us the information at the interface. The GI XRD results are shown in the Fig. 4-7(a)-(c); there is no peak of Ni(111) observed in GI XRD, indicating that the X-ray doesn't reach the Py layer and it is reflected by NM. We found that the crystallinity at interface is NM(111)/amorphous Bi_2O_3. These results suggest that the NM/Bi_2O_3 (NM = Ag, Cu, and Au) interfaces may have similar crystallinity and therefore the strong NM dependence does not come from the crystal structure.

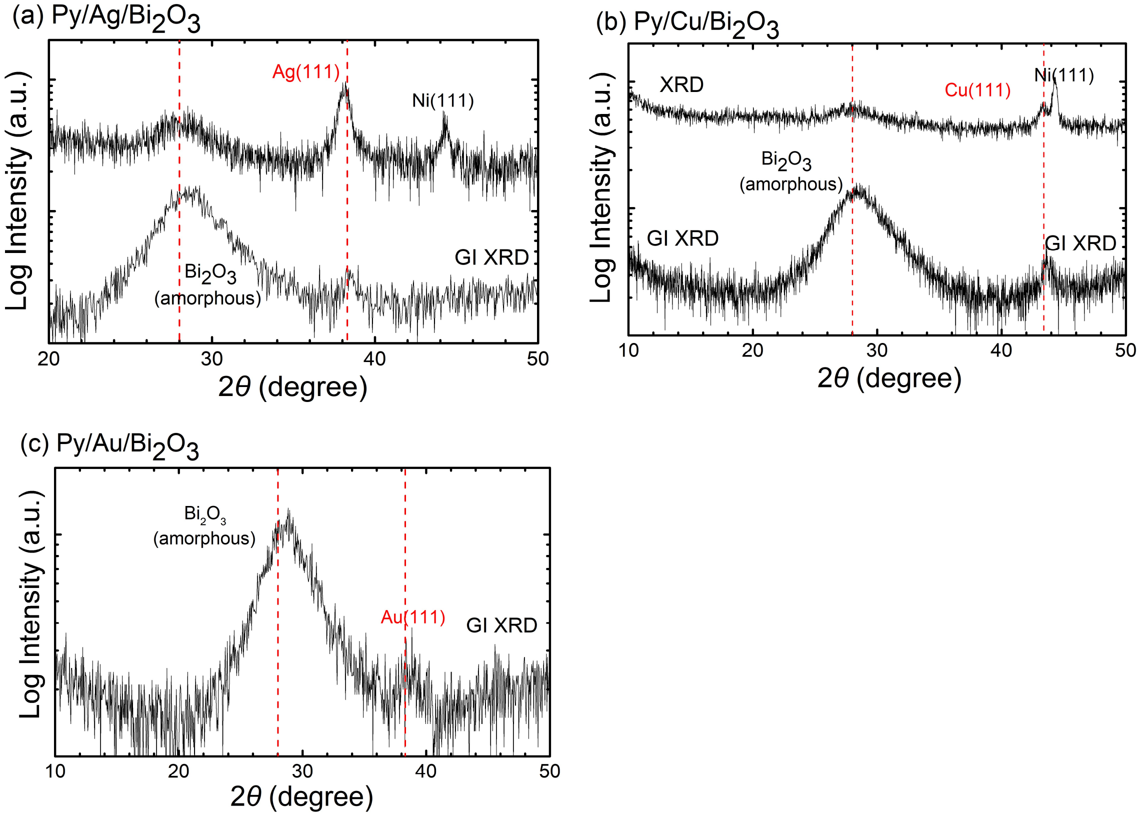

Figure 4-7. XRD and GI XRD spectrum of (a) Py/Ag/Bi_2O_3 (b) Py/Cu/Bi_2O_3 (c) Py/Au/Bi_2O_3

4.5.2 Interface alloying structure

In the metallic Rashba interface such as Ag/Bi, the potential inversion symmetry is occurred by the work function difference and also the interface alloying structure. It has been shown that the contribution of interface alloying structure on α_{R} is much larger than work function difference [4-21]. For example, different alloying structure is considered to be the reason why Ag(111)/Bi has 3 times larger α_{R} than Cu(111)/Bi. In contrast, for NM/Bi_2O_3 interfaces, the value of Rashba parameter at Ag/Bi_2O_3 interface is one order smaller than Ag(111)/Bi , and Cu/Bi_2O_3 is about half of Cu(111)/Bi [4-8]. This reduction might be caused by the lack of interface alloying and in-plane potential gradient, because Bi atoms are much more strongly bonded to oxygen atoms than to the NM. Following this hypothesis, we calculate the Rashba parameter at NM (111)/α-Bi_2O_3 interface without any alloying structure. A strong materials dependence is still observed as shown in first-principle calculation results. Therefore, the interface structure is not the reason of NM dependence. In addition, because the lack of alloying structure at NM/Bi_2O_3 interfaces, the work function difference may become an important essence to induce broken inversion symmetry and the interfacial spin splitting.

4.6 Rashba parameter versus work function difference

From previous discussion of NM dependence, the out-of-plane electric field originating from work function difference may be an important essence for inducing inversion broken symmetry at NM/Bi_2O_3 interfaces. That is to say, α_{R} is related with work function difference between NM and Bi_2O_3, $\Delta\Phi_{\mathrm{NM-Bi2O3}}$. Fig. 4-8 (a) shows absolute value estimated by experiment and calculation in different NM/Bi_2O_3 interfaces as a function of $|\Delta\Phi_{\mathrm{NM-Bi2O3}}|$. Here, the $\Delta\Phi_{\mathrm{NM-Bi2O3}}$ is defined as Φ_{NM}-Φ_{Bi2O3}. We use reported value of work function Φ of Cu (111) [4-22], Ag(111), Au(111), Al(111) [4-23], and α- Bi_2O_3 [4-24] as 4.96, 4.74, 5.31, 4.26, and 4.92 in units of eV, respectively. It seems that $|\alpha_{\mathrm{R}}^{\mathrm{eff}}|$ decreases as $|\Delta\Phi_{\mathrm{NM-Bi2O3}}|$ increases and the trend of calculated $|\alpha_{\mathrm{R}}|$ is in good agreement with the experimental results. Additionally, the sign change of $\alpha_{\mathrm{R}}^{\mathrm{eff}}$ between Ag/Bi_2O_3 and Cu/Bi_2O_3 occurs near $\Delta\Phi_{\mathrm{NM-Bi2O3}}=0$ as shown in Fig. 4-8(b).

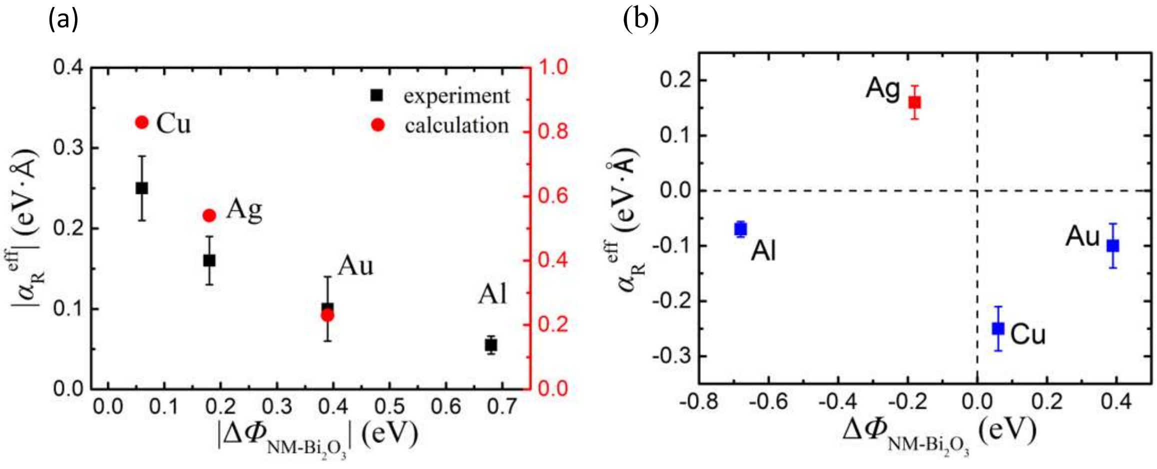

Figure 4-8 (a) Absolute value $|\alpha_R{}^{\mathrm{eff}}|$ in various NM/Bi$_2$O$_3$ interfaces as a function of $|\Delta\Phi_{\mathrm{NM\text{-}Bi2O3}}|$ between NM and Bi$_2$O$_3$. (b) $\alpha_R{}^{\mathrm{eff}}$ as a function of $\Delta\Phi_{\mathrm{NM\text{-}Bi2O3}}$ between NM and Bi$_2$O$_3$.

To understand the relation between work function difference and α_R, again we start from the relation $\alpha_R = (\frac{2}{c^2}) \int (\partial V/\partial z)\, |\psi|^2\, dz$. We investigated the charge density distribution $|\psi|^2$ and potential V at NM=Cu, Ag, Au(111)/α-Bi$_2$O$_3$ by first-principle calculation as shown in Fig. 4-9. The details of calculation will be explained in section 4.7. The potential V of Cu, Ag, and Au are very similar while their $|\boldsymbol{\psi}|^2$ has very different shape which indicates that $|\boldsymbol{\psi}|^2$ is the main reason of strong NM dependence. Here we discuss how work function difference modulates $|\boldsymbol{\psi}|^2$ and α_R. Firstly, we compare Cu/Bi$_2$O$_3$ and Au/Bi$_2$O$_3$. In case of Cu, the $|\Delta\Phi_{\mathrm{NM\text{-}Bi2O3}}|$ is smaller than Au and the asymmetric $|\psi|^2$ is more strongly localized near Cu nuclei where the $\partial V/\partial z$ of Columb potential becomes largest as shown in Fig. 4-9(a). In case of Au, the peak of $|\psi|^2$ is shifted by a larger $|\Delta\Phi_{\mathrm{NM\text{-}Bi2O3}}|$ from Au nuclei and delocalized by charge transfer due to interfacial electric field as shown in Fig. 4-9(c). Thus, the integral of $\int (\partial V/\partial z)\, |\psi|^2\, dz$ becomes smaller in case of Au because $|\psi|^2$ is not localized in the largest $\partial V/\partial z$ region. Therefore, $|\alpha_R|$ decreases as $|\Delta\Phi_{\mathrm{NM\text{-}Bi2O3}}|$ increases. This charge-transfer-induced delocalization of $|\psi|^2$ is often discussed in ferroelectric oxides by Wannier functions [4-25].

Secondly, we discuss the different sign of α_R between Ag/Bi$_2$O$_3$ and Cu/Bi$_2$O$_3$. Because the $\partial V/\partial z$ is an antisymmetric Coulomb potential near NM nucleus, sign of α_R

is determined by whether the excess electron density is localized on NM side or Bi_2O_3 side. The opposite sign between Ag/Bi_2O_3 and Cu/Bi_2O_3 should come from the different asymmetry of $|\psi|^2$. When there is a sign change of $\Delta\Phi$, the interfacial electric field change its direction. Assuming that Ag/Bi_2O_3 and Cu/Bi_2O_3 interfaces have similar hybridization state, the opposite direction of electric field may shift the $|\psi|^2$ to different side of NM or Bi_2O_3 and then cause the sign change of α_R. This opposite direction shift is demonstrated by calculation results in Fig. 4-9(a) and (b). Also in case of Gd(0001) and O/Gd(0001) surface, it has been reported that the sign change behavior is caused by asymmetry of $|\psi|^2$ due to top oxide layer [4-26]. While in case of Al/Bi_2O_3 interface, the sign is not as expected by the same scenario as NM = Ag, Cu, and Au. Since Al itself has quite different electronic state with Ag, Cu, and Au (group 11 elements), the hybridization state at Al/Bi_2O_3 interface may have different asymmetric feature with others and that's why Al/Bi_2O_3 interface does not have the same sign as Ag/Bi_2O_3 though their $\Delta\Phi_{NM\text{-}Bi2O3}$ are both negative.

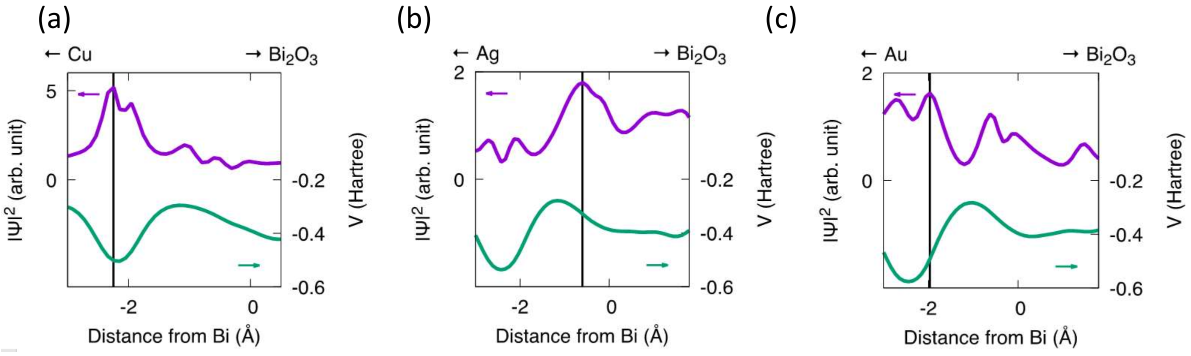

Figure 4-9. Charge density distribution $|\boldsymbol{\psi}|^2$ and the planar averaged electrostatic potential V of (a) Cu/Bi_2O_3 (b) Ag/Bi_2O_3 (c) Au/Bi_2O_3. The origin is fixed to the position of the nearest neighbor Bi atom from top NM atom. The vertical line represents the position of the peak of $|\boldsymbol{\psi}|^2$.

4.7 First-principles calculations results

The details of electronic state such as charge density and electrostatic potential at NM/Bi_2O_3 interface were investigated by first-principles calculations. Fig. 4-10 (a)-(b) shows the electronic states of the NM(111)/ α -Bi_2O_3 interfaces of which local crystallographic configuration is similar to that of our sample (see section 4.5.1). Fig. 4-4(c) shows the schematic of the first Brillouin zone of α-Bi_2O_3. The in-plane length of unit cell is based on the experimental lattice constant of each NM. We also assumed other local crystallographic configuration for the NM/Bi_2O_3 interfaces in terms of the out of plane arrangement of NM and the crystal phases of Bi_2O_3 (e.g. NM(110)/ β -Bi_2O_3). The calculated α_{R} is in the same order of magnitude for both interfaces. From our thickness dependence calculation, we found that the electronic structures were insensitive to the number of NM layers once the number of layers exceeds 16. Fig. 4-11 shows the band structure for the NM(111)/$\boldsymbol{\alpha}$-Bi_2O_3 systems, where the symmetry points (Γ, C, X) are those in the first Brillouin zone shown. There is a free-electron-like band around C-point near the Fermi energy for each system, and its Rashba spin splitting is anisotropic. Fig. 4-6 shows the spin textures for the NM(111)/α-Bi_2O_3 system. The anisotropic Rashba spin structures are shown for NM = Cu (Fig. 4-12 (a)) and for NM = Ag (Fig. 4-12 (b)), while the non-Rashba type spin structures are shown for NM = Au (Fig. 4-12 (c)). Since $\boldsymbol{\alpha}$-Bi_2O_3 is monoclinic ($P2_1/c$, No. 14) and C-point is Brillouin zone-boundary, each system has no 4-fold rotational symmetry around C-point that makes Fermi surface and spin textures isotropic. The anisotropic Rashba spin vortices for NM = Cu and Ag are opposite to each other (e.g. The inner (outer) vortex for NM = Cu is the clockwise (anti-clockwise), while that for NM = Ag is the anti-clockwise (clockwise), which may support our experimental result that the sign of $\boldsymbol{\alpha}_{\mathbf{R}}{}^{\mathbf{eff}}$ in Ag/Bi_2O_3 is positive while that in Cu/Bi_2O_3 is negative. For NM = Au, there are non-Rashba type spin splitting. This may be due to strong SOC of Au. On the other hand, in the experiment, a symmetric circular spin structure was observed by angle dependence results but not an anisotropic one, because the amorphous Bi_2O_3 results in a symmetric potential in x-y plane. We obtained the Rashba coefficients $\boldsymbol{\alpha}_{\mathbf{R}}$ as the average of the ones along CΓ and CX line around C-point. A trend in the Rashba spin splitting is corresponding to experimental one as shown in Table 1. The experimental values of $|\alpha_R|$ are about 3 times smaller than the calculated values; this difference may come from the different structure between real samples and the calculations. In the experiment the deposited Bi_2O_3 layer is amorphous, so it is reasonable that the smaller α_R is obtained by experiments.

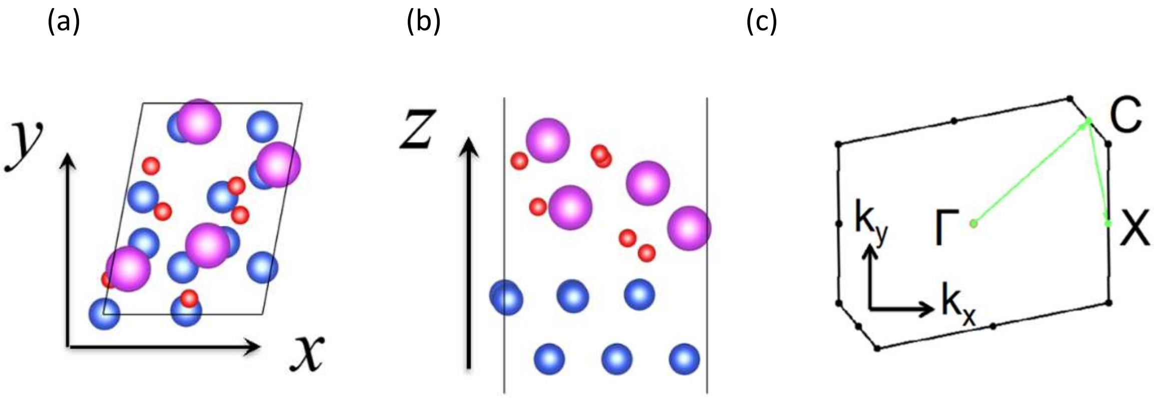

Figure 4-10 Atomic structure of NM(111)/α-Bi_2O_3; (a) top view; (b) side view. Blue, purple and red circles correspond to NM material, Bismuth and Oxygen. (c) The schematic of the first Brillouin zone of α-Bi_2O_3

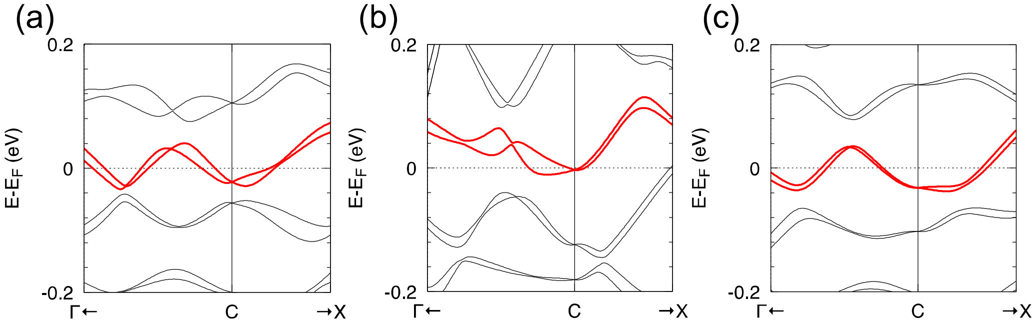

Figure 4-11 Band structures for NM(111)/α-Bi_2O_3. (a) NM = Cu; (b) NM=Ag; (c) NM=Au. The enlarged views of the band structures around C-point are shown through each path from C-point to the point dividing CΓ or CX line internally in the ratio 1:4.

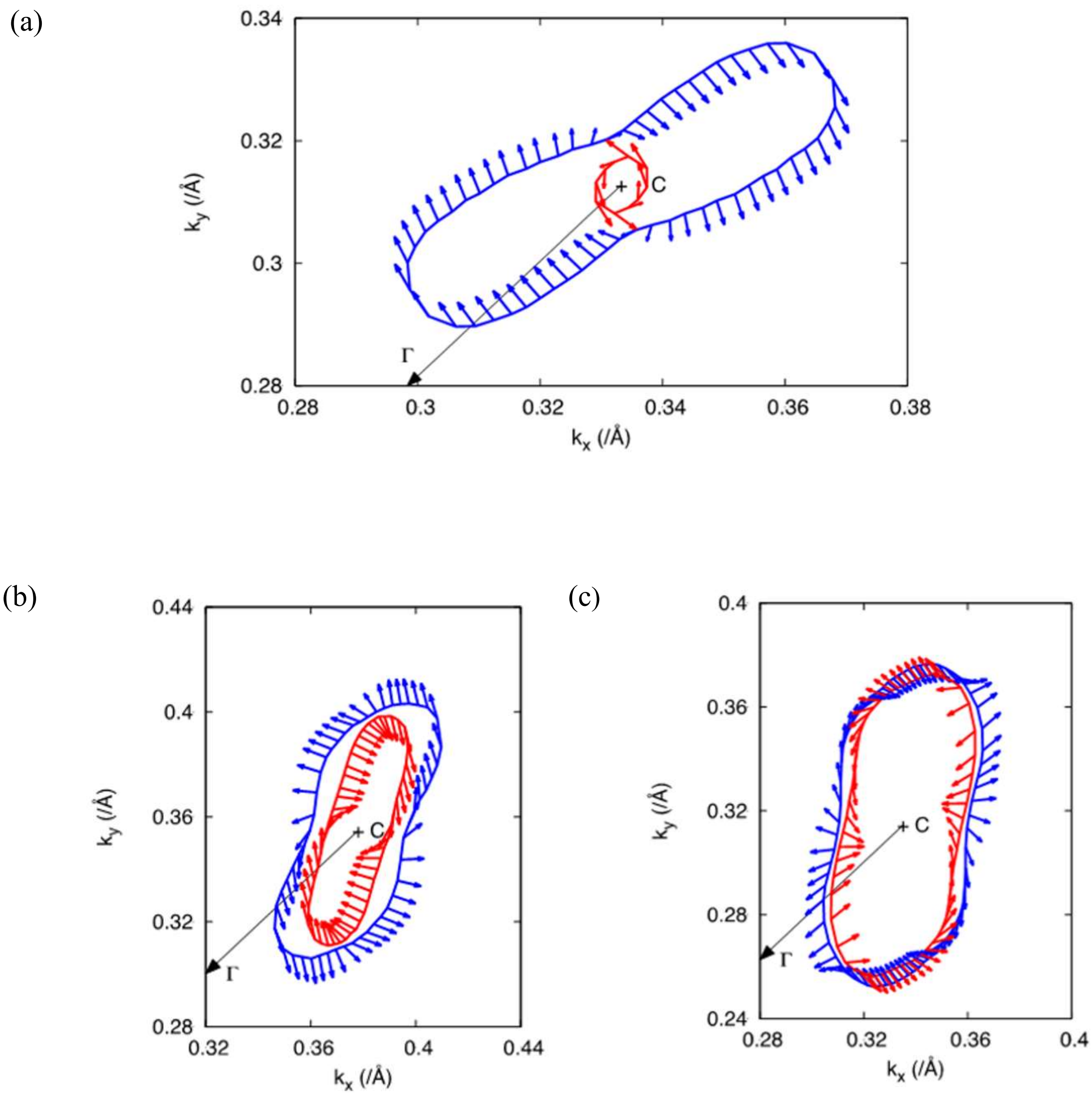

Figure 4-12 Spin textures of (a) Cu(111)/α-Bi_2O_3; (b) Ag(111)/α-Bi_2O_3; (c) Au(111)/α-Bi_2O_3. The black arrow shows CΓ line in the first Brillouin zone.

To understand the role of atomic SOC, the strength dependence of SOC in Bi on the $\boldsymbol{\alpha}_{\mathbf{R}}$ is investigated as shown in Fig. 4-13. $\boldsymbol{\alpha}_{\mathbf{R}}$ without SOC of Bi is in the order of each NM (111) surface state. For NM = Cu and Ag, the $\boldsymbol{\alpha}_{\mathbf{R}}$ drastically increases as the strength of SOC of Bi increases, while the $\boldsymbol{\alpha}_{\mathbf{R}}$ slightly decreases for NM = Au. This result suggest that the large SOC dominates the Rashba splitting in Cu and Ag case.

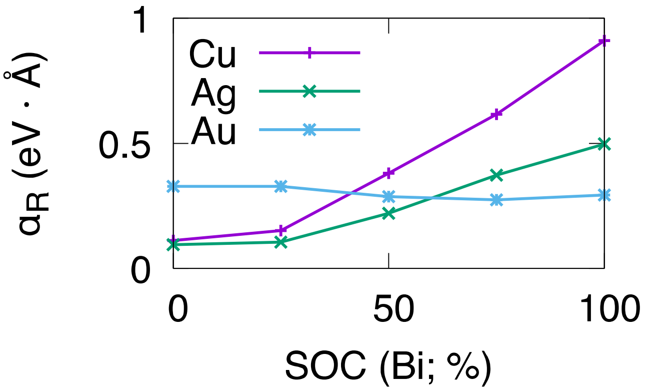

Figure 4-13. Strength dependence of SOC of Bi on Rashba coefficient $\boldsymbol{\alpha}_{\mathbf{R}}$ for NM(111)/α-Bi_2O_3.

4.8 Summary of chapter 4

We have observed the large magnitude variation and sign change of S-C conversion originated from modulation of Rashba spin-splitting at various NM/Bi_2O_3 interfaces. This strong variation comes from the material dependent electron distribution near the interface. The experimental results, supported by calculation, suggest that $|\psi|^2$ could be controlled by tuning interfacial electric field between NM and Bi_2O_3. The estimated Rashba parameter of NM/Bi_2O_3 is one order smaller the Ag/Bi interfaces. This reduction can be explained by the lack of interface alloying structure at oxide/metal interfaces. However, despite of the one order smaller α_{R} , λ_{IEE} at NM(Cu, Ag)/Bi_2O_3 is comparable to reported value of Ag/Bi, 0.3 nm. The reason may be that in case of Ag/Bi metallic interfaces, part of spin current is absorbed by Bi layer since Bi has large SOC and notable spin Hall effect; therefore, the spin current converted to charge current at Ag/Bi interface is less than totally injected spin current. On the other hand, in case of NM/Bi_2O_3 interfaces, the injected spin current is converted only at NM/Bi_2O_3 interfaces since Bi_2O_3 is insulator. Thus, NM/oxide interfaces have a great potential of more efficient S-C conversion than metallic interfaces. This study have shown an effective way to tune the magnitude and sign of S-C conversion by changing the electron distribution and provided a guiding principle for finding novel NM/oxide interfaces in the future.

Reference of chapter 4

[4-1] H. Bentmann, T. Kuzumaki, G. Bihlmayer, S. Blügel, E. Chulkov, F. Reinert and K. Sakamoto, *Physical Review B* **84**, no. 11 (2011).

[4-2] M. Nagano, A. Kodama, T. Shishidou and T. Oguchi, *J. Phys. Condens. Matter.* **21**, no. 6, p. 064239 (2009)

[4-3] J. Sánchez, L. Vila, G. Desfonds, S. Gambarelli, J. Attané, J. De Teresa, C. Magén and A. Fert, *Nature Communications* **4**, no. 1 (2013).

[4-4] S. Karube, K. Kondou and Y. Otani, *Applied Physics Express* **9**, no. 3, p. 033001 (2016).

[4-5] Y. Niimi, H. Suzuki, Y. Kawanishi, Y. Omori, T. Valet, A. Fert and Y. Otani, *Physical Review B* **89**, no. 5 (2014).

[4-6] H. Wang, C. Du, Y. Pu, R. Adur, P. Hammel and F. Yang, *Physical Review Letters* **112**, no. 19 (2014).

[4-7] O. Mosendz, V. Vlaminck, J. Pearson, F. Fradin, G. Bauer, S. Bader and A. Hoffmann, *Physical Review B* **82**, no. 21 (2010).

[4-8] V. Vlaminck, J. Pearson, S. Bader and A. Hoffmann, *Physical Review B* **88**, no. 6, (2013).

[4-9] Y. Tserkovnyak, A. Brataas and G. Bauer, *Physical Review Letters* **88**, no. 11 (2002).

[4-10] W. Zhang, M. Jungfleisch, W. Jiang, J. Pearson and A. Hoffmann, *Journal of Applied Physics* **117**, no. 17, pp. 17C727 (2015).

[4-11] M. Isasa, M. Martínez-Velarte, E. Villamor, C. Magén, L. Morellón, J. De Teresa, M. Ibarra, G. Vignale, E. Chulkov, E. Krasovskii, L. Hueso and F. Casanova, *Physical Review B* **93**, no. 1 (2016).

[4-12] K. Shen, G. Vignale and R. Raimondi, *Physical Review Letters* **112**, no. 9, (2014).

[4-13] K. Ando, Y. Kajiwara, K. Sasage, K. Uchida and E. Saitoh, *IEEE Transactions on Magnetics* **46**, no. 6, pp. 1331-1333 (2010).

[4-14] B. Heinrich, J. Cochran and R. Hasegawa, "FMR linebroadening in metals due to two - magnon scattering", *Journal of Applied Physics* **57**, no. 8, pp. 3690-3692 (1985).

[4-15] Y. Tserkovnyak, A. Brataas, G. Bauer and B. Halperin, *Reviews of Modern Physics* **77**, no. 4, pp. 1375-1421, (2005).

[4-16] Y. Otani and T. Kimura, *Philosophical Transactions of the Royal Society A: Mathematical, Physical and Engineering Sciences* **369**, no. 1948, pp. 3136-3149 (2011).

[4-17] M. Costache, S. Watts, M. Sladkov, C. van der Wal and B. van Wees, *Applied Physics Letters* **89**, no. 23, p. 232115 (2006).

[4-18] Y. Fukuma, L. Wang, H. Idzuchi, S. Takahashi, S. Maekawa and Y. Otani, *Nature Materials* **10**, no. 7, pp. 527-531 (2011).

[4-19] S. Valenzuela and M. Tinkham, *Nature* **442**, no. 7099, pp. 176-179 (2006).

[4-20] H. Bentmann, F. Forster, G. Bihlmayer, E. Chulkov, L. Moreschini, M. Grioni and F. Reinert, *Europhysics Letter* **87**, no. 3, p. 37003, (2009)

[4-21] G. Bian, X. Wang, T. Miller and T. Chiang, *Physical Review B* **88**, no. 8 (2013).

[4-22] K. Takeuchi, A. Suda and S. Ushioda, *Surface Science* **489**, no. 1-3, pp. 100-106 (2001).

[4-23] J. Hölzl, & F. Schulte, *Work function of metals*. (1979).

[4-24] Q. Li and Z. Zhao, *Physics Letters A* **379**, no. 42, pp. 2766-2771 (2015).

[4-25] P. Ghosez, J. Michenaud and X. Gonze, *Physical Review B* **58**, 6224 (1998).

[4-26] O. Krupin, G. Bihlmayer, K. Starke, S. Gorovikov, J. Prieto, K. Döbrich, S. Blügel and G. Kaindl, *Physical Review B* **71**, no. 20 (2005).

Chapter 5

Efficient spin conversion at Cu(Ag)/oxide interfaces without heavy elements

In chapter 4, we investigated Rashba parameter α_{R} at various metal / Bi_2O_3 interfaces. Our results suggest a way to design metal materials from work function difference. Moreover, it is important to understand how to choose the oxide materials at metal/oxide Rashba interfaces as well. We have shown that the SOC of metal layer have almost no contribution on Rashba parameter at metal/Bi_2O_3 interface because the SOC of Bi is much larger than metal layer. Following this conclusion, using other oxide materials instead of Bi_2O_3 should change SOC and have notable effect on α_{R}. There are at least two contribution of oxide materials on α_{R}: SOC of oxide materials and oxide materials dependence electron distribution. Because Bi have the largest SOC in non-radioactive materials, using other metal-oxide materials should results in smaller SOC and α_{R}. Besides, different electron distribution with strong localization or asymmetry can possibly increases or decreases α_{R} as introduced in chapter 4. In this chapter, we investigate the S-C conversion at various Cu/oxide interfaces to understand how the oxide materials dependent SOC and electron distribution influent α_{R}. Surprisingly, we found that the S-C conversion efficiency λ_{IEE} at Cu/ITO (Indium Tin oxide) interface has the same magnitude as Cu/Bi_2O_3 but with opposite sign though the SOC of Indium and Tin are about 5-6 times smaller than Bi [5-1, 5-2]. To make sure the detected conversion signal doesn't come from ITO layer, we investigate both S-C and C-S conversion at Py/Cu(Ag)/ITO trilayers and Py/ITO bilayers samples and succeed to observe both inverse and direct Edelstein effect at

Cu(Ag)/ITO interfaces. Our results indicate that heavy element is not necessary for efficient spin-charge interconversion [5-3].

5.1 Spin-to-charge current conversion at various Cu/oxide interfaces

We prepared Py(5 nm)/Cu(20 nm)/oxide(30 nm) tri-layer samples for investigating oxide materials dependence. The experiment setup and sample structure are the same as chapter 4. We use SnO_2, HfO_2, Al_2O_3, SiO_2, ITO (Indium Tin Oxide) as the oxide materials. The measured spin pumping spectrum of at 9 GHz with 20 dBm rf current is shown in Fig. 5-1. Except Cu/ITO interface, magnitudes of all the signals are at least 1 order smaller than Cu/Bi_2O_3 interface.

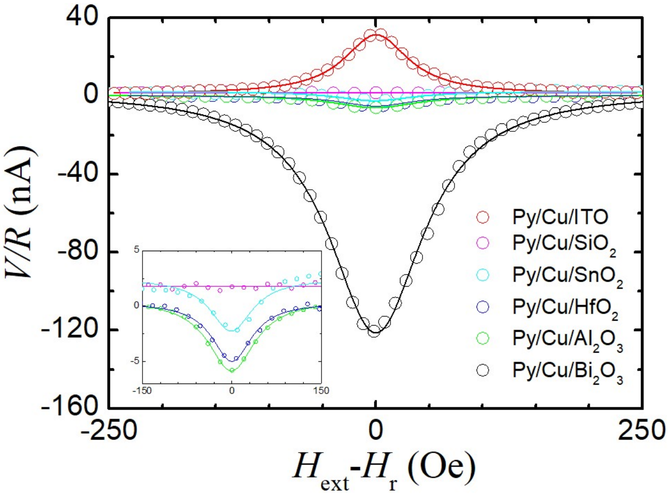

Figure 5-1 Detected *V/R* spectrum of Py/Cu/ITO, Py/Cu/SiO_2, Py/Cu/SnO_2, Py/Cu/HfO_2, Py/Cu/Al_2O_3, and Py/Cu/Bi_2O_3 from spin pumping measurement

Firstly, we compare the spin-orbit coupling constant ζ of the Sn, Hf, Al, Si, In, and Sn. Fig. 5-2 shows the value of ζ as a function of atomic number reported by Y. Yanase and H. Harima. Fig. 5-3(a) shows the detected V/R signal as a function of ζ. Al and Si are light elements with neglected small ζ. As expected, much smaller S-C conversion signals of Cu/Al_2O_3, SiO_2 than Cu/Bi_2O_3 is observed as shown in. In, Sn, and Hf has similar ζ~0.02; however, detected *V/R* signals of Cu/SnO_2, HfO_2 have the similar magnitude with Cu/Al_2O_3 while only Cu/ITO shows notable signal which is 5 times larger than Cu/SnO_2,

HfO_2. Such large signal of Cu/ITO cannot be explained by the strength of SOC. To check if the large signal of ITO is related to the work function difference, we compare the work function difference between Cu and oxide layer with the detected *V/R* signal as shown in Fig. 5-3(b). We use reported value of work function Φ of Cu (111) [5-4], α- Bi_2O_3 [5-5] , SiO_2, Al_2O_3, SnO_2 [5-6], ITO[5-7], as 4.96, 4.92, 5.00, 4.70, 4.84, and 4.70 in units of eV, respectively. We cannot find a reported value for HfO_2 so it is excluded. The work function difference of ITO is 2 times larger than SnO_2 while the signal is 5 times larger. This trend is complete different with what we found from the metal materials dependence. The possible origins will be discussed in section 5.4.

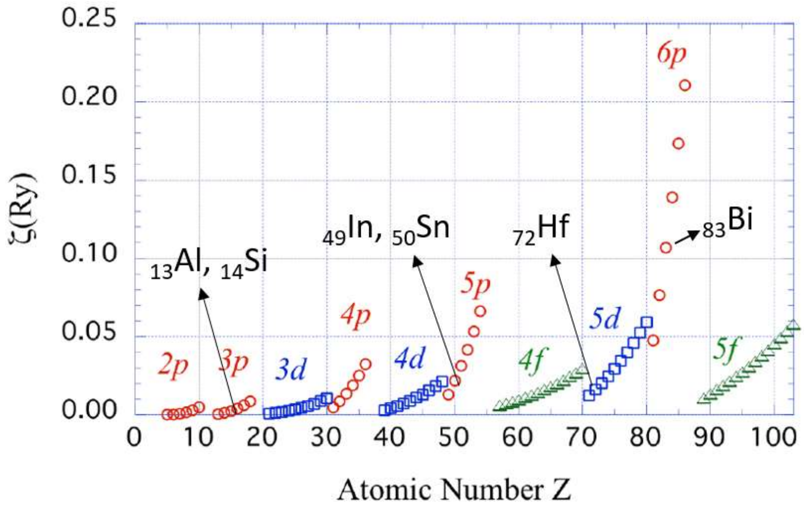

Figure 5-2 Spin-orbit coupling constant ζ as a function of atomic number Z. [6-2]

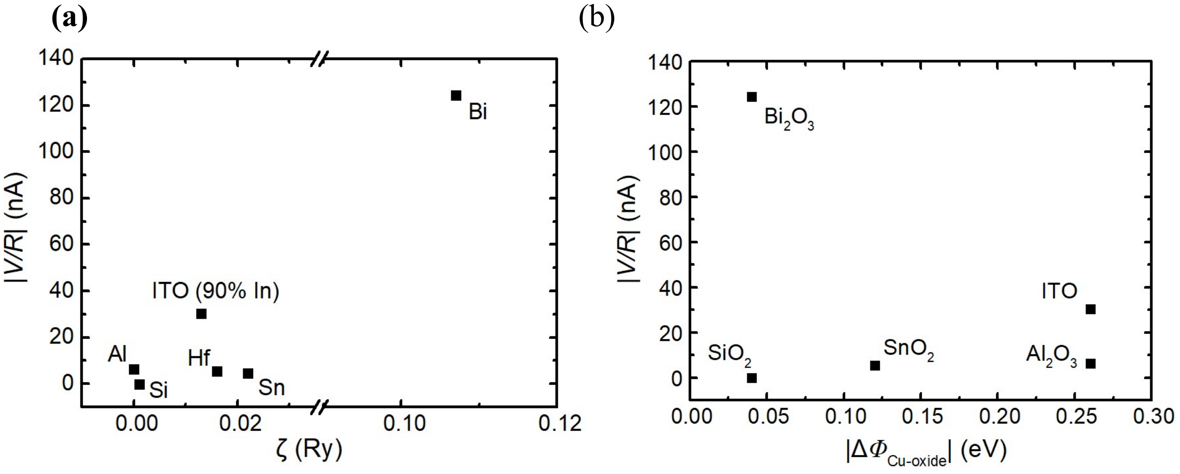

Figure 5-3 (a) Detected V/R signal as a function of spin-orbit coupling constant ζ of the metal element in each metal-oxide material. (b) Detected V/R signal as a function of work function difference $\Delta\Phi_{\text{Cu-oxide}}$.

5.2 Spin-to-charge conversion at Cu(Ag)/ ITO interfaces

Because ITO is the only conductive materials in the oxide materials we used, ISHE of ITO may also contribute to the S-C conversion measured by spin pumping method. To clarify the contribution of ITO layer, we prepared Py/Cu/ITO, Py/Ag/ITO, and Py/ITO samples for spin pumping measurement. The weight ratio of the ITO (In_2O_3/SnO_2) target was 90% vs. 10%. The resistivity of Cu, Ag, and ITO films were 10 μΩ cm,9 μΩ cm, and 0.75 mΩ cm at room temperature. We compared the S-C conversion signal at the Py/Cu(Ag)/ITO trilayer samples and Py/ITO reference samples as shown in Fig. 5-4. Clear *V/R* signal is detected at Py/Cu(Ag)/ITO samples while there is much smaller signal detected at Py/ITO interface, which indicates that the the contribution of Cu(Ag)/ITO dominant the S-C conversion. Using the same analysis method as chapter 4, we calculate the damping constant δ_{eff} and S-C conversion efficiency λ_{IEE} of Cu(Ag)/ITO and compare them with Cu(Ag)/Bi_2O_3 interfaces as shown in table 5-1. Surprisingly, the magnitude of conversion efficiency of Cu/ITO is the same as Cu/Bi_2O_3 interfaces while that of Ag/ITO is twice larger than Ag/Bi_2O_3. This result suggest that the heavy element may be not necessary for efficient S-C conversion. In addition, the we found that the damping constant δ_{eff} of Py/Cu(Ag)/ITO are much smaller than Py/Cu(Ag)/Bi_2O_3 interface. This result indicates that the total spin current generated from spin pumping of Cu(Ag)/ITO interfaces is less than Cu(Ag)/Bi_2O_3 interfaces. Since the spin current injected from Py layer to Cu(Ag) layer should be the same, the less spin current generated indicates that the back flow of spin current from Cu(Ag)/ITO interface is larger than Cu(Ag)/Bi_2O_3 interfaces. That is, when the same amount of spin current is injected into the interface, less spin current is converted to charge current and more spin current is reflected as the backflow at Cu(Ag)/ITO than Cu(Ag)/Bi_2O_3.

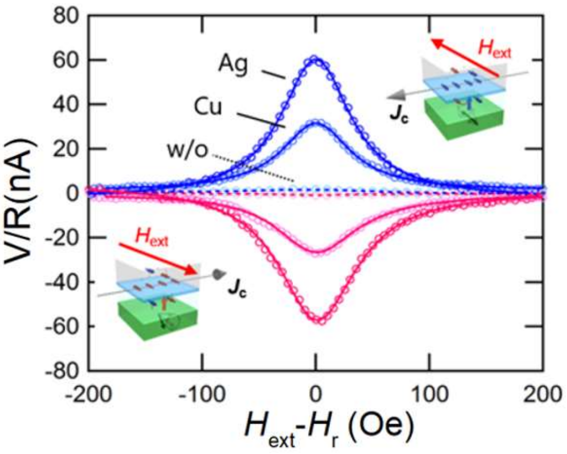

Figure 5-4 Detected *V/R* spectrum of Py/Ag/ITO, Py/Cu/ITO, and Py/ITO (w/o)

Interface	λ_{IEE}(nm)	$\boldsymbol{\delta}_{\mathbf{eff}}$
Py/Cu/ITO	+0.17	0.0116
Py/Ag/ITO	+0.35	0.0114
Py/Cu/Bi_2O_3	- 0.17	0.0154
Py/Ag/Bi_2O_3	+0.15	0.0168

Table 5-1 S-C conversion efficiency λ_{IEE} and damping constant δ_{eff} of Py/Cu/ITO, Py/Ag/ITO, Py/Cu/Bi_2O_3, and Py/Ag/Bi_2O_3

5.3 Charge-to-spin conversion at Cu(Ag)/ ITO

In section 5.2, we found that λ_{IEE} at Cu(Ag)/ITO can be comparable or larger than Cu(Ag)/Bi_2O_3. This finding provides a new direction for designing Rashba interfaces for efficient S-C conversion without heavy elements. It is worth to understand whether an efficient charge-to-spin conversion can also be achieved at the Cu(Ag)/ITO interface. In case of Cu/Bi_2O_3, it has been shown that the C-S conversion efficiency q_{DEE} is comparable to Pt [5-8, 5-9]. Note that though the efficiency of q_{DEE} and λ_{IEE} are both proportional to

α_{R}, they have different time scale τ_{DEE} and τ_{IEE} with different relation, $q_{\mathrm{DEE}} \propto \tau_{\mathrm{DEE}}{}^{-1}$ and $\lambda_{\mathrm{IEE}} \propto \tau_{\mathrm{IEE}}$, as introduced in chapter 2. A large λ_{IEE} doesn't necessarily correspond to an efficient q_{DEE}. In this section, we observe the direct Edelstein effect (DEE), a charge-to-spin (C-S) conversion at Cu(Ag)/ITO by the spin-torque FMR measurement introduced in chapter 3. Fig. 5-4 shows the schematic image of sample structure consist of multi-layer wire and Ti/Au coplanar wave guide (CPW). The CPW is deposited on both ends of the wire so that the wire element act as a part of the waveguide. When rf current I_{rf} and direct current I_{dc} is applied to the sample, ferromagnetic resonance (FMR) in NiFe layer is excited by local magnetic field due to I_{rf}. The I_{dc} plays the role of modulation of damping torque by spin torque as shown in Fig. 5-4. During measurement, an external static magnetic field H_{ex} is applied with an angle θ = 45° and 225°. All of measurements were performed at room temperature. Fig. 5-5(a)-(c) show the detected V spectrum at Py/ITO, Py/Cu/ITO, and Py/Ag/ITO interfaces with I_{dc} -25 mA, 0 mA, and 25 mA. In case of Py/ITO there is no modulation of spectrum observed while applying I_{dc} as shown in Fig. 5-5(a), while at Py/Cu/ITO and Py/Ag/ITO, a clear difference of spectrum due to I_{dc} is observed. The amount of damping modulation $\Delta\delta_{\mathrm{eff}}$ due to spin current can be expressed as following equation [5-10]

$$\Delta\delta_{\mathrm{eff}} = \frac{\sin\theta}{(H_{ex} + M_S/2)\mu_0 M_S t_{FM}} \frac{\hbar J_S}{2e} \ , \qquad (5.1)$$

where e is the electron charge, μ_0 is the permeability in vacuum, M_{S} is the saturation magnetization, t_{FM} is the FM layer thickness, θ is the static magnetic field angle from the longitudinal direction of the wire, and $\hbar J_{\mathrm{s}}/2e$ is the spin current density. Fig. 5-5(b)-(d) show the modulation results of the magnetic damping constant ($\Delta\delta_{\mathrm{eff}}$). In the Py/ITO bilayer, we could not observe the finite variation of $\Delta\delta_{\mathrm{eff}}$ as shown in Fig. 5-5(d). On the other hand, in the Py/Cu(Ag)/ITO tri-layer, we observed a clear variation of $\Delta\delta_{\mathrm{eff}}$, as shown in Fig. 5-5(e)-(f). The direction of $\Delta\delta_{\mathrm{eff}}$ is reversed by changing the H_{ex} direction from 45° to 225°, which is caused by switching of the direction of the spin torque.

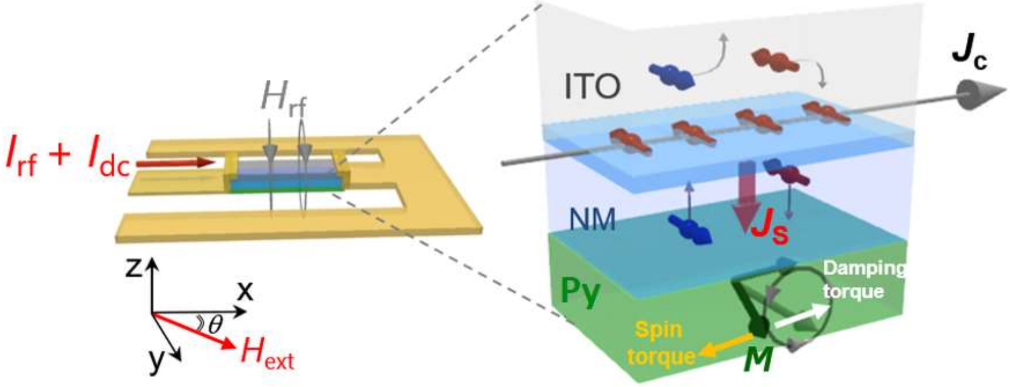

Figure 5-4 Spin torque-ferromagnetic resonance (ST-FMR) measurement circuit and sample structure. Yellow (white) arrows in NiFe layer is corresponds to spin torque (damping torque)

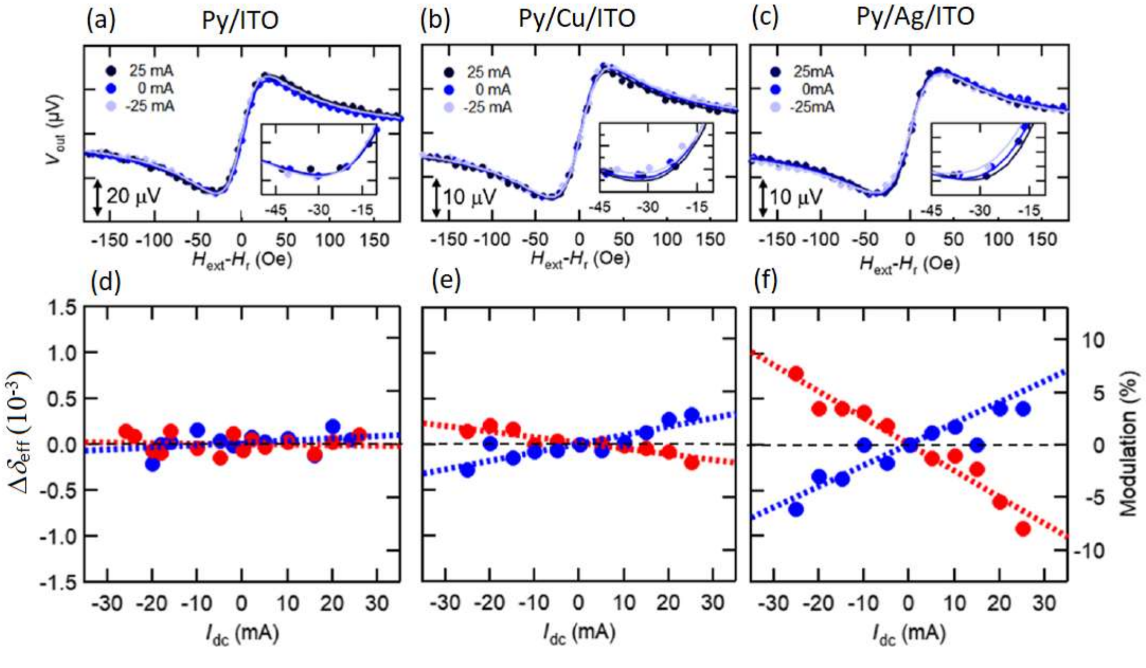

Figure 5-5 (b)-(d) ST-FMR spectrum without dc current. Input frequency and power is 8 GHz and 20 dBm (e)-(g) Modulation of magnetic damping constant ($\Delta\delta_{\text{eff}}$) due to spin current in Py/ITO, Py/Cu/ITO and Py/Ag/ITO

Charge-to-spin conversion coefficient q_{DEE} is defined as $q_{\mathrm{DEE}} = J_S{}^{3D}/J_C{}^{2D}$, where $J_S{}^{3D}$ and $J_C{}^{2D}$ is spin current density generated from the interface and input charge current density at NM/ITO interface, respectively. The values of $J_S{}^{3D}$ can be estimated from damping modulation measurement by using eq. (6.1). $J_C{}^{2D}$ was calculated from conductivity ratio in each layer, assuming the conductivity at interface is the same as the NM layer. Estimated q_{DEE} in NiFe/Cu(Ag)/ITO becomes to 0.061 (0.021) nm^{-1}. This value is comparable to the Cu/Bi_2O_3 interfaces, $q_{\mathrm{DEE}} = 0.025$ nm^{-1} measured by ST-FMR method [5-8]. To compare with typical spin Hall materials, we estimated the spin current conductivity σ_S, which is defined as $\sigma_S = \theta_{SH}\sigma_{NM}$ in SHE and $\sigma_S = q\sigma_{\mathrm{int}}$ in DEE, where θ_{SH}, σ_{NM}, σ_{int} are spin Hall angle, conductivity of spin Hall material and conductivity at interface, respectively [5-11~13]. Estimated spin current conductivity σ_S in Py/Cu(Ag)/ITO becomes to 0.22 (0.67) $(10^{6}\ \Omega^{-1}\mathrm{m}^{-1})$, which values are larger than transition metals of Pt and β–Ta as shown in Fig. 5-6 [5-11, 5-12]. Thus, the efficient C-S and S-C conversion are both observed at Ag(Cu)/ITO interfaces. These results indicate that the heavy element is not necessary to induce the efficient charge-spin interconversion at NM/oxide interface.

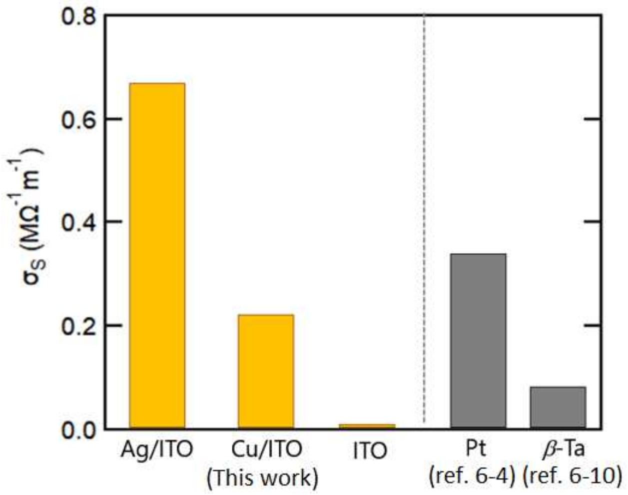

Figure 5-6 Yellow bars show the spin current conductivity σ_S. σ_S in NM/ITO is higher than that of transition metals (Pt, β-Ta).

5.4 Discussion of oxide materials dependence

The S-C conversion efficiency can be expressed by $\lambda_{IEE} \equiv \frac{J_C^{2D}}{J_S^{3D}} = \frac{\alpha_R \tau_{IEE}}{\hbar}$. By using the approximation $\tau_{IEE} \sim \tau_p^{NM}$, where τ_p^{NM} is the momentum relaxation time of metal layer, the estimated $|\alpha_{\mathrm{R}}{}^{\mathrm{eff}}|$ of Cu(Ag)/ITO interface is 0.25 (0.37) eVÅ. Following the scenario of the relation between α_R and work function difference in chapter 4, Fig. 5-7 shows $|\alpha_{\mathrm{R}}{}^{\mathrm{eff}}|$ as a function of $|\Delta\Phi_{\text{NM-oxide}}|$. It seems that the trend of Cu(Ag)/ITO is consistent with NM/Bi_2O_3 interfaces. That is, a smaller work function difference corresponds to a larger $|\alpha_{\mathrm{R}}{}^{\mathrm{eff}}|$. Therefore, we can confirm the large α_{R} at Cu(Ag)/ITO is related to the charge distribution at interface which can be modulated by work function difference. It should be note that the story of work function difference cannot be used to explain the oxide materials dependence since the strength of SOC also depends on oxide materials. From the reported value of SOC [5-1], we found that Bi has 5-6 times larger SOC than In and Sn but Cu(Ag)/ITO and Cu(Ag)/Bi_2O_3 have comparable α_{R}. From the relation $\alpha_{\mathrm{R}} = (\frac{2}{c^2}) \int (\partial V/\partial z)\, |\psi|^2\, dz$, because $\partial V/\partial z$ of Bi is larger than In and Sn, the only reason of the comparable α_{R} at Cu(Ag)/ITO should be the electron distribution $|\psi|^2$. Though it is impossible to tell the exact shape of $|\psi|^2$ at NM/ITO interface from our experiment results, there is a hypothesis that the conductive feature of ITO may lead to a different $|\psi|^2$ with insulating Bi_2O_3. In case of metal/Bi_2O_3 interface, because Bi_2O_3 layer is insulator, conduction electrons all come from metal layer. Part of the them are shifted into Bi_2O_3 layer by charge-transfer as shown in chapter 4. In contrast, in case of metal/ITO interface, because ITO layer is conductive, originally there are conduction electrons of ITO layer locating near In or Sn nuclei. The localized electrons near In or Sn should be more than Bi case even after the charge-transfer with metal layer. As the results, though ITO has much smaller SOC and $\partial V/\partial z$, because there are more electrons locating near In and Sn. The total contribution of SOC on α_{R} at NM/ITO may become comparable to NM/Bi_2O_3. However, since the asymmetry of $|\psi|^2$ which depend on the hybridization state [5-14], is another important essence to determine α_{R}, whether the conductive feature can really enhance α_{R} is still unknown. A further experiment and calculation, i.e. a comparison between Cu/ITO and Cu/In_2O_3, is required to clarify the origins of large Rashba spin-splitting at metal/ITO interfaces.

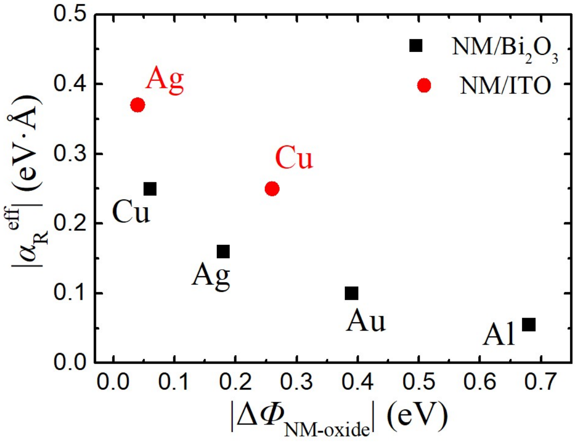

Figure 5-7. Absolute value $|\alpha_R^{eff}|$ of Ag(Cu)/ITO and NM/Bi_2O_3 interfaces as a function of work function difference $|\Delta\Phi_{NM\text{-}oxide}|$.

5.5 Summary of chapter 5

In this chapter, we investigate the S-C conversion efficiency λ_{IEE} at various Cu/oxide interfaces. Though the SOC of oxide materials is similar in SnO_2, HfO_2, and ITO, only Cu/ITO interface shows a notable S-C conversion signal. We investigate both S-C conversion via IEE and C-S conversion via DEE at Cu(Ag)/ITO interfaces. Surprisingly, estimated λ_{IEE} at Cu(Ag)/ITO interface becomes to 0.17 (0.35) nm which is comparable to Cu/Bi_2O_3 interfaces. Furthermore, we found that spin current conductivity for charge-to-spin conversion in Cu(Ag)/ITO interfaces can be larger than Pt and β-Ta. These experimental results imply that the heavy element is not necessary to realize an efficient spin-charge interconversion at NM/Oxide interface. In addition, the estimated α_R of Cu(Ag)/ITO is comparable to Cu(Ag)/Bi_2O_3 even though the SOC of In and Sn is much smaller than Bi. This large Rashba spin-splitting comes from the electron distribution which may be related with the conductive feature of ITO layer. These finding should provide a new perspective to material search of efficient spin current generator and detector.

Reference of chapter 5

[5-1] Y. Yanase, H. Harima, "Spin-orbit interactions and electronic states in crystals (part 1)" Solid State Physics **46** (No. 5), 299 (2011)

[5-2] K. Wittel and R. Manne, *Theoretica Chimica Acta* **33**, no. 4, pp. 347-349 (1974).

[5-3] K. Kondou, H. Tsai, H. Isshiki and Y. Otani, *APL Materials* **6**, no. 10, p. 101105 (2018).

[5-4] K. Takeuchi, A. Suda and S. Ushioda, *Surface Science* **489**, no. 1-3, pp. 100-106, (2001).

[5-5] Q. Li and Z. Zhao, *Physics Letters A* **379**, no. 42, pp. 2766-2771 (2015).

[5-6] V.S. Fomenko: NTIS, US Department of Commerce Report, No.JPRS-56579 (1972).

[5-7] I. D. Parker, Journal of Applied Physics **75**, pp. 1656 (1994).

[5-8] S. Karube, “Enhanced spin relaxation and spin-charge currents interconversion in metal/Bismuth oxide interfaces”, doctor thesis (2017)

[5-9] H. Isshiki, “Inverse and direct Edelstein effects at Bi_2O_3/Cu interface“ (2018) (unpublished)

[5-10] S. Kasai, K. Kondou, H. Sukegawa, S. Mitani, K. Tsukagoshi and Y. Otani, *Applied Physics Letters* **104**, no. 9, p. 092408 (2014).

[5-11] L. Liu, T. Moriyama, D. Ralph and R. Buhrman, *Physical Review Letters* **106**, no. 3, (2011)

[5-12] L. Liu, C. Pai, Y. Li, H. Tseng, D. Ralph and R. Buhrman, *Science* **336**, no. 6081, pp. 555-558, (2012)

[5-13] N. Khang, Y. Ueda and P. Hai, *Nature Materials* **17**, no. 9, pp. 808-813 (2018)

[5-14] M. Nagano, A. Kodama, T. Shishidou and T. Oguchi, *J. Phys. Condens. Matter* **21**, no. 6, p. 064239 (2009)

Chapter 6

Enhancement of spin-to-charge conversion at metal/oxide interface by increasing momentum relaxation time

Spin-to-charge conversion efficiency λ_{IEE} can be described by

$$\lambda_{\mathrm{IEE}} = \alpha_{\mathrm{R}}\tau_{IEE}/\hbar = \alpha_{\mathrm{R}}\tau_p^{int}/\hbar \tag{6.1}$$

where τ_{IEE} and τ_p^{int} is the spin relaxation time and momentum relaxation time at the interface, respectively. In chapter 4 and 5, we have shown that how the species of materials change α_{R} at metal/oxide interfaces by modulation of electron distribution. Besides α_{R}, increasing τ_{IEE} should be another way of enhancing λ_{IEE}. In experiment, it is difficult to determine τ_{IEE} directly by electrical measurement. To estimate τ_{IEE} , we take an approximation $\tau_{IEE} \sim \tau_p^{NM}$ from previous study [6-1], where τ_p^{NM} is the momentum relaxation time of metal layer. However, the accuracy and the origin of this the relation are not clear yet. The purpose of this study is to clarify the relation between τ_{IEE} and τ_p^{NM}, and to enhance λ_{IEE} by increasing τ_p^{NM} without changing α_{R}.

So far, τ_p^{int} of 2DEG at topological insulator or quantum well state have been investigated by several method, i.e. pump probe spectroscopy (PPS) [6-2] ,angle-resolved photoemission (ARPES) [6-3], and weak localization measurement [6-4]. The reported value of τ_p^{int} are in range of several picoseconds. In case of 2DEG at metallic interface, τ_p^{int} becomes much shorter in range of few femtosecond, i.e. Ag/Sn [6-5], Ag/Bi [6-6], and Ag/Fe [6-7] interface. Rojas-Sanchez *et al.* confirmed that such relatively short relaxation times at metallic interfaces is due to the additional relaxation mechanism coming from the hybridization of the 2D states with metallic 3D states [6-5, 6-8]. Following this scenario, previous studies of our group gave the approximation $\tau_p^{int} \sim \tau_p^{NM}$ for metal/oxide interface

[6-1]. In this experiment, the relation between τ_p^{NM} and λ_{IEE} is investigated by measuring Cu thickness dependence at Cu/Bi_2O_3 interfaces. By assuming that α_{R} is independent to Cu thickness (5-30 nm), the relation τ_{IEE}~τ_p^{NM} is obtained. However, more recently another report from our group using another analysis method found that α_{R} depends on Cu thickness in 5-20 nm range which may be due to the possible improvement of crystallization of the Cu as thickness increases [6-9]. This finding is against to the assumption in [6-1]. Therefore, measuring thickness dependence is not a suitable way to determine the relation of τ_{IEE} and τ_p^{NM}. To solve this problem, in this study we change τ_p^{NM} by decreasing temperature because τ_p^{NM} is proportional to the conductivity of metal which can increase tens of percentage at low temperature [6-10]. The relation between τ_p^{NM} and λ_{IEE} can be obtained by measuring temperature dependence at metal/oxide interface. Because the thermal expansion of Cu layer is neglected small (~%0.1) from room temperature to 10K [6-11], there is no temperature dependence of crystallization at interface. Therefore, the variation of α_{R} should be much smaller than the case of thickness dependence which may change the crystallization of Cu layer [6-9]. In this study, we investigated temperature dependence of Cu(Ag)/ Bi_2O_3 from 290 K to 10 K by means of spin pumping. We choose Cu/Bi_2O_3 and Ag/Bi_2O_3 interfaces because they have similar magnitude of $|\lambda_{\mathrm{IEE}}|$ but with opposite sign. If the temperature variation comes from τ_p^{NM}, a similar variation of $|\lambda_{\mathrm{IEE}}|$ should be observed while λ_{IEE} keeps its sign. We succeed to observed 40(17) percentages enhancement of λ_{IEE} at 10 K due to the increased τ_p^{NM} at Cu(Ag)/ Bi_2O_3 interfaces. In addition, we found the relation that $\lambda_{\mathrm{IEE}} \propto \tau_{IEE} \propto \tau_p^{NM}$, which suggests that a larger conversion efficiency λ_{IEE} at metal/oxide interface can be obtained by making higher conductivity metal layer.

6.1 Temperature dependence of spin pumping spectrum

Fig. 6-1(a) shows the measured *V/R* spectrum at 8 GHz of Py/Cu/Bi_2O_3 and Py/Ag/Bi_2O_3 from 290 K to 10 K. Clear resonance peak due to S-C conversion are detected in all temperatures. The opposite sign of the peak is due to the opposite sign of α_{R} between Cu/Bi_2O_3 and Ag/Bi_2O_3 interfaces (see chapter 4). The magnitude of the peak becomes larger at low temperature as shown in Fig. 6-1(b). The same measurement is performed at 7, 7.5, 8, 8.5, and 9 GHz and all of the frequency shows the similar temperature variation.

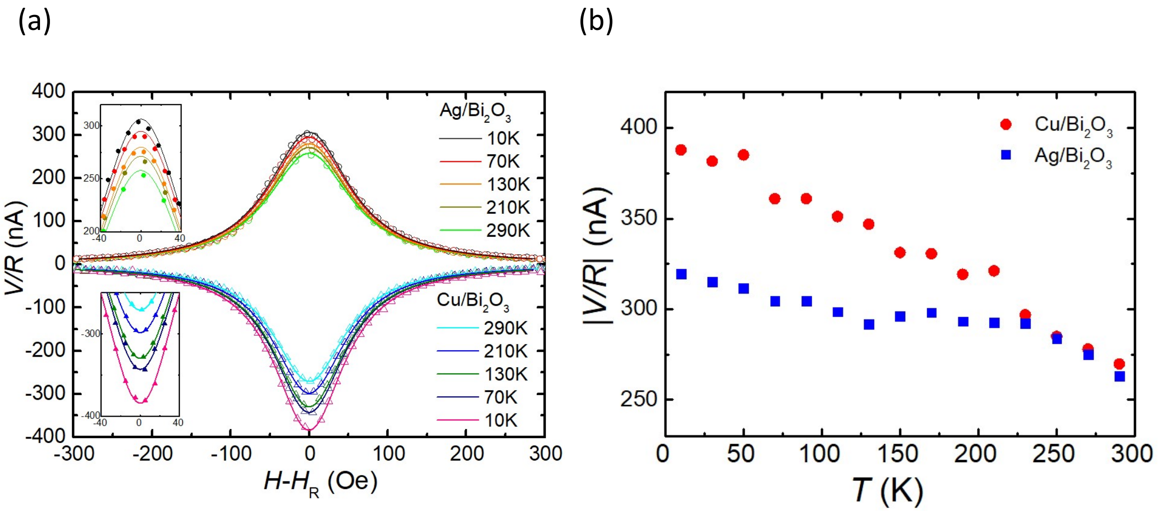

Figure 6-1. (a) Detected *V/R* spectrum of Py/Cu(Ag)/Bi$_2$O$_3$ from 290 K to 10 K at 8 GHz with 20 dBm rf current. (b) Temperature dependence of *V/R* signal at 8 GHz

6.2 Temperature dependence of spin current generation and spin-to-charge conversion

Spin current density injected into NM/Bi$_2$O$_3$ interface is given by [6-12]

$$J_{\mathrm{s(NM/Bi_2O_3)}} = \frac{2e}{\hbar} \times \frac{\hbar g_{\mathrm{eff}}^{\uparrow\downarrow} \gamma^2 (\mu_0 h_{\mathrm{rf}})^2 \left[\mu_0 M_{\mathrm{s}} \gamma_e + \sqrt{(\mu_0 M_{\mathrm{s}})^2 \gamma_e^2 + 4\omega^2}\right]}{8\pi \delta_{\mathrm{F/N/O}}^2 \left[(\mu_0 M_{\mathrm{s}})^2 \gamma_e^2 + 4\omega^2\right]} \tag{6.2}$$

where γ, ${g_{\mathrm{eff}}}^{\uparrow\downarrow}$, $\delta_{\mathrm{F/N/O}}$, M_{s}, ω, and h_{rf} are the gyromagnetic ratio, spin mixing conductance, damping constant, saturation magnetization, angular frequency, and applied rf field, respectively. ${g_{\mathrm{eff}}}^{\uparrow\downarrow}$ can be estimated by using the relation ${g_{\mathrm{eff}}}^{\uparrow\downarrow}= \frac{4\pi M_{\mathrm{s}} t_{\mathrm{F}}}{g\mu_{\mathrm{B}}}\left(\delta_{\mathrm{F/N/O}} - \delta_{\mathrm{F/N}}\right)$, where t_{F}, $\delta_{\mathrm{F/N/O}}$, and $\delta_{\mathrm{F/N}}$ are the thickness of Py, the damping constant for Py/NM/Bi$_2$O$_3$, and the damping constant for Py/NM, respectively. Here we discuss the temperature dependence of each parameter in eq. (6.2). γ and ω are temperature independent. h_{rf} is determined by the impedance of CPW, which is determined by the structure of the waveguide and the permittivity of the substrate [6-13]. Because permittivity of Si substrate has only 2% difference at 10 K and the resulting impedance difference is less than 1%, h_{rf} is also insensitive to temperature [6-14]. In case of $\mu_0 M_{\mathrm{s}}$, we found that the resonance field of FMR is slightly decreased at low temperature because the saturation magnetization $\mu_0 M_{\mathrm{s}}$ of Py bulk increases when temperature decreases as shown in Fig. 6-3(a), which is consist with previous reports [6-15].

The damping constant $\delta_{\mathrm{F/N/O}}$ can be determined by the relation, $\Delta H = \delta_{\mathrm{eff}}\omega/\gamma_e + \Delta H_0$, where ΔH is the half width at half maximum (HWHM). From experiment, both ΔH and $\delta_{\mathrm{F/N/O}}$ of Py/NM(Cu,Ag) Bi_2O_3 samples are insensitive to temperature from 10 K to 290 K as shown in fig. 6-2. Similarly, there is a report that ΔH and δ_{eff} in Py thin film is constant between 10 K to 300 K [6-16, 17]. In contrast, it is reported that the temperature dependence of δ_{eff} in Py(5nm) with capping layer TaN of Al_2O_3 has a peak around 50 K due to the thermally induced spin reorientation for the surface magnetization of the Py thin films [6-15]. However, authors demonstrated that this reorientation phenomenon correspond to a peak in temperature dependence of $\mu_0 M_{\mathrm{s}}$ at 50K, which is not observed in our experiment results. Therefore, it can be assumed that in our samples $\delta_{\mathrm{F/N}}$ have no temperature dependence from 10 K to 290 K. Since $g_{\mathrm{eff}}{}^{\uparrow\downarrow}$ is proportional to $\mu_0 M_{\mathrm{s}}$, $\mu_0 M_{\mathrm{s}}$ and $g_{\mathrm{eff}}{}^{\uparrow\downarrow}$ becomes the only two parameters being temperature dependent in eq. (6.2),. By fitting with Kittel formula, $(\omega_f/\gamma_e)^2 = \mu_0 H_{\mathrm{dc}}(\mu_0 H_{\mathrm{dc}} + \mu_0 M_{\mathrm{s}})$, we derived $\mu_0 M_{\mathrm{s}}$ of the Py layer from the frequency dependence of resonance field. About 7% enhancement of $\mu_0 M_{\mathrm{s}}$ and $g_{\mathrm{eff}}{}^{\uparrow\downarrow}$ is observed at 10 K. As the results, spin current density $J_{\mathrm{s(NM/Bi_2O_3)}}$ increases 3% at 10 K as shown in Fig. 6-3(a). The conversion coefficient λ_{IEE} is calculated by $\lambda_{\mathrm{IEE}} = j_{\mathrm{c}}/J_{\mathrm{s(NM/Bi_2O_3)}}$. Fig. 6-3(b) shows the temperature dependnece of normalized conversion efficiency $\lambda_{\mathrm{IEE(T)}}/\lambda_{\mathrm{IEE(290K)}}$, and normalized conductivity $\sigma_{\mathrm{(T)}}/\sigma_{\mathrm{(290K)}}$ of Cu(Ag)/Bi_2O_3 interface. At 10 K, 40 (17)% enhancement of in λ_{IEE} at Cu(Ag)/Bi_2O_3 is observed. The trend of temperature dependence of σ_{NM} is very similar with λ_{IEE}, which suggests that the enhancement of λ_{IEE} is related to conductivity.

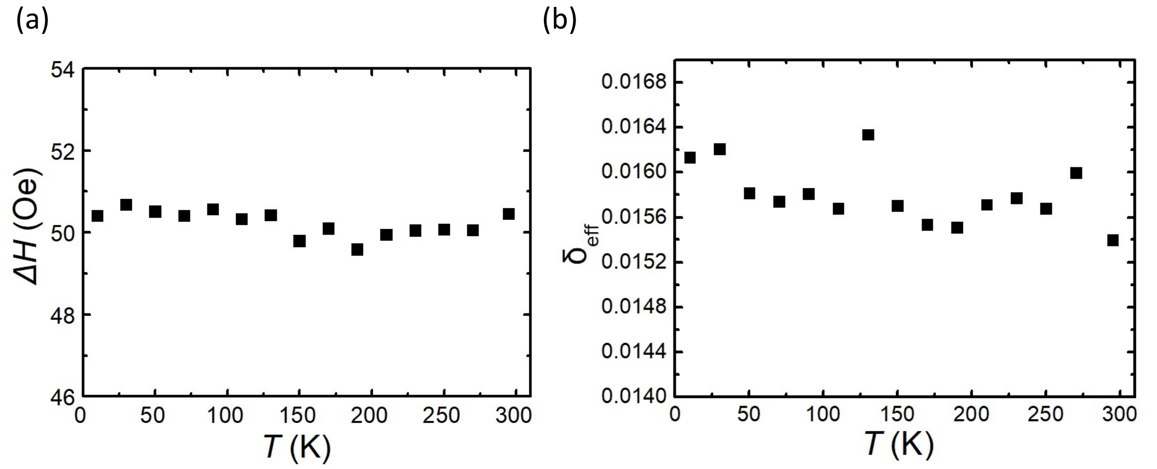

Figure 6-2. Temperature dependence of (a) linewidth of FMR at 8GHz (b) damping constant.

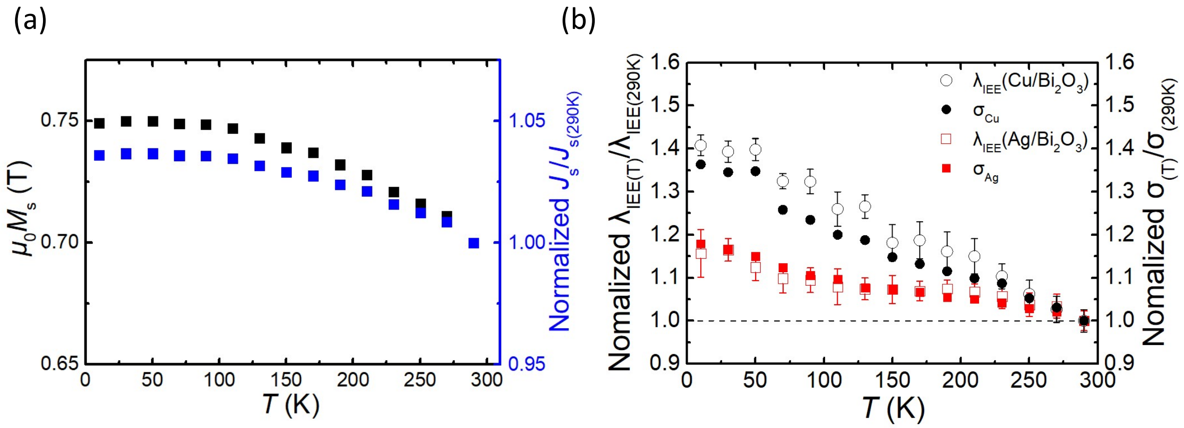

Figure 6-3. (a) Temperature dependence of saturation magnetization $\mu_0 M_\mathrm{s}$ of Py and normalized spin current density $J_{\mathrm{s(T)}}/J_{\mathrm{s(290K)}}$. (b) Temperature dependence of normalized conversion efficiency $\lambda_{\mathrm{IEE(T)}}/\lambda_{\mathrm{IEE(290K)}}$ at Cu(Ag)/Bi_2O_3 and normalized conductivity σ of Cu and Ag layer.

6.3 Conversion coefficient versus momentum relaxation time of metal layer

To understand the relation between λ_{IEE} and τ_p^{NM}, we calculate τ_p^{NM} from σ_{NM} by Drude formula, $\sigma_{\mathrm{NM}} = \tau_{NM}(ne^2/m_e)$, where n, e, and m_e are the carrier density, electron charge and electron mass, respectively. λ_{IEE} as a function of τ_{NM} is shown as Fig. 6-4. The data is well fitted by linear function, $\lambda_{\mathrm{IEE}} = \alpha_R^{eff}\tau_p^{NM}/\hbar$, indicating that λ_{IEE} is proportional to τ_p^{NM} and σ_{NM}. The proportional relation between λ_{IEE} and σ_{NM} indicates that the higher conversion efficiency can be reached by making high conductivity metal layer. Note that when τ_p^{NM} and σ_{NM} is near zero which means the metal layer becomes semiconductor of insulator, the relation of λ_{IEE} should return to $\lambda_{\mathrm{IEE}} = \alpha_{\mathrm{R}}\tau_p^{int}/\hbar$ Therefore, the fitting in Fig. 6-4 is not meaningful at zero point. Interestingly, this relation between conversion efficiency and conductivity is quite different with SHE. It has been reported that the spin Hall angle of materials with a dominant intrinsic contribution to the SHE can be enhanced by decreasing conductivity [6-18]. Therefore, checking the relation between conversion efficiency and conductivity may help us understand the origin of S-C conversion when designing new materials for S-C conversion.

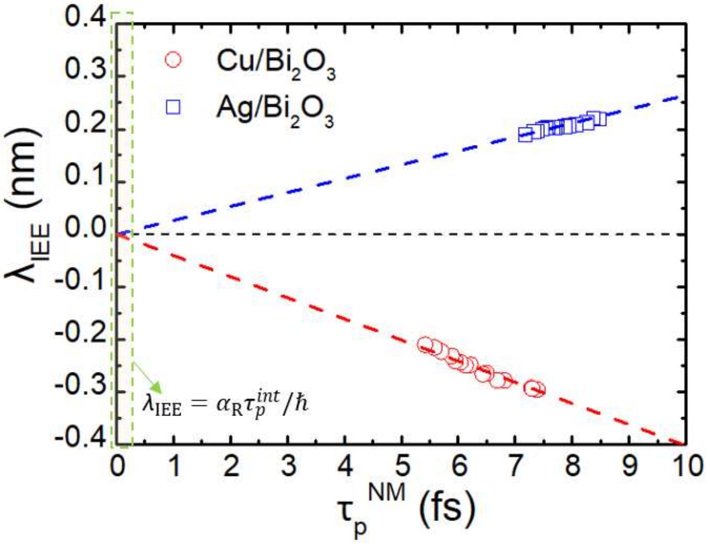

Figure 6-4. λ_{IEE} as a function of momentum relaxation time in NM layer τ_p^{NM}. Near the zero point λ_{IEE} is not related to τ_p^{NM} so the fitting is not meaningful.

Here we discuss the origin of $\lambda_{\mathrm{IEE}} \propto \tau_p^{NM}$. Since λ_{IEE} can be expressed by $\lambda_{\mathrm{IEE}} = \alpha_{\mathrm{R}}\tau_{IEE}/\hbar$, our results indicate that τ_{IEE} is proportional to τ_p^{NM} which is in the order of fs. In contrast, 2DEG Rashba interface in quantum well state like $\mathrm{LaAlO_3}$(LAO)/$\mathrm{SrTiO_3}$(STO) interface, $\tau_{IEE} = \tau_p^{int}$ which is in the order of ps. This difference could be explained by considering the additional momentum relaxation process due to metal layer. For 2DEG at LAO/STO interface, conductive electrons can only move in the 2D Rashba interface. In case of metal/oxide interface, because the interface state is contact with metal layer, a hybridization of Rashba interface state with 3D metallic state can be occurred which enables electrons to move across interface state and 3D bulk state. This possible hybridization has been discussed by J. C. Rojas-Sánchez [6-5] and S. Zhang [6-8]. Fig. 6-5 shows the schematic of momentum relaxation process due to metal layer. Charge current I_c generated by S-C conversion flows through interface and bulk state as shown in black dash line. Blue line shows electrons moving at interface whose momentum relaxation time is τ_p^{int}. Black solid line shows electrons moving in bulk whose momentum relaxation is τ_p^{NM}. Fig 4(b) shows the schematic of spin relaxation process. At first, electrons at interface have certain momentum and corresponding spin direction, i.e. momentum $\boldsymbol{k} = +k_{\mathrm{x}}$ and spin $\boldsymbol{S} = -S_{\mathrm{y}}$. When electrons move at interface state, spin relaxation takes place due to spin-momentum locking in time scale τ_p^{int} as shown in blue dash line. For electrons moving from interface state to bulk state, the momentum direction is changed, $\boldsymbol{k} \neq +k_{\mathrm{x}}$, by electron scattering in the bulk as shown in the black solid line. Because the spin relaxation time in Cu or Ag is 3 order larger than τ_p^{NM} [6-19], most of the electron spin keeps its direction $\boldsymbol{S} = -S_{\mathrm{y}}$ in few scattering events. Now the electron momentum $\boldsymbol{k}$ and spin $\boldsymbol{S}$ of are different with the relation of spin-momentum locking at interface, $+k_{\mathrm{x}}$ and $-S_{\mathrm{y}}$. When these electrons move into the interface state, the spin relaxation is occurred by spin-momentum locking, which becomes an additional spin relaxation process with the spin relaxation time proportional to τ_p^{NM}. Therefore, mainly there is two spin relaxation process at metal/oxide interfaces. Spin relaxation time of electrons moving at the interface is τ_p^{int} while for electrons moving through interface and bulk, it is proportional to τ_p^{NM}.

Following this scenario, τ_{IEE} can be expressed by

$$ {\tau_{IEE}}^{-1} = (\tau_p^{int})^{-1} + C \cdot (\tau_p^{NM})^{-1} \tag{6.3} $$

where C is a constant determined by the contribution of bulk layer. The experiment result $\tau_{IEE} \propto \tau_p^{NM}$ suggests $C \cdot (\tau_p^{NM})^{-1}$ term dominant τ_{IEE}, which means most of the electrons take momentum relaxation in metal layer rather than at interface. This is reasonable because the resistance of 30 nm thickness metal layer is at least one order smaller than interface. Thus, most of the current is flow in the bulk layer rather than in interface. In the extremely case, when τ_p^{NM} or σ_{NM} is close to 0, which means the metal layer becomes semiconductor or insulator, because the current cannot flow in the bulk part, the constant C in eq. (6.3) becomes to 0 and the eq. (6.3) turns to be $\tau_{IEE} = \tau_p^{int}$, which is complete the same as 2DEG case.

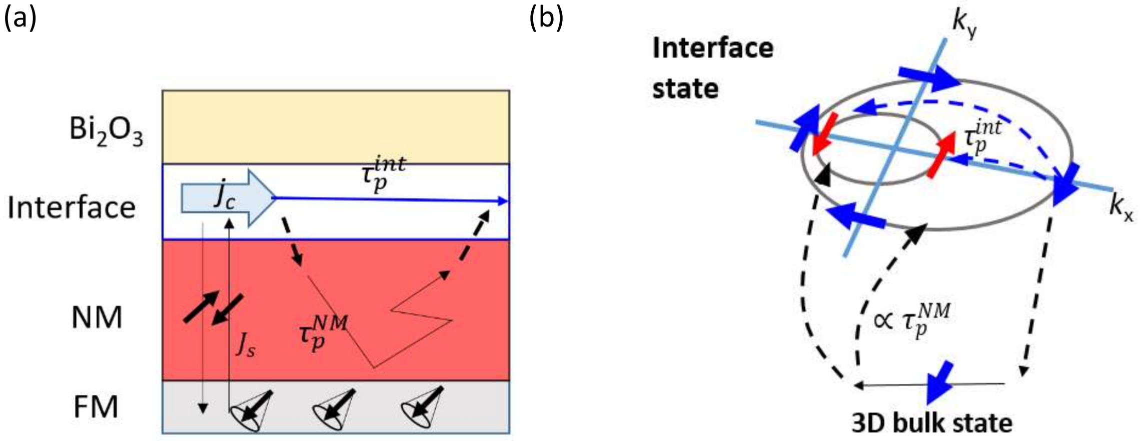

Figure 6-5.

(a) Schematic of momentum relaxation process. Charge current I_c generated by S-C conversion can flow through interface and bulk state as shown in black dash line. Blue line shows electrons moving at interface whose momentum relaxation time is τ_p^{int}. Black solid line shows electrons moving in bulk whose momentum relaxation is τ_p^{NM}.

(b) Schematic of spin relaxation process. When electrons move at interface state, spin relaxation is in time scale τ_p^{int} as shown in blue dash line. For electrons moving through bulk state and interface state spin relaxation occurred by spin-momentum locking is in time scale τ_p^{NM} as shown in black dash line

6.4 Summary of chapter 6

In this chapter, we measured temperature dependence of λ_{IEE} at NM(Cu,Ag) /Bi_2O_3 interfaces to observed the relation between λ_{IEE}, τ_{IEE}, and τ_p^{NM}. We found 40 (17)% enhancement of λ_{IEE} at 10K due to the increased τ_p^{NM} at low temperature and we found a relation $\lambda_{\mathrm{IEE}} \propto \sigma_{\mathrm{NM}} \propto \tau_p^{NM}$. From these results, we found that the spin relaxation time τ_{IEE} at interface is proportional to τ_p^{NM} of NM layer. This result can be explained by considering the additional momentum relaxation process in metal layer. This study provides a way to enhance λ_{IEE} at NM(Cu,Ag) /Bi_2O_3 interfaces by increasing τ_p^{NM} and also provides a further understanding of the relation between momentum relaxation time at metal layer and the spin relaxation time at metal/oxide Rashba interface.

Reference of chapter 6

[6-1] S. Karube, K. Kondou and Y. Otani, *Applied Physics Express* **9**, no. 3, p. 033001 (2016).

[6-2] L. Werake, B. Ruzicka and H. Zhao, *Physical Review Letters* **106**, no. 10, (2011).

[6-3] M. Hajlaoui, E. Papalazarou, J. Mauchain, L. Perfetti, A. Taleb-Ibrahimi, F. Navarin, M. Monteverde, P. Auban-Senzier, C. Pasquier, N. Moisan, D. Boschetto, M. Neupane, M. Hasan, T. Durakiewicz, Z. Jiang, Y. Xu, I. Miotkowski, Y. Chen, S. Jia, H. Ji, R. Cava and M. Marsi, *Nature Communications* **5**, no. 1 (2014).

[6-4] A. Caviglia, M. Gabay, S. Gariglio, N. Reyren, C. Cancellieri and J. Triscone, *Physical Review Letters* **104**, no. 12 (2010).

[6-5] J. Rojas-Sánchez, S. Oyarzún, Y. Fu, A. Marty, C. Vergnaud, S. Gambarelli, L. Vila, M. Jamet, Y. Ohtsubo, A. Taleb-Ibrahimi, P. Le Fèvre, F. Bertran, N. Reyren, J. George and A. Fert, *Physical Review Letters* **116**, no. 9 (2016).

[6-6] J. Sánchez, L. Vila, G. Desfonds, S. Gambarelli, J. Attané, J. De Teresa, C. Magén and A. Fert, *Nature Communications* **4**, no. 1 (2013).

[6-7] S. Ogawa, H. Nagano and H. Petek, *Physical Review Letters* **88**, no. 11 (2002).

[6-8] S. Zhang and A. Fert, *Physical Review B* **94**, no. 18 (2016).

[6-9] J. Kim, Y. Chen, S. Karube, S. Takahashi, K. Kondou, G. Tatara and Y. Otani, *Physical Review B*, **96**, no. 14 (2017).

[6-10] P. Drude, *Annalen der Physik* **306**, no. 3, pp. 566-613 (1900).

[6-11] F. Rosebury, *Handbook of electron tube and vacuum techniques*. New York: American Institute of Physics (1993).

[6-12] K. Ando, Y. Kajiwara, K. Sasage, K. Uchida and E. Saitoh, *IEEE Transactions on Magnetics* **46**, no. 6, pp. 1331-1333 (2010).

[6-13] R. Garg, I. Bahl and M. Bozzi, *Microstrip lines and slotlines* (1993).

[6-14] J. Krupka, J. Breeze, A. Centeno, N. Alford, T. Claussen and L. Jensen, *IEEE Transactions on Microwave Theory and Techniques* **54**, no. 11, pp. 3995-4001 (2006).

[6-15] Y. Zhao, Q. Song, S. Yang, T. Su, W. Yuan, S. Parkin, J. Shi and W. Han, *Scientific Reports* **6**, no. 1 (2016).

[6-16] P. Lubitz, J. Krebs, M. Miller and S. Cheng, *Journal of Applied Physics* **83**, 6819-6821 (1998).

[6-17] G. Counil, T. Devolder, J. Kim, P. Crozat, C. Chappert, S. Zoll and R. Fournel, *IEEE Trans. Magn.* **42**, 3323-3325 (2006).

[6-18] E. Sagasta, Y. Omori, M. Isasa, M. Gradhand, L. Hueso, Y. Niimi, Y. Otani and F. Casanova, *Physical Review B* **94**, no. 6 (2016).

[6-19] E. Villamor, M. Isasa, L. Hueso and F. Casanova, *Physical Review B* **87**, 094417 (2013).

Chapter 7

Conclusion

7.1 Conclusion of this thesis

This thesis presents a systematic study on the spin-charge interconversion phenomenon at metal/oxide interfaces. The thesis consists of three studies, the metal materials dependence, the oxide materials dependence and the temperature dependence of the spin conversion at metal/oxide interfaces. The first two studies focus on the relation between Rashba spin-splitting and different species of metal or oxide materials. The third study focus on the contribution of the metal layer of the spin and momentum relaxation time in spin-to-charge conversion process. These results demonstrate how the materials dependent electron distribution modulates Rashba spin-splitting and also explain the additional spin relaxation process due to the metal layer in S-C conversion process. Several guidelines for designing metal/oxide interfaces with efficient spin conversion are provided: (i) Larger Rashba spin-splitting can be obtained by choosing metal materials with close work function with oxide materials. (ii) The heavy elements are not necessary for the oxide layer. (iii) The larger spin-to-charge conversion efficiency can be enhanced by increasing conductivity of metal layer. These understandings of spin conversion phenomenon at metal/oxide interfaces could be useful to design and propose the new spintronics devices utilizing effectively the interface.

7.2 Future prospect

The findings of this thesis should excite further studying on the metal/oxide type Rashba interfaces. Here are some possible directions in the future.

7.2.1 Magnetization switching

Since the conversion efficiency of metal/oxide interface is comparable to heavy metals like Pt and Ta, it should be possible to perform the magnetization switching by spin torque generated from DEE at metal/oxide interfaces. Especially, the large spin conductivity at Cu(Ag)/ITO interface indicates that the energy consumption for spin current generation is smaller than using Pt or Ta.

7.2.2 Applying gate voltage on oxide layer

Similar with the gate voltage controlled Rashba parameter at oxide interface, at metal/oxide (insulator) interface, it is possible to apply gate voltage on the insulated oxide layer to tune the fermi energy of oxide material and also the interfacial electric field. Because interface electron distribution is strongly influenced by interfacial electric field as shown in chapter 4, it is expected that the Rashba parameter can be modulated by applying gate voltage.

7.2.3 Modulation of DEE relaxation time

In chapter 6, we show a way to modulate IEE relaxation time by changing temperature.
In addition, since the DEE efficiency is described by $q_{DEE} = \alpha_{\mathrm{R}}/(v_{\mathrm{F}}{}^2\hbar\tau_{\mathrm{DEE}})$, the modulation of DEE relaxation time τ_{DEE} can also increase q_{DEE}. As introduced in chapter 2, τ_{DEE} is the spin relaxation time of the spin current flowing from the Rashba interface to the adjacent NM layer and FM layer. Therefore, the FM layer may play an important role in τ_{DEE}. Investigating the FM materials dependence of C-S conversion should be a way to check the relation between τ_{DEE} and FM materials.

7.2.3 Using materials with long momentum relaxation time

Because the S-C conversion efficiency is proportional to the momentum relaxation time of conductive layer, it is possible to increase the efficiency by using conductive materials with long momentum relaxation time. However, for metal materials, the momentum relaxation time is always in the range of few ps. One possible candidate is using graphene as the conductive layer because it has been reported that the momentum relaxation time of graphene is in the order of fs. Graphene/Bi_2O_3 may be a possible candidate for efficient S-C conversion.

Publication

1) **H. Tsai**, S. Karube, K. Kondou, N. Yamaguchi, F. Ishii and Y. Otani, "Clear variation of spin splitting by changing electron distribution at non-magnetic metal/Bi_2O_3 interfaces", Scientific Reports, vol. 8, no. 1, 2018.

2) K. Kondou, **H. Tsai**, H. Isshiki, and Y. Otani "Efficient spin current generation and suppression of magnetic damping due to fast spin ejection from nonmagnetic metal/Indium-tin-oxide interface", APL Materials 6, 101105, 2018.3)

3) J. Puebla, F. Auvray, M. Xu, B. Rana, A. Albouy, **H. Tsai**, K. Kondou, G. Tatara and Y. Otani, "Direct optical observation of spin accumulation at nonmagnetic metal/oxide interface", Applied Physics Letters, vol. 111, no. 9, p. 092402, 2017.

4) J. Kim, **H. Tsai**, D. Go, K. Kondou, H. Lee, Y. Otani, "Non-trivial charge-to-spin conversion in ferromagnetic metal/Cu/Al_2O_3 trilayers" (in preparation)

Presentation

1) **H. Tsai**, K. Kondou & Y. Otani, "Strong spin-splitting modulation by various non-magnetic metal/Bi_2O_3 interfaces",62nd Annual Conference on Magnetism and Magnetic Materials(MMM2017), Pittsburgh, USA, November 2017. (Oral)

2) **H. Tsai**, K. Kondo & Y.Otani, "Temperature dependence of spin-to-charge conversion and Rashba spin splitting at non-magnetic metal/Bi_2O_3 interfaces", 2018 Autumn meeting of the Physical Society of Japan, Doshisha University, September 2018. (Oral)

3) **H. Tsai**, S. Karube, K. Kondou & Y. Otani, "Materials dependence of spin-to-charge current conversion at non-magnetic metal/oxide interfaces", 72nd Annual Meeting of the Physical Society of Japan 2017, Osaka University, March 2017. (Oral)

4) **H. Tsai**, S. Karube, K. Kondou & Y. Otani, "Spin to charge current interconversion at NM/Bi_2O_3 (NM = Cu, Ag, and Au) interfaces", INTERMAG 2017, Dublin, Ireland, April 2017. (Poster)

5) **H. Tsai**, S. Karube, K. Kondo & Y. Otani, "Materials dependence of spin-to-charge current conversion at non-magnetic metal/oxide interface", Spintech IX, Fukuoka, Japan, June 2017. (Poster)

6) **H. Tsai**, S. Karube, K. Kondou, F. Ishii, N. Yamaguchi & Y. Otani
"Clear variation of spin splitting by changing electron distribution at non-magnetic metal/Bi_2O_3 interfaces", The 11th Condensed-Matter-Science Cross-Area Workshop, University of Tokyo, November 2017. (Poster)

7) **H. Tsai**, S. Karube, K. Kondou & Y. Otani, "Materials dependence of spin-to-charge current conversion at non-magnetic metal/oxide interfaces", Status Meeting on Nano Spin Conversion 2017, Tokyo Institute of Technology, March 2017.

Acknowledgement

I would like to acknowledge all the people who help me complete this thesis and my PhD degree. Especially, I greatly appreciate my supervisor, Prof. Yoshichika Otani in Institute for Solid State Physics in the University of Tokyo, for giving me the chance to study in his group, giving the insightful and critical discussions and guiding me the way of doing research.

I would like to thank to Dr. Kouta Kondou in RIKEN, Institute of Physical and Chemical Research for helpful suggestion and discussion in every part of my research. Also I appreciate him for spent so much time helping me revise this thesis. It is impossible to complete this thesis without his help.

I appreciate to Prof. Fumiyuki Ishii and his student Mr. Naoya Yamaguchi in Kanazawa University for their calculation work and also the meaningful discussion in the paper published on Scientific reports. I also thank to Prof. Fumiyuki Ishii, Prof. Masamitsu Hayashi and Prof. Shinji Miwa for giving insightful comments and evaluating this thesis very carefully.

I am grateful to Dr. Junyeon Kim, Dr. Jorge Puebla, Dr. Bivas Rana, and Dr. Tomoyuki Yokouchi, researchers in RIKEN, Institute of Physical and Chemical Research, and Dr. Hironari Isshiki in Institute for Solid State Physics in the University of Tokyo. I have learned a lot from their research and their work attitudes encourage me to make more efforts in my PhD research.

I thank to Ms. Machie Kaitou and Mr. Kazuhiko Shihoyama in RIKEN for teaching me the technique for making samples and how to use equipment in clean room like photo-lithography and e-beam evaporation. I thank to Dr. Daisuke Hashizume in RIKEN for teaching me how to do XRD measurement and help me analysis XRD data.

I would like to thank to all group members and former members. I thank to Dr. Shutaro Karube and Dr. Norinobu Hasegawa for their help in the experiments. I thank to Dr. Florent Auvray, Mr. Mingran Xu, and Mr. Heeman Kim for encouraging me; it was a great pleasure to work with them. I thank to, Dr. Yasutomo Omori, Dr. Sei Takizawa, Dr. Hideki Narida, Mr. Kenta Matsumoto, and Mr. Yuki Mogi for stimulating my research. I also thank to our group secretary Ms. Michiko Ishinabe and Ms. Yoko Kaneda for all the paper works.

I would like to thank to Prof. Chien-Yuan Chen for encouraging and helping me join the doctoral course in Tokyo University. Finally, I would like to appreciate my family for their support and understanding during my PhD life.